Study on Electroactive Soft Actuators Based on Nanostructured Columnar Liquid-Crystalline Polymer Electrolytes

（ナノ構造カラムナー液晶性高分子電解質に基づく電気活性ソフトアクチュエータに関する研究）

Siyu Cao

Graduate School of Chemical Sciences and Engineering

Hokkaido University

2022

Contents

Contents

Contents

Abstract

Ionic electroactive polymer (**iEAP**) actuators that show reversible mechanical deformation by ion migration in response to an electric field have received enormous interest in the fields of artificial muscles, soft robotics, and haptics. Polymer electrolytes are one of the essential components for achieving high performance in **iEAP** actuators. Conventionally, amorphous ion gels and hydrated ionic polymers have been employed as polymer electrolytes. But, as the ions are transported by segmental motion of the polymer backbone or by diffusion in the entangled polymer chains, the ionic conductivities are in the range of 10^{-4}–10^{-7} S cm^{-1} at ambient temperature. A new efficient electrolyte design that can transport a large number of ions in a shorter distance is important to achieve fast and low-voltage-driven actuation. The author expected that the formation of continuous ionic channels into polymer electrolytes should lead to achieve fast response and large bending for **iEAP** actuators. Liquid-crystalline (**LC**) materials are one of the promising candidates for the preparation of nanostructured low dimensional ion-transporting channels. Up to now, a variety of liquid-crystalline electrolytes forming columnar, lamellar, and cubic structures have been developed and successfully applied in lithium-ion batteries and dye-sensitized solar cells. However, no **iEAP** actuators using ionic **LC** electrolytes have been developed. In this thesis, a new family of ion-conductive columnar **LC** polymer electrolytes forming 1D and 3D ion channels have been developed by two different self-assembly approaches and successfully applied in soft **iEAP** actuators for the first time.

In chapter 1, the general background of actuators including the working mechanism and recent development of **iEAP** actuators and ion-conductive **LC** materials are described. The objectives of this thesis are given.

In chapter 2, the author focused on the columnar **LC** derivatization of a zwitterionic molecule as a medium for proton transport. Imidazolium sulfobetaine is one of the zwitterions in which the charge-delocalized cation and anion are covalently bonded. The zwitterion tethering a fan-shaped polymerizable mesogen is expected to form 1D ionic channels but have no transportable ions. After addition of protic salts, the salts may be dissociated by the interactions with the zwitterionic moiety, which allows ions to move along the ionic pathways. Nanostructured proton and lithium-ion conductors were previously developed by co-assembly of low-molecular weight **LC** zwitterions and acidic molecules or lithium salts. However, the

Abstract

preparation of anhydrous 1D proton transporting polymer materials is still challenging. In this chapter, the author developed a new family of proton-conductive free-standing polymer films with randomly oriented 1D nanochannels by the columnar **LC** self-assembly of protic ionic liquids (**IL**) and a photopolymerizable fan-shaped zwitterionic molecule and the subsequent interlocking of the structures by *in situ* photopolymerization. Selecting the ionic liquids as nonvolatile electrolytes is the key to inducing nanostructured **LC** phases. The combination of the zwitterionic monomer and imidazolium bis(trifluoromethylsuflonyl)imide in the presence of water provided the room-temperature columnar liquid crystals, whereas the zwitterionic mixture with 1-butyl-3-methylimidazolium hydrogen sulfate formed the thermotropic columnar liquid crystals at room temperature without water. The polymer membranes obtained from the thermotropic columnar **LC** assemblies showed the anhydrous conductivities of 10^{-6}–10^{-9} S cm^{-1} at room temperature. In contrast, the hydrous polymer membranes obtained from the lyotropic columnar **LC** assemblies exhibited higher ionic conductivity in the order of 10^{-4}–10^{-3} S cm^{-1} at room temperature due to the accelerated ion diffusion by the incorporation of water molecules into the ionic channels. Furthermore, the hydrous columnar **LC** membranes showed 100–1000 times higher conductivity than the amorphous polymer films prepared by photo-preservation of the monomeric mixtures in the isotropic liquid state. The author has demonstrated that the nanostructured complexes of zwitterionic monomer and protic **ILs** can efficiently transport ions in the solid polymer matrices.

In chapter 3, the 1D nanostructured **LC** polymer film electrolytes were applied in **iEAP** actuators and their actuation performance was evaluated under various conditions. The nanostructured columnar **LC** polymers with the thickness of 64 μm were sandwiched between two conducting polymer electrodes, poly(3,4-ethylenedioxythiophene) doped with poly(styrenesulfonate) (**PEDOT:PSS**). The actuation strip showed a bending motion to the anode side. This is probably due to the swelling of the cathode layer by the accumulation of larger size of cations on the cathode. The anhydrous actuators showed a maximum bending strain of 0.65% under the application of an alternating current (AC) square voltage of ±2 V at a frequency of 0.01 Hz under ambient conditions and generated 1.2 mN under a direct current voltage of 2 V for 2 min. On the other hand, the maximum value of bending strain of the hydrous polymer electrolytes reached 0.84% under an AC bias of ±2 V at 0.1 Hz in 70% RH. The bending strain and generated blocking force can be enhanced by increasing the ion content in

the columnar **LC** polymers and employing ionic liquids with large volume differences between cations and anions. It is found that the use of thicker **LC** electrolytes can enhance the blocking force but reduce the bending strain. In this chapter, the novel soft actuators based on the columnar **LC** polymer film electrolytes organizing protic **ILs** into the 1D nanochannels were developed to induce large bending strain and blocking force at low driving voltage.

The uniform alignment of the 1D channels in the direction perpendicular to the columnar **LC** electrolyte membranes is expected to improve the ionic conductivity and actuator performance. However, it is quite difficult to control the orientation in the thick films exceeding 50 μm. In chapter 4, the author aimed to develop a new type of ion-conductive liquid crystal/polymer composite electrolyte forming 3D continuous nanochannels as an alignment free electrolyte showing high ionic conductivity. A rod-like zwitterionic molecule containing an imidazolium sulfobetaine moiety was designed and synthesized because the interaction of zwitterionic moiety and ionic liquids may change the molecular shape from rod-like to conical, which is favorable for the induction of inverted columns. The self-assembly of the zwitterionic mesogenic compound, 1-butyl-3-methylimdiazolium triflate as an ionic liquid, and poly(vinyl alcohol) (**PVA**) as a mechanically supported polymer matrix successfully induced a hexagonal columnar **LC** structure that formed 3D ionic transporting channels surrounding the mesogenic columns for the first time. These composite electrolytes maintained the columnar **LC** structures in humidified conditions over 60% RH and showed a mechanical stretchability. The actuator strips composed of the composite electrolyte and **PEDOT:PSS** exhibited a large displacement of 15 mm under the application of an AC voltage of ±1 V at 0.1 Hz in 70% RH. The bending strain reached 0.32%, which is larger than those of reported amorphous **iEAP** actuators containing larger amount of ionic liquids. In addition, the bending speed of **LC**/polymer composite actuator was two times faster than that of the amorphous actuator consisting of **PVA** and the same amount of ionic liquid under an AC bias of ±0.5 V. In this chapter, the author demonstrated that the inverted columnar **LC** /polymer composite films with 3D interconnected ionic channels can be a new soft actuator that exhibits fast and large deformation at low driving voltage despite the low ion content.

In chapter 5, overall summary of this thesis and future perspectives are presented. This thesis has reported columnar **LC** polymer films confining ionic liquids into 1D and 3D channels and the first application to electroactive actuators that exhibited low-voltage-driven bendability

Abstract

and force generation in the air and humidified conditions. This work has unveiled a direct correlation between the nanochannels and the actuation performances. The concept of **LC** nanosegregation may lead to new designs for **iEAP** actuators to achieve the conflicting functions of high-power generation and fast motion.

Chapter 1 Introduction

1.1 Electroactive soft actuators

1.1.1 General background for soft actuators

In recent years, artificial muscles,[1-2] also known as muscle-like actuators, have attracted a growing interest in the field of soft robotics,[3-5] virtual reality,[6-9] bionics,[10-11] and so on. These materials or devices can generate reversible contraction, expansion, or rotation to external stimulus such as electric or magnetic field, thermal or chemical stimulation, fluid pressure, and light. For these energy-to-motion conversion devices, the maximum transduction of input energy to motion and minimum of energy consumption are sustained pursuit for developing modern actuators through advanced materials, novel mechanical design, and superior assembly.

Traditional actuators have low energy density and power-to-weight ratio due to the stiffness of manufacturing materials, which caused the application in the field of low energy consumption, lightweight, and small-scale robotics was limited. Moreover, the rigidity of actuators can also hinder the continuous deformation and natural motion pattern that decreasing the possibility for employing in artificial skins, wearable electronics, and soft haptics. Next generation of actuators requires a bold departure from traditional actuators and more similar to the materials found in living organisms. To mimic the inherent characteristics of mankind muscles and skins, numerous soft and active materials for actuators with the properties of flexibility, stretchability, self-healing were developed and researched.[12-15] Among these, electroactive polymers (**EAPs**) actuators are one of most promising candidates for artificial muscles due to their ability of emulating natural muscles accurately. These types of actuators will be detailed introduce in next section.

Soft actuators were divided into three major groups depends on their actuation stimuli: pneumatic, thermal, and electroactive actuation. Pneumatic actuators can generate contractile and extensional deformation operating by pressurized air or fluid (in this case, it was called as hydraulic actuators). The best-known pneumatic actuators are McKibben Artificial Muscles, which were first developed by J. L. McKibben in the 1950s.[16] Pneumatic actuators have high power-to-weight ratios, maintain compliance at low temperatures, lightweight, and are

potentially low cost.[17-18] However, the working pneumatic actuators requires air compressor, and the precise direction of movement is difficult to be controlled. Therefore, other alternative types of soft actuators are flourishing.

Thermal triggered actuators can be deformed and returned to original shape activating by light, thermal radiation, or Joule heating. The most developed thermal response materials for actuators were shape-memory materials including shape-memory alloys,[19] polymers,[20] and ceramics.[21] The deformation of crystalline structure by heat stimuli enables the macroscopic shape change. For example, nylon owning semicrystalline structure was well-known as thermoresponsive polymer. During heating, the crystalline regions show expansion in volume while the amorphous chains shrink in length. The amorphous phases are energetically less stable than the crystalline phases. Therefore, the nylon fibers expand in diameter while shrink in length.[22] Other thermoresponsive actuators working with different mechanism based on liquid-crystalline elastomers, hydromorphic materials were reported in reported literatures.[22-25]

1.1.2 Electroactive polymer actuators

EAPs are a type of polymers that can change shape and size when applying electrical energy. They are widely used in actuators due to their high flexibility, lightweight, low noise.[26] The actuation behavior of **EAP**s-based actuators can be easily adjusted by controlling electronic signals such as magnitude, phase, and frequency. Consequently, they can be driven by simple operation and exhibit good compatibility with electronics and batteries after integrating with electrical drivers and power sources. Moreover, because of simple fabrication and easy miniaturization, **EAP**s-based actuators can be applied to the microscale objects such as micro robotics,[27-28] microfluidic systems,[29] biomedical application,[30] *etc*.

The **EAP**s actuators were broadly classified into two types: 1) non-ionic **EAP**s actuators driven by electric field or Coulomb force; 2) ionic **EAPs** (**iEAP**s) actuators driven by ion diffusion. The former classification usually includes dielectric-elastomer actuators (**DEA**s), ferroelectric-polymer actuators (**FPA**s), and liquid-crystal elastomers (**LCE**s) actuators. The latter classification includes ionic conjugated polymers (**CP**s)-, ionic polymer-metal composites (**IPMC**s)-, and bucky gels-based actuators, which will be highlighted later in this section.

Chapter 1

Field-Activated Electroactive Polymer Actuators

DEAs are driven by Coulomb force, which attracted two electrodes in different potential on both sides of a compressible membrane.[31] The typical materials for **DEA**s are acrylic elastomers,[32] silicones,[33] polyurethanes,[34] which can exhibit extremely large strains (more than 1000%),[35] high energy density, and fast response. The performance of **DEA**s is highly depended on elastomer stiffness, dielectric constant, viscoelastic properties, and breakdown voltage. Normally, DEAs are operating on high excitation voltage (the order of kilovolts), which is considered to increase the risk of current breakdown and currents leakage and be unsafe wearable and biomedical devices.

FPAs are crystalline polymers that can generating lattice strain and dimensional change by the transition from polar to nonpolar states under electric fields. The most popular materials for **FPA**s are poly(vinylidene fluoride) (**PVdF**), famous for their stable chemical and thermal properties. Zhang *et.al* reported a ferroelectric polymer poly(vinylidene fluoride trifluroethylene) (**PVDF-TrFE-CFE**) copolymer exhibited a strain of 4% under an electric field of 150 MV/m.[36] Later, the strain of **PVDF-TrFE-CFE**-based actuator was improved to 7% by irradiated with high-energy electrons or protons.[37]

LCEs are lightly crosslinked liquid-crystalline polymer networks (**LCN**s) in which the mesogenic units are attached to main-chain or sidechain of polymers. The first **LCE**s was polysiloxane compositions, reported by Finkelmann in the 1980s.[38] When applied external stimuli such as electric field, thermal, and humidity, the mesogenic units will be aligned and the polymer chain will be reorganization, resulting in the shape deformation of materials. The reported electroactive **LCE**s includes ferroelectric **LCE** films that exhibit a strain of 4% with an electric field of 150 MV/m,[39] isotropic genesis polydomain nematic **LCE** which the strain can reach 25% under an electric field of 25 MV/m.[40]

Although non-ionic **EAP**s can generate large strain, rapid response speed, high mechanical energy density, how to significantly reduce operating electric field is still a big challenge. Here are some studies on soft actuators that can work at lower applied voltage, which are more favorable for artificial skins and wearable devices.

Ionic-Activated Electroactive Polymer Actuators

In **iEAP**s-based actuators, the actuation is driven by the motion of ions, normally under

several volts. In a few years, various **iEAP**s materials for actuation applications were explored and can be divided into **IPMC**s, bucky gels, and **CP**s based on the type of electrode materials.

***IPMC**-based Actuators*: **IPMC**-based actuators are composed of an ion-conductive polymer electrolytes between two flexible metal electrodes, typically coating with Pt nanoparticles or Au. The bending actuation was mainly driven by the migration of mobile ions to the opposite charged electrode under an applied voltage. The first bending phenomenon for **IPMC** was Nafion™ plated with Pt, reported by Oguro *et al.* in 1992.[41] The Nafion films can form hydrophilic channels inside the immobilized anionic polymer networks when exposure to water. When a voltage is applied to Nafion-based actuators, hydrated cations can move freely to the cathode through the channels, resulting in asymmetric distribution of ions in the thickness of polymer and expansion and contraction of cathode and anode, respectively. The molecular structure of Nafion and the schematic illustration of **IPMC**-based actuators are shown in Figure 1-1. Typical **IPMC**-based actuators suffer from obvious drawbacks such as low durability working in dry air, weak blocking force, and back relaxation. The new strategies for overcoming these problems are using the nonvolatile liquids such as ionic liquids (**IL**s) instead of water, optimizing electrode materials or adhesion between electrolyte and electrodes, modifying molecular structure of electrolytes for better ion distribution and faster ion migration.

Zhang *et al.* reported a series of **IPMC**-based actuators composed of Au electrodes and Nafion™ electrolytes containing various types of imidazolium-**IL**s and examined the influence of **IL**s on performance.[42] The actuators with smallest mobile ions and weakest binding energy exhibited shortest charging time and strain response time, and highest capacitance. Moreover, although there is a fourfold difference in total accumulated charge among **IL**s in this study, the difference in equilibrium strain is not very large (maximum value of 2% for **[BMIM]$^+$[BF$_4$]$^-$** *vs.* minimum value of 1.5% for **[EMIM]$^+$[CF$_3$SO$_3$]$^-$**). The effects of thickness of electrolytes on displacement and output force were explored by comparing **IPMC** actuators composed of Pt electrodes and commercial thin Nafion film/lab-cast thick Nafion films and founded that the thick electrolytes exhibited smaller displacement but larger block force.[43] Besides, the effects of thickness of Au electrodes on electromechanical performance for Nafion-based **IPMC** actuators were also investigated. The blocking force was increased as increased thickness of electrodes from 10 to 45 nm and then decreased with thickness from 45 to 80 nm.[44] In normal Nafion-based **IPMC** actuators, the initial response is generated after applying a DC voltage and

then followed by a motion in opposite direction, which is called back-relaxion.[45] It can be eliminated by modifying electromechanical coupling between **IL**s and polymer matrix. There are some researches about **PVdF**-based **IPMC** actuators that shown no back-relaxation, such as **PVdF** copolymers, **PVdF** blends with other polymers, and grafted cationic or anionic **PVdF** films.[46-48]

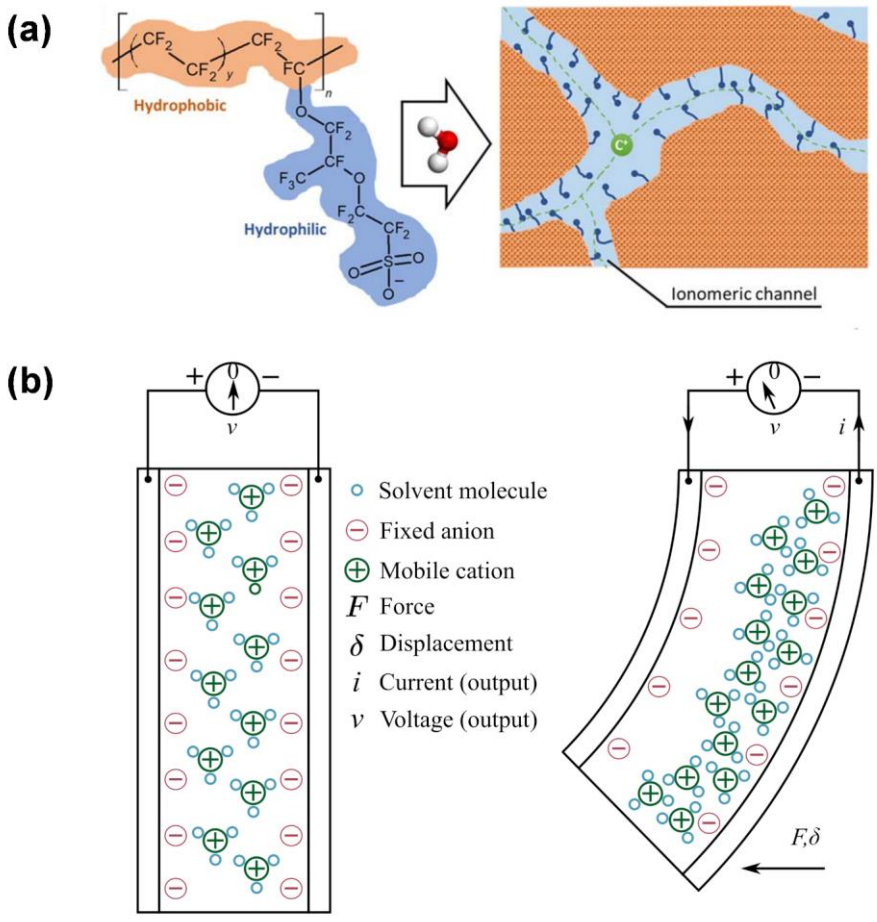

Figure 1-1. (**a**) The molecular structure and illustration of Nafion 117™, where C^+ is any cation;[49] (**b**) The bending mechanism of **IPMC**-based actuators.[50]

Bucky Gels-based Actuators: Bucky gel actuators are tri-layer structured **iEAP** actuators that integrated by ionic gel electrolyte sandwiching with two nanocarbon dispersed ionic liquid gel electrodes. The first example of nanocarbon materials used as electrodes of actuators was single-walled carbon nanotubes (**SWCNT**s) electrodes that laminated on the Scotch tape-based interlayer, reported by Baughman in 1999.[51] Since then, successive studies of high-performance buck-gel actuators were explored by Aida *et al*.[52-54] The working mechanism of typical bucky

gel actuators is the combination of the volume change in both cathodes and anodes caused by steric repulsion effect of injected ions and the accumulation of ions on the interface of electrolytes and electrodes. Therefore, the capacity and conductivity of electrodes as well as the ion mobility in the electrolytes plays a key role to achieve large bending and fast response. To improve the charge carriers and specific surface area of electrodes, nanocarbon materials with porous structure were used as electrodes, such as carbide-derived carbon, multi-walled carbon nanotubes (**MWCNT**s), activated carbon nanofibers.[55-57] In addition, the capacity and conductivity can be enhanced by addition of nanoparticles such as silica, carbon black, and polyaniline into **CNT** electrodes.[58]

More recently, inducing hierarchical architecture into electrodes that paving interchannels for charge carriers has drawn a lot of attention, which can achieve orders-of-magnitude improvements in displacement and fast actuation response. For example, Xie *et al.* reported a type of as-grown **SWCNT** electrode films with hierarchical structures employing on a chitosan electrolyte layer which shown a superfast response (19 ms), large stress rate (1080 MPa s^{-1}), and ultrahigh mechanical output power density (244 W kg^{-1}).[59] Furthermore, the continuous ion channels can be created by vertically aligned **CNT**s or NiO nanowall arrays on the surface of **CNT**s[60-61]. The nanostructured electrodes provided larger specific area and smaller electrical resistance enabling quick response speed (>8 % s^{-1}) and good durability (500 000 cycles) in the air. Chen et al. reported a bucky gel actuator based on black phosphorous/**CNT**s (**BP-CNT**) electrodes with ordered lamellar structure which can realize outstanding electrochemical capacitance (321.4 F cm^{-1}), large peak-to-peak strain (1.67%), fast strain and stress rate (11.57 % s^{-1} and 28.48 MPa s^{-1}), a wide working frequency range (0.1–20 Hz), and excellent cycling stability up to 500 000 cycles (Figure 1-2).[62]

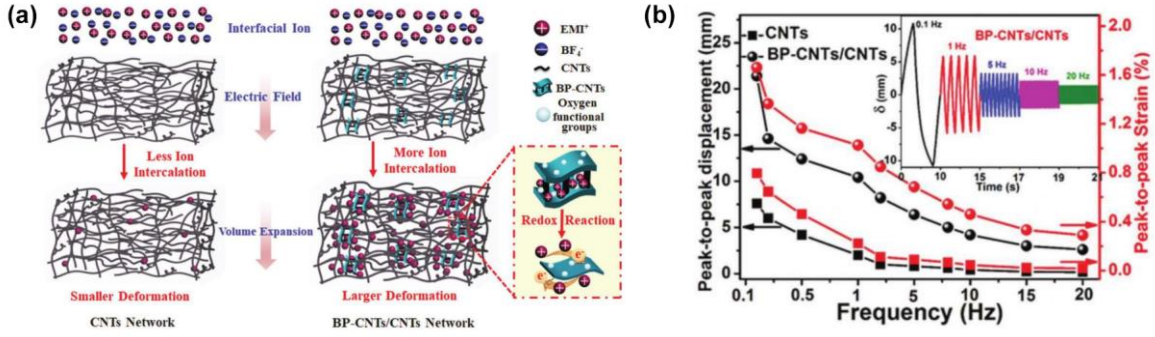

Figure 1-2. (a) Schematics of structure and ion transportation of **BP-CNT** electrode; (b) Peak-to-peak displacement and strain under an applied voltage of ±2.5 V with various frequencies.[62]

Chapter 1

***CP**s-based Actuators*: **CP**s are organic compositions that can conduct electrons by conjugated orbitals and can be high electrically conductive if doped with ions. **CP**s can be positively charged (p-doped) or negatively charged (n-doped) depends on if electrons were detached or inserted to polymer backbone. The electric response of **CP**s was induced by counterion diffusion during oxidation/reduction reaction when an electric field was applied. In anion driven **CP**s (p-doped), the dissociated anions from electrolytes will flow into polymer matrix to maintain the charge neutrality of **CP**s, which result in the expansion during the oxidation process of electrodes. In reduced state, the ions migrated away from polymer chains which caused the contraction of polymers. The cation driven **CP**s (n-doped) will demonstrate the opposite behavior that contract/expand during the oxidation/reduction process. The oxidation/reduction process of anion driven **CP**s and cation driven **CP**s were shown in equation 1-1 and 1-2, respectively.

p-doped	Reduction:	$P^+(D^-) + e^- + C^+ \rightarrow P^0 + D^- + C^+$	(contract)	**1-1**
	Oxidization:	$P^+(D^-) - e^- + A^- \rightarrow P^+ (D^- + A^-)$	(expand)	
n-doped	Reduction:	$P^-(D^+) + e^- + C^+ \rightarrow P^- (D^+ + C^+)$	(expand)	**1-2**
	Oxidization:	$P^-(D^+) - e^- + A^- \rightarrow P^0 + D^+ + A^-$	(contract)	

where P^+/P^- is doped polymer, D^-/D^+ is dopant, and C^+/A^- is injected cations/anions from dissociated **IL**s. Like other **iEAP** actuators, ion diffusion to interlayer between electrolytes and electrodes can also cause the deformation of actuators. Therefore, the actuation response of **CP**s is a synergistic effect of electrochemical reaction of electrodes and ion accumulation of electrolytes.

The concept of **CP**s-based actuators was proposed by Baughman in 1991.[63] Until now, most commonly used **CP**s are polypyrrole (**PPy**),[64-65] polyaniline (**PANI**),[66] and poly(3,4-ethylenedioxythiophene):polystyrenesulfonate (**PEDOT:PSS**) (Figure 1-3).[67-69] Among these, commercialized **PEDOT:PSS** dispersed aqueous solution is widely used because it can be easily processed via coating, inkjet, and 3D printing.[70-71] **CP**s-based actuators normally can work under low voltage (1–2 V), with bending strain from 1 to 40%.[72-73] Oh *et al.* reported an **iEAP** actuators composed by a freeze-dried bacterial cellulose membrane sandwiched between

two **PEDOT:PSS** electrodes.[74] These hybrid actuators shown electrical response at low applied voltage (1 V) when two kind of **IL**s were employed into the electrolyte by dipping. The working mechanism of electrochemical reaction on electrodes and ion migration in electrolyte was illustrated in Figure 1-4. The electrons flowing into cathode triggered reduction reaction that caused **PEDOT**$^{+}$ becoming to **PEDOT**^{0} and at the same time dissociated cations of **IL**s were bonding with **PSS**$^{-}$, which resulting in swelling of cathode. On the other hand, the **PSS**$^{-}$ in the anode was oxidized to **PSS**^{0} by the expulsion of electrons. The asymmetric volume change of cathode and anode caused the bending towards anode side.

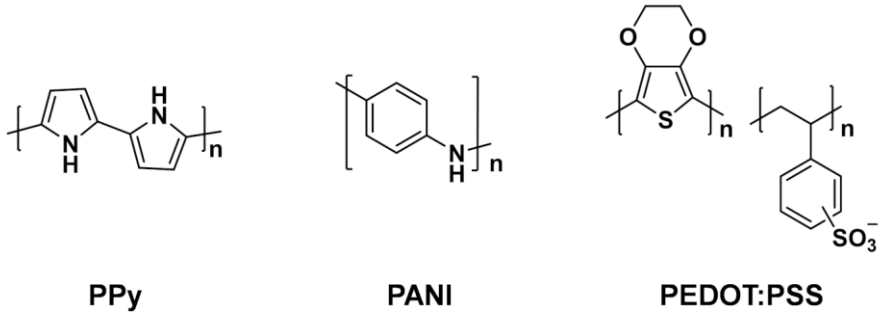

Figure 1-3. Chemical structures of polypyrrole (**PPy**), polyaniline (**PANI**), and poly(3,4-ethylenedioxythiophene):polystyrenesulfonate (**PEDOT:PSS**).

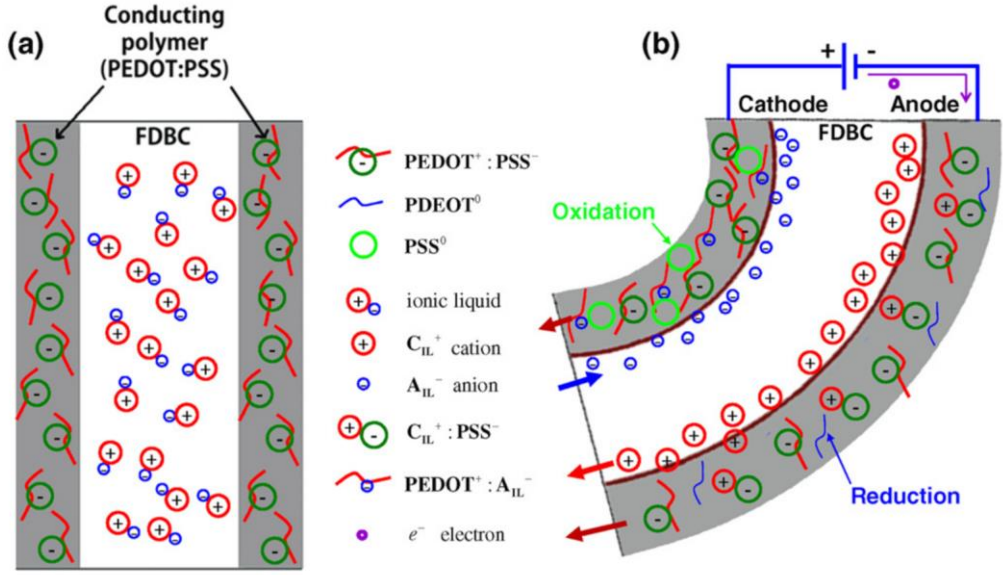

Figure 1-4. Illustration of actuation mechanism of **PEDOT:PSS**-based actuator with freeze-dried bacterial cellulose electrolyte.[74]

1.1.3 Ionic electroactive polymer actuators based on nanostructured electrolytes

Looking back at the above-mentioned **iEAP**-based actuators, besides the effect of electrode materials on actuation performance, ion migration in electrolytes is another crucial factor. The electrolytes with high ionic conductivity can achieve shorter response time and the difference in volume of cations and anions will correspond to bending displacement. The use of nanostructured block polymers with ion transporting channels to fabricate **iEAP** actuators with fast and large deformation are advanced technologies. Long *et al.* employed tri- and penta-block copolymers containing imidazolium into **IPMC** actuators.[75-76] The microphase-separated morphologies facilitated ion transporting in the polymers and the curvatures surpassed the Nafion™-based actuators. Further progress for mentioned pentablock copolymers based **IPMC** actuators was reported by *Koo et al*.[77] In addition to ion channels constructed by pentablock copolymers, the impregnation of sulfonated montmorillonite which building bridges between ionic domains can achieve larger ionic conductivities and bending displacement comparing with Nafion/**IL** based actuators.

Park *et al*. introduced zwitterions into block copolymers forming well-defined ionic domains which called single-ion conductor.[78] The actuator based on single-ion polymers can move several millimeters under 1 V with an initial response time as short as 20 ms (Figure 1-5a). Another enlightening method for constructing nanostructured **iEAP** actuator is to employ blend of **PVdF** and polyvinyl pyrrolidone as electrolyte. The resultant **PVdF** film produced 3D interconnected hierarchical channels and a high porosity of 15.8% which can adsorb water or **IL**s for driving actuation.[47] Both water- or **IL-** driven actuators exhibited much higher displacement and force compared to conventional **PVdF**/**IL**-based actuators (Figure 1-5b)

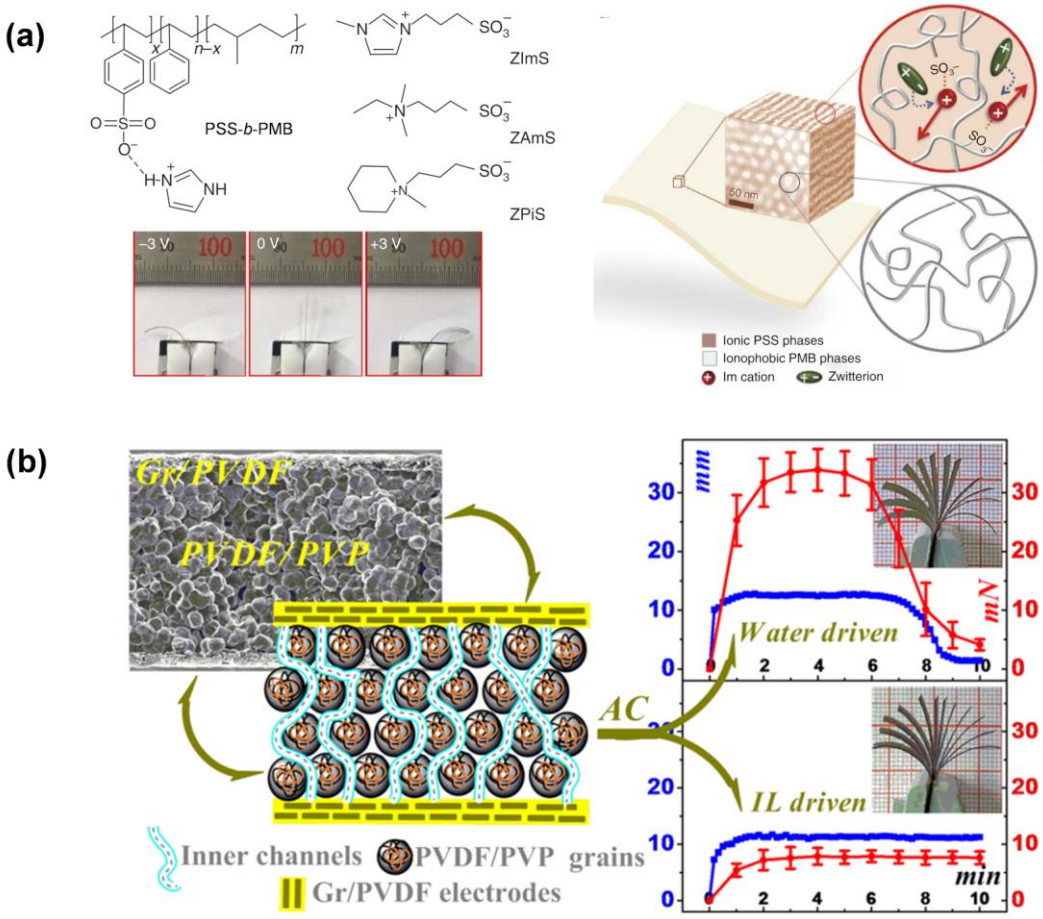

Figure 1-5. (a) Molecular structures and illustration of imidazole-doped copolymer of sulfonated polystyrene (**PSS**) and polymethylbutylene (**PMB**) and zwitterions. Photographs are actuators based on ZIMs;[78] (b) Left: SEM image and illustration of cross-section of **PVdF**-based actuator. Right: Time-dependent displacement and blocking force of water- and **IL**- driven **PVdF**-based actuators under an AC applied voltage of 10 V and a frequency of 0.1 Hz.[47]

Obviously, the self-assembled polymers with ionic channels are excellent materials for quick and large deformation actuators. The well-organized pathways can facilitate ion migration with lower resistance. However, the precise synthetic procedures are necessary to prepare block polymers. In this thesis, we introduced a new strategy for constructing nanostructured ionic nanochannels by introducing liquid-crystalline assemblies.

1.2 Liquid-crystalline materials

1.2.1 General background for liquid-crystalline matter

The liquid-crystalline (**LC**) phase in matter is defined as an intermediate phase between crystalline phase and isotropic liquid phase, so it also been called as mesophase.[79-80] The mesogenic moieties that introduced into molecules can induce **LC** behavior. Normally, the mesogenic group contains aromatic rings to provide "rigid" parts for **LC** molecules. When substance entered **LC** state, the order structure, which is the typical behavior of crystalline state, was partially reduced. It allows the molecules possess more mobility, which result in **LC** materials behaving as an ordered fluid (Figure 1-6). The individual molecule in **LC** phase is not fixed in certain position but it directs in one direction in each molecular monodomain, which called "long-range order".[81] The orientation of **LC** is aligning molecules to parallel with each other, which turning **LC** materials from polydomain to monodomain state. The orientation of **LC** molecules can minimize the excluded volume and maximize molecular interaction.[82-83]

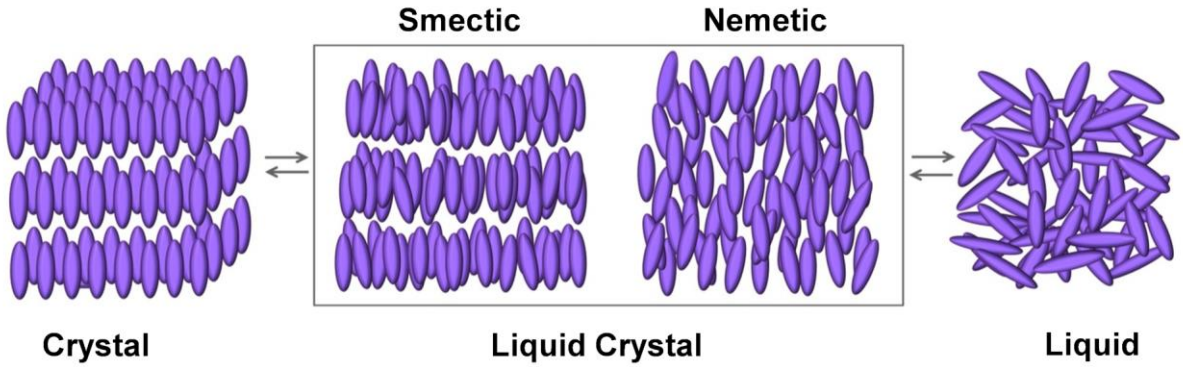

Figure1-6. Illustration of molecular arrangement of crystal, **LC**, and isotropic liquid.

Depends on the molecular arrangement, the nanostructure of **LC** can be roughly divided into three types: columnar (one dimensional), lamellar (two dimensional), and cubic (three dimensional) (Figure 1-7).[84] These structures are formed by phase segregation of immiscible part of molecules. The congregation of ionophilic parts construct the continuous channels for transportation.

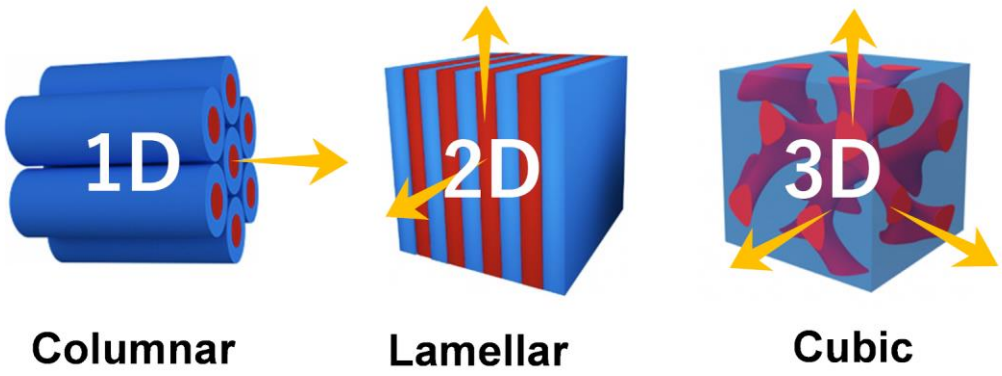

Figure 1-7. Illustration of **LC** phase.

1.2.2 Self-assembly of ionic liquid crystals

The self-assembly of **LC** molecules provided continuous and ordered ionic pathways which are widely applied in the field of batteries, semiconductors, electrochemical devices and so on.[85-86] In order to greater functionalize **LC** materials, some molecular designs focus on molecular interaction, nanosegregation, and molecular shape were developed.[87] There are two types of **LC** materials for ion conduction, one is the complexes of non-ionic **LC** molecules with ionic salts; the other one **LC** molecules containing cationic, anionic, zwitterionic moieties, called ionic liquid crystals. Among these, zwitterionic molecules with covalently bonded cationic and anionic moieties exhibited electrical neutrality can perform as ion conductive matrix for transporting target ions. The first application of zwitterionic molecules for ion conduction is reported by Ohno *et al.* in 2001.[88] They polymerized zwitterionic molten salts containing imidaozulium cations and sulfonimide anions and the ion conductivity can reach 10^{-4} S cm^{-1} by addition of lithium bis(trifluoromethanesulfonyl)imide (**LiTFSI**).

Recent years, ionic liquids are rapidly developed in electrochemical application because of its properties such as high ionic conductivity, low vapor pressure.[89] The introduction of **IL**s into zwitterionic **LC** molecules can provide mobile and selective ions for **LC** materials, which are promising for high efficiency conduction. Ohno *et al.* designed a type of phosphonium zwitterions with sulfonate anionic moieties and lyotropic columnar **LC** phase was induced by mixing with bis(trifluoromethanesulfonyl) imide (**HTFSI**) and a small amount of water (Figure 1-8a).[90] The 1D ionic conductivities can achieve 10^{-2} S cm^{-1} after alignment into monodomain state.

The columnar **LC** provided 1D conductive channels for ion, however the insulation between inner channels of columns caused by ionophobic parts obstructed the continuous ion migration. The connection of ionic channels between each molecular domains should be taken into consideration to promote conduction. Ichikawa and coworkers reported a new type of cubic **LC** materials by self-assembly of pyridinium zwitterions and **HTFSI** (Figure 1-8b).[91] The mixtures shown not only cubic phase, but also columnar and smectic phase by tuning the length of alkyl chain. By addition of water, there was a 3D hydrophilic gyroid surface was constructed and formed continuous hydrogen-bond networks. The cubic lyotropic **LC** materials exhibited the highest ionic conductivities of 8.4×10^{-4} S cm^{-1} at 82 °C. Further increasing temperature will lead to a decline of conductivities following a phase transition from bicontinuous cubic phase to isotropic liquid phase. The nanostructure and ion conduction were influenced by water content in lyotropic **LC** materials and working temperature.

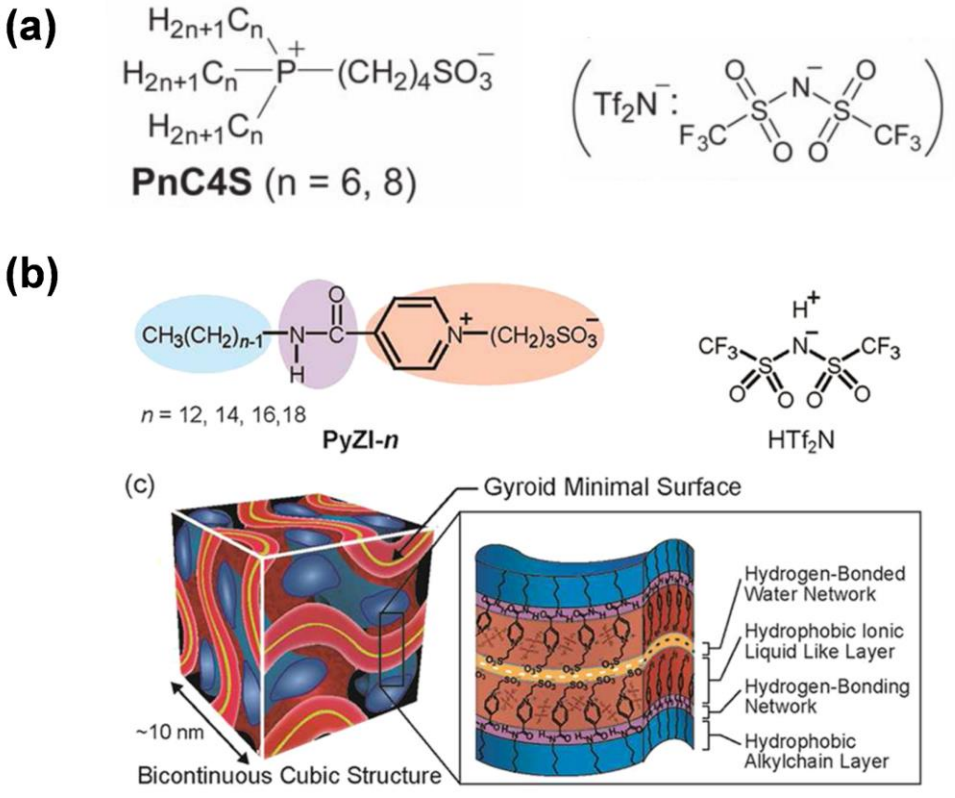

Figure 1-8. (a) Chemical structure of phosphonium zwitterions and **HTFSI**;[90] (b) Chemical structure of pyridinium zwitterions and illustration of **LC** assembly of pyridinium zwitterions and **HTFSI**.[91]

The self-organization of zwitterionic molecules and ionic liquids is a powerful approach for constructing low dimensional **LC** materials to achieve ordered conduction. However, the maintenance of **LC** nanostructure in these materials in a variable temperature and humidity of environment is a problem for practical application. The fixation of ordered molecules should be one of useful methods to preserve **LC** structure in solid electrolytes for wider operating environment.

1.2.3 Ion-conductive polymer membranes with liquid-crystalline nanostructures

In situ photopolymerization can irradiate sample at the **LC** phase, which can fix the ordered molecular architecture and obtain free-standing polymer films. The polymers with **LC** nanostructure can work in high temperature with no phase change. And the macroscopic orientation of **LC** molecules in the polymer film can also be achieved by *in situ* photopolymerization of aligned **LC** monomer. There are some inspiring researches about ion conductive polymer films with fixed low dimensional **LC** nanostructure.

Yoshio *et al.* has designed a fan-shaped imidazolium salt with polymerizable acrylate chains in the end of mesogens.[92] The salts shown thermotropic columnar **LC** behavior and formed 1D transporting nanochannels at room temperature in which the ionic part was in the inner of columns. To investigate the anisotropic conduction in materials, the columnar **LC** molecules were aligned in two directions: the column was parallel and perpendicular to the surface of film. The following UV photopolymerization allowed two directions of aligned **LC** molecules was fixed and transparent free-standing films with macroscopic oriented nanochannels were obtained. The ionic conductivities were measured in two directions for both two types of aligned polymers: electric field is parallel and perpendicular to the column axis. The ionic conduction exhibited strong anisotropy, which the conductivities along column axis were higher than those perpendicular to column axis for two films. The anisotropy of films that columns are vertical to the surface was about 10 times higher than the films that columns were parallel to the surface at 150 °C. In addition, the conductivities of macroscopic oriented films were higher than that of film with amorphous structure. These orientation of ionic parts by macroscopic alignment paved effective transporting channels for ions and the fixation of **LC** phase by photopolymerization provided 1D nanostructured solid electrolytes.

The lamellar **LC** structure was considered to have higher ordered molecular arrangement

comparing to columnar structure. The ions can be transported along two directions in the layer of each molecular domain. The orientation of lamellar **LC** mesogens to make ionic conductive layers vertical to the surface of film is easier to achieve comparing to columnar **LC** materials. The co-assembly of imidazolium zwitterion and 4-dodecyl benzenesulfonic acid can induce lyotropic smectic **LC** phase which achieved 2D proton conduction.[93] The ionic conductivities of monomeric **LC** materials can reach 10^{-1} S cm^{-1}, however the water evaporation limited the application in high temperature condition. The photopolymerization of lyotropic smectic **LC** assembly gave a proton conductive electrolyte film with lamellar nanostructure which allowed operating temperature can be enhanced over 100 °C. The highly ordered proton transporting channels in the polymer matrix resulted in higher conductivities in order of 10^{-3} S cm^{-1} and lower activation energy of 11.82 kJ/mol comparing to Nafion 117. The design of 2D conductive **LC** films provided a new strategy proton exchange membrane fuel cell.

The high effective proton conductive electrolyte can be further improved *via* constructing cubic **LC** structure in the films. The 3D continuous transporting channels can be formed in cubic **LC** phase without any alignment. The Grotthuss mechanism for proton conduction can occur along the continuous hydrogen bond networks in cubic **LC** polymers. The co-assembly of amphiphile having two zwitterionic head-groups and **HTFSI** was formed cubic **LC** phase with bicontinuous gyroid minimal surface.[94] A polymer film with 3D proton transporting channels was given by *in situ* photopolymerization. The polymer films can adsorb water when placed in a humid atmosphere due to strong hydration ability of the zwitterionic parts. The cubic **LC** nanostructure was maintained even the polymer was fully adsorbed water. The water molecules covering on the gyroid surface formed a continuous water nanosheet in which the proton hopping through hydrogen bonding network can achieve high speed transporting with a conductivity of 10^{-3} S cm^{-1} at room temperature.

The *in situ* photopolymerization of **LC** assemblies allowed the materials to maintain ordered arrangement ignoring the change of temperature and humidity in environment. The nanostructured solid polymer electrolyte that providing low dimensional effective conduction can be applied in a variety of electronic devices and adapted to more complex operating condition.

1.3 Objectives and thesis outline

Considering about the working mechanism of **iEAP** actuators, the capability of ion migration in the electrolyte layer plays a crucial role for achieving fast and large actuation. The ordered nanochannels in electrolyte can pave the pathway for high effective ion migration. The objective of this dissertation is introducing nanostructured **LC** assemblies into **iEAP** actuators to expand the application field of **LC** materials and overcome drawbacks of present actuators.

The author expected that 1D columnar **LC** phase can be induced at room temperature by combination of zwitterionic molecules and ionic liquids. And the well-organized **LC** nanostructure can be preserved in solid electrolyte film by *in situ* photopolymerization. The actuators based on 1D columnar **LC** polymer electrolyte can show fast and large bending motion in both dry and humid environment. The actuation performance such as bending strain, response time, and generated force can be investigated at various condition and the influenced factors on actuation can be explored. To further improve ion transporting in the actuators, the **iEAP** actuators with 3D continuous ionic channels in electrolytes need to be designed. There are two arrangements for **LC** materials with 3D conductive network: cubic phase and inverted columnar phase, in which the ionophilic parts were surrounding the columns and connected with each other. Normally, it is difficult to induce cubic phase at room temperature. Therefore, inducing 3D inverted columnar phase by co-assembly of zwitterionic molecule and ionic liquids will be challenged in this study. The **LC** materials with 3D conductive channels can be applied in actuators and show fast response speed and large deformation.

This dissertation was divided into four parts and described as follow:

In chapter 2, ion-conductive polymer membranes with 1D columnar nanochannels were developed. A new fan-shaped zwitterionic molecule containing imidazolium cationic, sulfonate anionic, and polymerizable acrylate groups was designed and synthesized. Two types of protonic ionic liquids were mixed with zwitterionic compound. The lyotropic columnar **LC** phase was induced for the mixture of imidazolium bis(trifluoromethylsuflonyl)imide by addition of small amount of water. And thermotropic columnar **LC** phase was observed for the mixture of 1-butyl-3-methylimidazolium hydrogen sulfate at room temperature. Both of mixtures were polymerized under UV light at **LC** phases to get free-standing polymer films, and columnar structure was well preserved in the films. The hydrous and anhydrous ionic conduction was studied for the polymer electrolytes with 1D nanostructure.

In chapter 3, the polymer films with 1D columnar **LC** were used as electrolytes in **iEAP** actuators. The **LC** polymer films sandwiched between two conductive polymer electrodes were triggered by alternating electric field in both dry and humid condition. The high bending strain was generated for both dry and humid **LC** polymer-based actuators under low-voltage, and a large blocking force was produced by dry actuator. The actuators were examined at various condition and the factors affecting on actuation performance were investigated, such as relative humidity, ion content in the electrolyte, ion species, and thickness of actuators.

In chapter 4, soft actuators based on columnar **LC** composite membranes with 3D nanostructure was obtained. A new design of rod-like zwitterionic molecules was prepared. And 3D continuous columnar **LC** phase was formed by mixing with ionic liquid. A stretchable **LC** composite membrane was given by addition of polymer matrix. The composite film showed inverted columnar structure when relative humidity was higher than 60% RH. The actuation performance of soft actuator composed by **LC** composite film was examined under various humid atmosphere and exhibited large displacement and quick response due to the 3D connecting ionic transport channels.

In chapter 5, an overall summary of this dissertation and the perspectives for **LC**-based actuator were given.

1.4 References

1. Mirvakili, S. M.; Hunter, I. W., Artificial Muscles: Mechanisms, Applications, and Challenges. *Adv. Mater.* **2018,** *30* (6), 1704407.

2. Asaka, K.; Okuzaki, H., *Soft Actuators: Materials, Modeling, Applications, and Future Perspectives*. 2nd ed.; Springer: Singapore, 2019.

3. Yang, Y.; Wu, Y.; Li, C.; Yang, X.; Chen, W., Flexible Actuators for Soft Robotics. *Adv. Intell. Syst.* **2020,** *2* (1), 1900077.

4. Hines, L.; Petersen, K.; Lum, G. Z.; Sitti, M., Soft Actuators for Small-Scale Robotics. *Adv. Mater.* **2017,** *29* (13).

5. Ilami, M.; Bagheri, H.; Ahmed, R.; Skowronek, E. O.; Marvi, H., Materials, Actuators, and Sensors for Soft Bioinspired Robots. *Adv. Mater.* **2021,** *33* (19), 2003139.

6. Bai, H.; Li, S.; Shepherd, R. F., Elastomeric Haptic Devices for Virtual and Augmented Reality. *Adv. Funct. Mater.* **2021,** *2009364* (n/a), 2009364.

7. Barreiros, J.; Claure, H.; Peele, B.; Shapira, O.; Spjut, J.; Luebke, D.; Jung, M.; Shepherd, R., Fluidic Elastomer Actuators for Haptic Interactions in Virtual Reality. *IEEE Robot. Autom. Lett.* **2019,** *4* (2), 277–284.

8. Bolzmacher, C.; Hafez, M.; Benali Khoudja, M.; Bernardoni, P.; Dubowsky, S., Polymer-Based Actuators for Virtual Reality Devices, *Smart Structures and Materials 2004: Electroactive Polymer Actuators and Devices (EAPAD),* International Society for Optics and Photonics, **2004**, 5385: 281–289.

9. Zhai, Y.; Wang, Z.; Kwon, K.-S.; Cai, S.; Lipomi, D. J.; Ng, T. N., Printing Multi-Material Organic Haptic Actuators. *Adv. Mater.* **2021,** *33* (19), 2002541.

10. Chang, L. F.; Liu, Y. F.; Yang, Q.; Yu, L. F.; Liu, J. Q.; Zhu, Z. C.; Lu, P.; Wu, Y. C.; Hu, Y., Ionic Electroactive Polymers Used in Bionic Robots: A Review. *J Bionic Eng* **2018,** *15* (5), 765–782.

11. Li, J. J.; Zhou, X.; Liu, Z. F., Recent Advances in Photoactuators and Their Applications in Intelligent Bionic Movements. *Adv. Opt. Mater.* **2020,** *8* (18), 16.

12. Chen, D.; Pei, Q., Electronic Muscles and Skins: A Review of Soft Sensors and Actuators. *Chem. Rev.* **2017,** *117* (17), 11239–11268.

13. Kim, J.; Kim, J. W.; Kim, H. C.; Zhai, L.; Ko, H.-U.; Muthoka, R. M., Review of Soft Actuator Materials. *Int. J. Precis. Eng. Manuf.* **2019,** *20* (12), 2221–2241.

14. McCracken, J. M.; Donovan, B. R.; White, T. J., Materials as Machines. *Adv. Mater.* **2020,** *32* (20), 1906564.

15. Liu, W.-C.; Chung, C.-H.; Hong, J.-L., Highly Stretchable, Self-Healable Elastomers from Hydrogen-Bonded Interpolymer Complex (HIPC) and Their Use as Sensitive, Stable Electric Skin. *ACS omega* **2018,** *3* (9), 11368–11382.

16. Klute, G. K. Artificial Muscles: Actuators for Biorobotic Systems. Ph.D. Dissertation, University of Washington, Washington, 1999.

17. Daerden, F.; Lefeber, D., Pneumatic Artificial Muscles: Actuators for Robotics and Automation. *Eur. J. Mech. Environ. Eng.* **2002,** *47*, 11–21.

18. Volder, M.; Reynaerts, D., Pneumatic and Hydraulic Microactuators: a Review. *J. Micromech. Microeng.* **2010,** *20,* 043001–043019.

19. Nespoli, A.; Besseghini, S.; Pittaccio, S.; Villa, E.; Viscuso, S., The High Potential of Shape Memory Alloys in Developing Miniature Mechanical Devices: A Review on Shape Memory Alloy Mini-Actuators. *Sens. Actuators, A* **2010,** *158* (1), 149–160.

20. Hager, M. D.; Bode, S.; Weber, C.; Schubert, U. S., Shape Memory Polymers: Past, Present and Future Developments. *Prog. Polym. Sci.* **2015,** *49,* 3–33.

21. Lai, A.; Du, Z.; Gan, C. L.; Schuh, C. A., Shape Memory and Superelastic Ceramics at Small Scales. *Science* **2013,** *341* (6153), 1505–1508.

22. Mirvakili, S. M.; Hunter, I. W., Multidirectional Artificial Muscles from Nylon. *Adv. Mater.* **2017,** *29* (4), 1604734.

23. Liu, L.; Liu, M.-H.; Deng, L.-L.; Lin, B.-P.; Yang, H., Near-Infrared Chromophore Functionalized Soft Actuator with Ultrafast Photoresponsive Speed and Superior Mechanical Property. *J. Am. Chem. Soc.* **2017,** *139* (33), 11333–11336.

24. Lu, H.-F.; Wang, M.; Chen, X.-M.; Lin, B.-P.; Yang, H., Interpenetrating Liquid-Crystal Polyurethane/Polyacrylate Elastomer with Ultrastrong Mechanical Property. *J. Am. Chem. Soc.* **2019,** *141* (36), 14364–14369.

25. Wang, E.; Desai, M. S.; Lee, S.-W., Light-Controlled Graphene-Elastin Composite Hydrogel Actuators. *Nano Lett.* **2013,** *13* (6), 2826–2830.

26. Bar-Cohen, Y., *Electroactive polymer (EAP) actuators as artificial muscles: reality, potential, and challenges*. SPIE press: 2004; Vol. 136.

27. Kwon, G. H.; Park, J. Y.; Kim, J. Y.; Frisk, M. L.; Beebe, D. J.; Lee, S.-H., Biomimetic Soft Multifunctional Miniature Aquabots. *Small* **2008,** *4* (12), 2148–2153.

28. Swann, J. M. G.; Topham, P. D., Design and Application of Nanoscale Actuators Using Block-Copolymers. *Polymers* **2010,** *2* (4), 454–469.

29. Raghavan, R. V.; Qin, J.; Yeo, L. Y.; Friend, J. R.; Takemura, K.; Yokota, S.; Edamura, K., Electrokinetic Actuation of Low Conductivity Dielectric Liquids. *Sens. Actuators, B* **2009,** *140* (1), 287–294.

30. Jung, K.; Koo, J. C.; Nam, J.-d.; Lee, Y. K.; Choi, H. R., Artificial Annelid Robot Driven by Soft Actuators. *Bioinspir. Biomim.* **2007,** *2* (2), S42–S49.

31. O'Halloran, A.; O'Malley, F.; McHugh, P., A Review on Dielectric Elastomer Actuators, Technology, Applications, and Challenges. *J. Appl. Phys.* **2008,** *104* (7), 071101.

32. Vargantwar, P. H.; Özçam, A. E.; Ghosh, T. K.; Spontak, R. J., Prestrain-Free Dielectric Elastomers Based on Acrylic Thermoplastic Elastomer Gels: A Morphological and (Electro)Mechanical Property Study. *Adv. Funct. Mater.* **2012,** *22* (10), 2100–2113.

33. Pelrine, R.; Kornbluh, R.; Pei, Q.; Joseph, J., High-Speed Electrically Actuated Elastomers with Strain Greater Than 100%. *Science* **2000,** *287* (5454), 836–839.

34. Jomaa, M.; Masenelli-Varlot, K.; Diguet, G.; Seveyrat, L.; Lebrun, L.; Wongtimnoi, K.; Vechambre, C.; Chenal, J.; Cavaillé, J., Modeling of Segmented Pure Polyurethane Electrostriction Behaviors Based on Their Nanostructural Properties. *Polymer* **2015,** *62*, 139–147.

35. Keplinger, C.; Li, T.; Baumgartner, R.; Suo, Z.; Bauer, S., Harnessing Snap-Through Instability in Soft Dielectrics to Achieve Giant Voltage-Triggered Deformation. *Soft Matter* **2012,** *8* (2), 285–288.

36. Zhang, Q. M.; Bharti, V.; Zhao, X., Giant Electrostriction and Relaxor Ferroelectric Behavior in

Electron-Irradiated Poly(vinylidene fluoride-trifluoroethylene) Copolymer. *Science* **1998,** *280* (5372), 2101–2104.

37. Huang, C.; Klein, R.; Xia, F.; Li, H.; Zhang, Q. M.; Bauer, F.; Cheng, Z. Y., Poly(vinylidene fluoride-trifluoroethylene) Based High Performance Electroactive Polymers. *IEEE Trans. Dielectr. Electr. Insul.* **2004,** *11* (2), 299–311.

38. Finkelmann, H.; Kock, H.-J.; Rehage, G., Investigations on Liquid Crystalline Polysiloxanes Liquid Crystalline Elastomers — a New Type of Liquid Crystalline Material. *Makromol. Chem., Rapid Commun.* **1981,** *2* (4), 317–322.

39. Lehmann, W.; Skupin, H.; Tolksdorf, C.; Gebhard, E.; Zentel, R.; Krüger, P.; Lösche, M.; Kremer, F., Giant Lateral Electrostriction in Ferroelectric Liquid-Crystalline Elastomers. *Nature* **2001,** *410* (6827), 447–450.

40. Okamoto, T.; Urayama, K.; Takigawa, T., Large Electromechanical Effect of Isotropic-Genesis Polydomain Nematic Elastomers. *Soft Matter* **2011,** *7* (22), 10585–10589.

41. Oguro, K., Bending of an Ion-Conducting Polymer Film-Electrode Composite by an Electric Stimulus at Low Voltage. *J. Micromach. Soc.* **1992,** *5*, 27–30.

42. Liu, S.; Liu, W.; Liu, Y.; Lin, J.-H.; Zhou, X.; Janik, M. J.; Colby, R. H.; Zhang, Q., Influence of Imidazolium-Based Ionic Liquids on the Performance of Ionic Polymer Conductor Network Composite Actuators. *Polym. Int.* **2010,** *59* (3), 321–328.

43. Naji, L.; Chudek, J. A.; Abel, E. W.; Baker, R. T., Electromechanical Behaviour of Nafion-Based Soft Actuators. *J. Mater. Chem. B* **2013,** *1* (19), 2502–2514.

44. Yilmaz, O. C.; Sen, I.; Gurses, B. O.; Ozdemir, O.; Cetin, L.; Sarıkanat, M.; Seki, Y.; Sever, K.; Altinkaya, E., The Effect of Gold Electrode Thicknesses on Electromechanical Performance of Nafion-Based Ionic Polymer Metal Composite Actuators. *Composites, Part B* **2019,** *165*, 747–753.

45. Nemat-Nasser, S.; Wu, Y., Comparative Experimental Study of Ionic Polymer–Metal Composites with Different Backbone Ionomers and in Various Cation Forms. *J. Appl. Phys.* **2003,** *93* (9), 5255–5267.

46. Liu, Y.; Ghaffari, M.; Zhao, R.; Lin, J.-H.; Lin, M.; Zhang, Q. M., Enhanced Electromechanical Response of Ionic Polymer Actuators by Improving Mechanical Coupling between Ions and Polymer Matrix. *Macromolecules* **2012,** *45* (12), 5128–5133.

47. Guo, D.; Han, Y.; Huang, J.; Meng, E.; Ma, L.; Zhang, H.; Ding, Y., Hydrophilic Poly(vinylidene Fluoride) Film with Enhanced Inner Channels for Both Water- and Ionic Liquid-Driven Ion-Exchange Polymer Metal Composite Actuators. *ACS Appl. Mater. Interfaces* **2019,** *11* (2), 2386–2397.

48. Park, J. H.; Han, M. J.; Song, D. S.; Jho, J. Y., Ionic Polymer–Metal Composite Actuators Obtained from Radiation-Grafted Cation- and Anion-Exchange Membranes. *ACS Appl. Mater. Interfaces* **2014,**

6 (24), 22847–22854.

49. Gonçalves, R.; Tozzi, K. A.; Saccardo, M. C.; Zuquello, A. G.; Scuracchio, C. H., Nafion-Based Ionomeric Polymer/metal Composites Operating in the Air: Theoretical and Electrochemical Analysis. *J. Solid State Electrochem.* **2020,** *24* (8), 1845–1856.

50. MohdIsa, W.; Hunt, A.; HosseinNia, S. H., Sensing and Self-Sensing Actuation Methods for Ionic Polymer-Metal Composite (IPMC): A Review. *Sensors* **2019,** *19* (18).

51. Baughman, R. H.; Cui, C.; Zakhidov, A. A.; Iqbal, Z.; Barisci, J. N.; Spinks, G. M.; Wallace, G. G.; Mazzoldi, A.; Rossi, D. D.; Rinzler, A. G.; Jaschinski, O.; Roth, S.; Kertesz, M., Carbon Nanotube Actuators. *Science* **1999,** *284* (5418), 1340–1344.

52. Fukushima, T.; Asaka, K.; Kosaka, A.; Aida, T., Fully Plastic Actuator through Layer-by-Layer Casting with Ionic-Liquid-Based Bucky Gel. *Angew. Chem., Int. Ed.* **2005,** *44* (16), 2410–2413.

53. Mukai, K.; Asaka, K.; Sugino, T.; Kiyohara, K.; Takeuchi, I.; Terasawa, N.; Futaba, D. N.; Hata, K.; Fukushima, T.; Aida, T., Highly Conductive Sheets from Millimeter-Long Single-Walled Carbon Nanotubes and Ionic Liquids: Application to Fast-Moving, Low-Voltage Electromechanical Actuators Operable in Air. *Adv. Mater.* **2009,** *21* (16), 1582–1585.

54. Imaizumi, S.; Kato, Y.; Kokubo, H.; Watanabe, M., Driving Mechanisms of Ionic Polymer Actuators Having Electric Double Layer Capacitor Structures. *J. Phys. Chem. B* **2012,** *116* (16), 5080–5089.

55. Torop, J.; Sugino, T.; Asaka, K.; Jänes, A.; Lust, E.; Aabloo, A., Nanoporous Carbide-Derived Carbon based Actuators Modified with Gold Foil: Prospect for Fast Response and Low Voltage Applications. *Sens. Actuators, B* **2012,** *161* (1), 629–634.

56. Terasawa, N.; Ono, N.; Mukai, K.; Koga, T.; Higashi, N.; Asaka, K., A Multi-Walled Carbon Nanotube/polymer Actuator that Surpasses the Performance of a Single-Walled Carbon Nanotube/polymer Actuator. *Carbon* **2012,** *50* (1), 311–320.

57. Takeuchi, I.; Asaka, K.; Kiyohara, K.; Sugino, T.; Terasawa, N.; Mukai, K.; Shiraishi, S., Electromechanical Behavior of a Fully Plastic Actuator Based on Dispersed Nano-Carbon/Ionic-Liquid-Gel Electrodes. *Carbon* **2009,** *47* (5), 1373–1380.

58. Sugino, T.; Kiyohara, K.; Takeuchi, I.; Mukai, K.; Asaka, K., Improving the Actuating Response of Carbon Nanotube/ionic Liquid Composites by the Addition of Conductive Nanoparticles. *Carbon* **2011,** *49* (11), 3560–3570.

59. Li, J.; Ma, W.; Song, L.; Niu, Z.; Cai, L.; Zeng, Q.; Zhang, X.; Dong, H.; Zhao, D.; Zhou, W.; Xie, S., Superfast-Response and Ultrahigh-Power-Density Electromechanical Actuators Based on Hierarchal Carbon Nanotube Electrodes and Chitosan. *Nano Lett.* **2011,** *11* (11), 4636–4641.

60. Liu, S.; Liu, Y.; Cebeci, H.; de Villoria, R. G.; Lin, J.-H.; Wardle, B. L.; Zhang, Q. M., High Electromechanical Response of Ionic Polymer Actuators with Controlled-Morphology Aligned Carbon

Nanotube/Nafion Nanocomposite Electrodes. *Adv. Funct. Mater.* **2010,** *20* (19), 3266–3271.

61. Wu, G.; Li, G. H.; Lan, T.; Hu, Y.; Li, Q. W.; Zhang, T.; Chen, W., An Interface Nanostructured Array Guided High Performance Electrochemical Actuator. *J. Mater. Chem. A* **2014,** *2* (40), 16836–16841.

62. Wu, G.; Wu, X.; Xu, Y.; Cheng, H.; Meng, J.; Yu, Q.; Shi, X.; Zhang, K.; Chen, W.; Chen, S., High-Performance Hierarchical Black-Phosphorous-Based Soft Electrochemical Actuators in Bioinspired Applications. *Adv. Mater.* **2019,** *31* (25), 1806492.

63. Baughman, R. H., Conducting Polymers in Redox Devices and Intelligent Materials Systems. *Makromol. Chem., Macromol. Symp.* **1991,** *51* (1), 193–215.

64. Jager, E. W. H.; Smela, E.; Inganäs, O., Microfabricating Conjugated Polymer Actuators. *Science* **2000,** *290* (5496), 1540.

65. Alici, G.; Huynh, N. N., Predicting Force Output of Trilayer Polymer Actuators. *Sens. Actuators, A* **2006,** *132* (2), 616–625.

66. Sansiñena, J. M.; Gao, J.; Wang, H. L., High-Performance, Monolithic Polyaniline Electrochemical Actuators. *Adv. Funct. Mater.* **2003,** *13* (9), 703–709.

67. Wu, Y.; Yang, Y.; Li, C.; Li, Y.; Chen, W., Flexible and Electroactive Textile Actuator Enabled by PEDOT:PSS/MOF-Derivative Electrode Ink. *Front. Bioeng. Biotechnol.* **2020,** *8* (212).

68. Wu, Y. J.; Minamikawa, H.; Nakazumi, T.; Hara, Y., Actuation Properties of Paper Actuators Fabricated Using PEDOT/PSS Electrode Films. *J. Oleo Sci.* **2020,** *69* (10), 1331–1337.

69. Okuzaki, H.; Takagi, S.; Hishiki, F.; Tanigawa, R., Ionic Liquid/polyurethane/PEDOT:PSS Composites for Electro-active Polymer Actuators. *Sens. Actuators, B* **2014,** *194*, 59–63.

70. Põldsalu, I.; Rohtlaid, K.; Nguyen, T. M. G.; Plesse, C.; Vidal, F.; Khorram, M. S.; Peikolainen, A.-L.; Tamm, T.; Kiefer, R., Thin Ink-jet Printed Trilayer Actuators Composed of PEDOT:PSS on Interpenetrating Polymer Networks. *Sens. Actuators, B* **2018,** *258*, 1072–1079.

71. Zolfagharian, A.; Kouzani, A. Z.; Khoo, S. Y.; Moghadam, A. A. A.; Gibson, I.; Kaynak, A., Evolution of 3D Printed Soft Actuators. *Sens. Actuators, A* **2016,** *250*, 258–272.

72. Feng, C.; Hemantha Rajapaksha, C. P.; Jákli, A., Ionic Elastomers for Electric Actuators and Sensors. *Engineering* **2021,** *7* (5), 581–602.

73. Hara, S.; Zama, T.; Takashima, W.; Kaneto, K., Tris(trifluoromethylsulfonyl)methide-Doped Polypyrrole as a Conducting Polymer Actuator with Large Electrochemical Strain. *Synth. Met.* **2006,** *156* (2), 351–355.

74. Kim, S.-S.; Jeon, J.-H.; Kee, C.-D.; Oh, I.-K., Electro-Active Hybrid Actuators based on Freeze-Dried Bacterial Cellulose and PEDOT:PSS. *Smart Mater. Struct.* **2013,** *22* (8), 085026.

75. Green, M. D.; Wang, D.; Hemp, S. T.; Choi, J.-H.; Winey, K. I.; Heflin, J. R.; Long, T. E., Synthesis

of Imidazolium ABA Triblock Copolymers for Electromechanical Transducers. *Polymer* **2012,** *53* (17), 3677–3686.

76. Gao, R.; Wang, D.; Heflin, J. R.; Long, T. E., Imidazolium Sulfonate-Containing Pentablock Copolymer–Ionic Liquid Membranes for Electroactive Actuators. *J. Mater. Chem.* **2012,** *22* (27), 13473–13476.

77. Lee, J.-W.; Yu, S.; Hong, S. M.; Koo, C. M., High-Strain Air-Working Soft Transducers Produced from Nanostructured Block Copolymer Ionomer/silicate/ionic Liquid Nanocomposite Membranes. *J. Mater. Chem. C* **2013,** *1* (24), 3784–3793.

78. Kim, O.; Kim, H.; Choi, U. H.; Park, M. J., One-Volt-Driven Superfast Polymer Actuators based on Single-Ion Conductors. *Nat. Commun.* **2016,** *7,* 13576.

79. Goodby, J. W.; Collings, P. J.; Kato, T.; Tschierske, C.; Gleeson, H.; Raynes, P.; Vill, V., Eds.; *Handbook of liquid crystals*, John Wiley & Sons: **2014**.

80. Collings, P. J., *Liquid crystals: nature's delicate phase of matter*, 2nd ed.; Princeton University Press: Princeton, NJ, **2001**.

81. Tschierske, C., Development of Structural Complexity by Liquid-crystal Self-Assembly. *Angew. Chem. Int. Ed.* **2013,** *52* (34), 8828–8878.

82. Goossens, K.; Lava, K.; Bielawski, C. W.; Binnemans, K., Ionic Liquid Crystals: Versatile Materials. *Chem. Rev.* **2016,** *116* (8), 4643–4807.

83. Tschierske, C., Non-Conventional Liquid Crystals—the Importance of Micro-Segregation for Self-Organisation. *J. Mater. Chem.* **1998,** *8* (7), 1485–1508.

84. Stupp, S. I.; LeBonheur, V.; Walker, K.; Li, L. S.; Huggins, K. E.; Keser, M.; Amstutz, A., Supramolecular Materials: Self-Organized Nanostructures. *Science* **1997,** *276* (5311), 384–389.

85. Cho, B.-K., Nanostructured Organic Electrolytes. *RSC Adv.* **2014,** *4* (1), 395–405.

86. Kato, T.; Yoshio, M.; Ichikawa, T.; Soberats, B.; Ohno, H.; Funahashi, M., Transport of Ions and Electrons in Nanostructured Liquid Crystals. *Nat. Rev. Mater.* **2017,** *2* (4).

87. Kato, T.; Mizoshita, N.; Kishimoto, K., Functional Liquid-Crystalline Assemblies: Self-Organized Soft Materials. *Angew. Chem. Int. Ed.* **2005,** *45* (1), 38–68.

88. Yoshizawa, M.; Hirao, M.; Ito-Akita, K.; Ohno, H., Ion Conduction in Zwitterionic-Type Molten Salts and their Polymers. *J. Mater. Chem.* **2001,** *11* (4), 1057–1062.

89. Armand, M.; Endres, F.; MacFarlane, D. R.; Ohno, H.; Scrosati, B., Ionic-Liquid Materials for the Electrochemical Challenges of the Future. *Nat. Mater.* **2009,** *8* (8), 621–629.

90. Ueda, S.; Kagimoto, J.; Ichikawa, T.; Kato, T.; Ohno, H., Anisotropic Proton-Conductive Materials formed by the Self-Organization of Phosphonium-Type Zwitterions. *Adv. Mater.* **2011,** *23* (27), 3071–3074.

91. Ichikawa, T.; Kato, T.; Ohno, H., 3D Continuous Water Nanosheet as a Gyroid Minimal Surface Formed by Bicontinuous Cubic Liquid-Crystalline Zwitterions. *J. Am. Chem. Soc.* **2012,** *134* (28), 11354–11357.

92. Yoshio, M.; Kagata, T.; Hoshino, K.; Mukai, T.; Ohno, H.; Kato, T., One-Dimensional Ion-Conductive Polymer Films: Alignment and Fixation of Ionic Channels formed by Self-Organization of Polymerizable Columnar Liquid Crystals. *J. Am. Chem. Soc.* **2006,** *128* (16), 5570–5577.

93. Lu, F.; Gao, X.; Dong, B.; Sun, P.; Sun, N.; Xie, S.; Zheng, L., Nanostructured Proton Conductors Formed via in Situ Polymerization of Ionic Liquid Crystals. *ACS Appl. Mater. Interfaces* **2014,** *6* (24), 21970–21977.

94. Kobayashi, T.; Li, Y.-x.; Ono, A.; Zeng, X.-b.; Ichikawa, T., Gyroid Structured Aqua-Sheets with Sub-Nanometer Thickness Enabling 3D Fast Proton Relay Conduction. *Chem. Sci.* **2019**, *10* (25), 6245–625.

Chapter 2 Ion-Conductive Nanostructured Polymer Films Formed by Photopolymerization of Columnar Liquid-Crystalline Monomers

2.1 Introduction

Nanostructured ionic liquid-crystalline (**LC**) assemblies are currently attracting widespread interest for applications in batteries and separation membranes.[1-4] The intension herein is to develop columnar **LC** polymer electrolytes forming proton transport highways which will pave way to better fuel cells and ion-conducting polymer actuators. The developments of proton transporting columnar and bicontinuous cubic **LC** assemblies with one-dimensionally anisotropic channels and three-dimensionally interconnected channels were reported, respectively.[5-6] These materials were obtained by co-assembly of zwitterionic **LC** molecules and Brønsted acids or dihydroxy-functionalized **LC** molecules and protic ionic liquids. The nanosegregation and intermolecular interactions play a great key role in controlling the self-organized nanostructures and enhancing proton transport. The author wondered if the co-assembly of zwitterionic molecules and more mobile protic ionic liquids can induce the **LC** phases at ambient temperature and enhance the proton conductivity. The binary mixtures of solid imidazolium-based zwitterionic salt and bis(trifluoromethylsulfonyl)imide acid (**HTFSI**) were reported to form ambient temperature ionic liquids by Yoshizawa and Ohno.[7] This concept was further extended to the design of high proton-conductive thermotropic and lyotropic **LC** materials.[8-11] In addition, Watanabe and coworkers developed high proton-conducting protic ionic liquids by the neutralization of imidazole and **HTFSI**, which can be applicable to fuel cell electrolytes.[12] Therefore, the self-assembly of protic ionic liquids containing **TFSI** anion and taper-shaped polymerizable zwitterionic molecules was assumed to induce columnar **LC** phases and the subsequent photopolymerization could produce prominent nanostructured polymer films preserving the fluidic proton transport highways in the solid matrices (Figure 2-1).

Chapter 2

Here, a new family of proton-conductive columnar **LC** polymer films based on room-temperature lyotropic columnar **LC** monomers composed of a zwitterionic molecule **1** having three acrylate groups at the extremity of the alkyl chains, protic ionic liquid **2**, and water was reported (Figure 2-2). In addition, anhydrous proton conductive columnar **LC** polymer films were also developed by co-assembly of **1** and protic ionic liquid **3** (**[BMIM]$^+$[HSO$_4$]$^-$**). The incorporation of a larger content of ionic liquid into the center of the columns has successfully provided a highly ion-conductive polymer film with mechanical robustness.

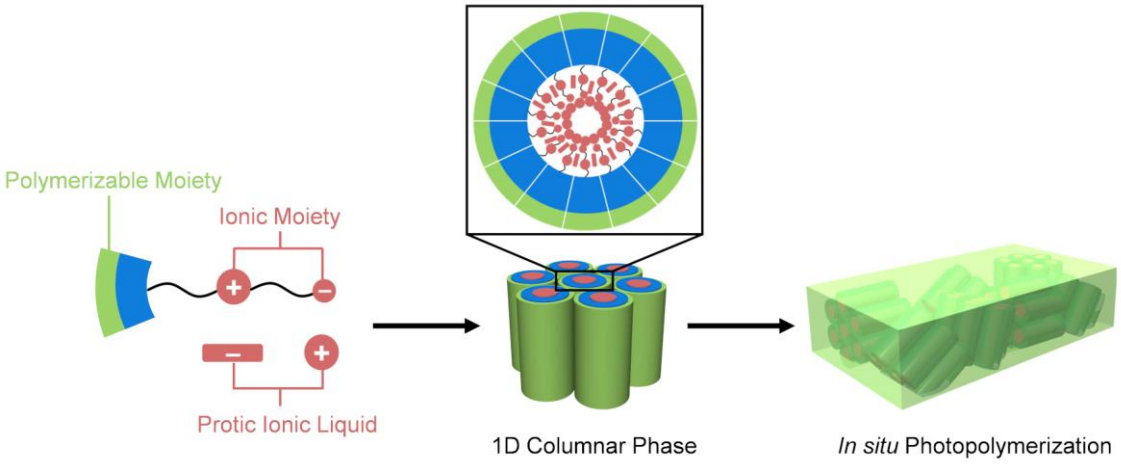

Figure 2-1. Schematic illustration of the columnar **LC** self-assembly of polymerizable zwitterionic compound, protic ionic liquid, and water and fabrication of polymer film with one-dimensionally proton-conductive nanochannels by *in situ* photopolymerization.

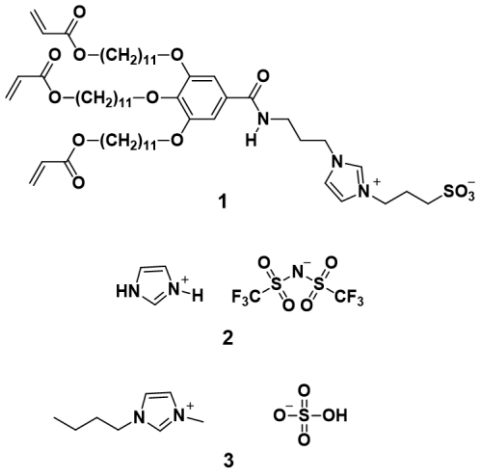

Figure 2-2. Chemical structures of polymerizable taper-shaped zwitterionic molecule **1** and protic ionic liquids **2** and **3**.

Chapter 2

2.2 Experimental section

2.2.1 General materials and methods

All ^{1}H NMR spectra were recorded on a JEOL JNM-AL30/BZ spectrometer at 300 MHz for solutions in $CDCl_3$ or D_2O. The chemical shifts (δ) are quoted in ppm using tetramethylsilane (δ = 0.00), as the internal standard for $CDCl_3$ solutions and a solvent residual peak (δ = 4.79) for a D_2O solution. All ^{13}C NMR spectra for $CDCl_3$ solutions were recorded on JEOL ECZ400S at 100 MHz, using the solvent peak as internal reference (δ = 77.0). High-resolution mass spectrometry (HRMS) measurements were carried out by using a BRUKER microTOF II. FT-IR spectra were taken with a BRUKER FT-IR ALPHA II spectrometer with a single reflection diamond ATR module. Elemental analysis for CHNS was carried out by using an ELEMENTAR vario EL cube. All reagents were purchased from Sigma-Aldrich, Tokyo Chemical Industry, Kanto Chemicals, and Wako Pure Chemical Industries and used without further purification.

2.2.2 Synthesis

Zwitterionic compound **1** was synthesized according to the procedures shown in Scheme 2-1. Intermediate compound **4** was prepared by the condensation reaction of tris(11'-acryloyloxyundecyloxy)benzoic acid[13] and 1-(3-aminopropyl)imidazole. Protic ionic liquid **2** was obtained by the reaction of **HTFSI** and imidazole in the modified synthetic procedure.[14]

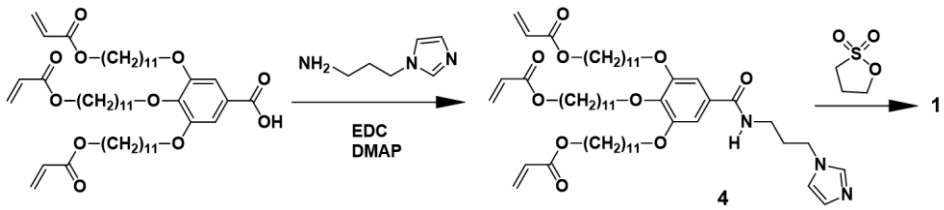

Scheme 2-1. Synthetic route of compound **1**.

Synthesis of Compound 4

In the synthesis, 1-(3-aminopropyl)imidazole (0.46 g, 3.70 mmol) was added dropwise to a dry dichloromethane solution (10 mL) of tris(11'-acryloyloxyundecyloxy)benzoic acid (1.56 g, 1.85 mmol), 4-(dimethylamino)pyridine (DMAP) (0.02 g, 0.20 mmol), and 1-ethyl-3-(3-

dimethylaminopropyl) carbodiimide hydrochloride (EDC) (0.71 g, 3.70 mmol) in a light-resistant three-necked round-bottom flask at 0 °C. The reaction mixture was warmed to room temperature and stirred for 18 h. The solvent was removed by evaporation. The residue was purified by flash column silica gel chromatography using an eluent of $CHCl_3$/MeOH = 95/5 to give compound **3** (1.28 g, 1.35 mmol, 73% yield) as a white solid.

^{1}H NMR (300 MHz, $CDCl_3$) : δ [ppm] = 7.52 (s, 1H), 7.07 (s, 1H), 6.97 (s, 1H), 6.92 (s, 2H), 6.39 (dd, *J* = 17.2, 1.5 Hz, 3H), 6.12 (dd, *J* = 17.2, 10.3 Hz, 3H), 5.80 (dd, *J* = 10.3, 1.5 Hz, 3H), 4.14 (t, *J* = 6.8 Hz, 6H), 4.08-3.96 (m, 7H), 3.46 (q, *J* = 6.4 Hz, 2H, 2.16 (m, 2H), 1.85-1.59 (m, 20H), 1.46-1.29 (m, 40H). ^{13}C NMR (100 MHz, $CDCl_3$): δ [ppm] = 167.8, 166.4, 153.1, 137.1, 130.5, 129.7, 129.1, 128.7, 119.0, 105.8, 73.5, 69.4, 64.8, 44.9, 37.4, 31.4, 30.4, 29.7, 29.6, 29.6, 29.4, 29.3, 29.3, 28.7, 29.1, 26.0. FT-IR (ATR): ν = 3111, 2916, 2850, 1723, 1643, 1582, 1496, 1467, 1410, 1338, 1296, 1187, 1114, 1093, 1055, 981, 869, 839, 809, 721, 667 cm^{-1}. Elemental analysis calcd (%) for $C_{55}H_{87}N_3O_{10}$: C, 69.51, H, 9.23, N, 4.42; found: C, 69.61, H, 8.94, N, 4.46. HRMS (ESI): molecular weight: 950.3120 ($C_{55}H_{87}N_3O_{10}$); m/z calcd for $[C_{55}H_{88}N_3O_{10}]^+$: 950.6464 ($[M+H]^+$); found: 950.6412.

Synthesis of Compound 1

Compound **4** (0.51 g, 0.54 mmol) was dissolved in dichloromethane (5 mL) in a light resistant container. Then, 1,3-propanesultone (0.33 g, 2.69 mmol) was added dropwise. The reaction mixture was stirred at room temperature for 3 days. The crude product was purified by silica gel chromatography (elution with $CHCl_3$/MeOH = 9/1). Subsequent purification using a recycling preparative HPLC (eluent: $CHCl_3$) afforded a white solid of compound **1** (0.40 g, 0.37 mmol, 69% yield).

^{1}H NMR (300 MHz, $CDCl_3$) : δ [ppm] = 9.76 (s, 1H), 8.19 (d, *J* = 6.6 Hz, 1H), 7.18 (s, 2H), 7.12 (s, 1H), 6.39 (dd, *J* = 17.2, 1.5 Hz, 3H), 6.11 (dd, *J* = 17.2, 10.3 Hz, 3H), 5.81 (dd, *J* = 10.4, 1.6 Hz, 3H), 4.40 (m, 4H), 4.14 (t, *J* = 6.8 Hz, 6H), 4.04 (t, *J* = 6.2 Hz, 3H), 3.96 (t, *J* = 6.6 Hz, 1H), 3.52 (d, *J* = 5.1 Hz, 2H), 2.78 (m, 2H), 2.30 (d, *J* = 5.5 Hz, 4H), 1.82-1.61 (m, 20H), 1.37 (d, *J* = 49.5 Hz, 42H). ^{13}C NMR (100 MHz, $CDCl_3$): δ [ppm] = 167.9, 166.4, 152.9, 140.7, 130.5, 129.1, 128.7, 122.2, 121.8, 106.1, 73.5, 69.3, 64.8, 47.2, 29.8, 29.7, 29.6, 29.5, 29.4, 29.3, 28.7, 26.2, 26.0. FT-IR (ATR): ν = 2918, 2851, 1721, 1636, 1579, 1540, 1497, 1469, 1409, 1330, 1296, 1184, 1113, 1038, 982, 810, 766, 603, 523 cm^{-1}. Elemental analysis calcd

(%) for $C_{58}H_{93}N_3O_{13}S$: C, 64.96, H, 8.74, N, 3.92, S, 2.99; found: C, 65.10, H, 8.39, N, 3.85, S, 3.14.

Synthesis of Protic Ionic Liquid 2

Solid imidazole (0.494 g, 7.26 mmol) in a glass vial was added to solid **HTFSI** (2.04 g, 7.26 mmol) in a dry nitrogen atmosphere in a glove box. The exothermic reaction immediately occurred and gave a colorless liquid. The obtained liquid was stirred for 5 minutes and turned to a white solid at an ambient temperature. The solid was recrystallized from a hot acetone. After filtration of the solid by a suction funnel under a nitrogen atmosphere, a white powder of **2** was dried under vacuum at 80 °C overnight (2.322 g, 6.65 mmol, 92% yield). ^{1}H NMR (300 MHz, D_2O): δ [ppm] = 8.73 (s, 1H), 7.53 (s, 2H). ^{13}C NMR (100 MHz, D_2O): δ [ppm] = 133.3, 119.7 (q, J = 318.2 Hz), 118.9. FT-IR (ATR): ν = 3266, 1585, 1340, 1184, 1127, 1049, 789, 769, 739, 650, 632, 614, 570, 511 cm^{-1}.

Preparation of the LC Mixtures

The **LC** monomers composed of **1** and protic ionic liquids **2** or **3** with different molar ratios (**M1**/**2(x)** or **M1/3(x)**, **x** denotes the mole% of **2** or **3** in the mixtures) were prepared as follows. The solid samples of **1**, **2** or **3**, and 1.0 wt% 2,2-dimethyl-2-phenylacetophenone as a photoinitiator were mixed in anhydrous tetrahydrofuran and MeOH. The solvent was slowly evaporated at 40 °C in a light-resistant container. The resultant mixtures were dried in a vacuum oven at 35 °C for 48 hours. For lyotropic sample **M1/2(x)**, 15% distilled water was added to the mixtures in a vial. Centrifugation of the mixtures (13500 rpm, 14 min) gave the lyotropic columnar liquid crystals at room temperature. Three mixtures (x = 40, 50, and 60) of **M1/2(x)** and **M1/3(x)** were used for the characterization of liquid crystallinity and ionic conductivity.

2.2.3 Characterization of LC properties and ionic-conductivity measurements

The optical texture of **LC** mixtures was observed by using a polarizing optical microscope (POM) (Olympus BX51N-31P-O3, Olympus Corporation, Tokyo, Japan), equipped with a digital camera DP22 and a temperature control system (LINKAM T95-HS, LTS420E). X-ray diffraction (XRD) measurements were carried out by using a Rigaku MiniFlex 600 (Ni-filtered

Cu Kα radiation, Rigaku Corporation, Tokyo, Japan) diffractometer equipped with an Anton Par thermal control system BTS 500. Differential scanning calorimetry (DSC) measurements were conducted with a NETZCH DSC 3500 Sirius system at a scanning rate of 10 °C/min.

The ionic-conductivity measurement cell consists of a pair of indium tin oxide (**ITO**) coated glasses with a polyimide tape spacer with a hole of 3 mm punch diameter. The monomer was filled into the hole of the sandwich cell and polymerized by UV irradiation. The ionic conductivities of polymerized samples with **LC** and isotropic molecular arrangement were measured as a function of temperature by an alternating current impedance method, using a Metrohm Autolab PGSTAT128N (frequency: 100 Hz–10 MHz, applied voltage: 0.6 V) with a temperature controller. The impedance data were fitted by the equivalent circuit consisting of a phase constant element and a parallel RC element. The ionic-conductivities were calculated by the equation: $\sigma = d/(R \cdot S)$, where σ is the conductivity (S cm^{-1}), d is the sample thickness (cm), R is the bulk resistance (Ω), and S is the area (cm^2) of sample. The value of R was obtained from the intercept of the semicircle on the real axis of impedance in Nyquist plots.

2.3 Results and discussion

2.3.1 LC Properties and ionic conductivity of lyotropic LC compounds

Zwitterionic compound **1** alone in the dry state shows no thermotropic liquid crystallinity and exhibits the crystal-isotropic liquid transition at 90 °C on heating. Protic ionic liquid **2** shows a melting point at 73 °C.[14] The monomeric mixtures of **1** and **2** in the dry state (**M1/2(40)**, **M1/2(50)**, and **M1/2(60)**, the values in the parentheses are the mol% of **2** in the mixture of **1** and **2**) form isotropic liquids at ambient temperature. On the other hand, the addition of 15 wt% water to the mixtures has successfully induced the lyotropic columnar **LC** phases (**Col**) at ambient temperature. Fan-like textures assignable to a lyotropic columnar phase are observed for all mixtures under crossed polarizers, as shown in Figure 2-3. The **LC** texture is observed up to 100 °C. The optical birefringence gradually disappears on further heating and the mixture eventually becomes the isotropic liquid state by the evaporation of water.

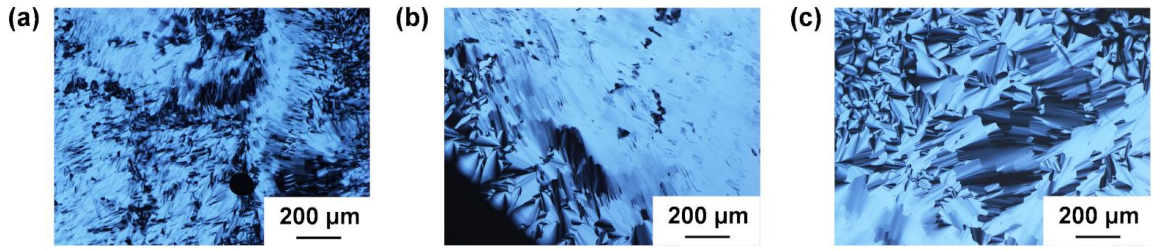

Figure 2-3. Polarizing optical micrographs of (a) **M1/2(40)** at 65 °C, (b) **M1/2(50)** at 80 °C, (c) **M1/2(60)** at 60 °C.

The interactions of **1** and **2** were examined by FT-IR measurements (Figure 2-4). The amide N-H stretching peak at 3320 cm^{-1} of **1** is shifted to 3409 cm^{-1} by the addition of **2**. This result suggests that the intermolecular hydrogen bonds between the amide group weaken by an increase in the distance between the amide groups accompanied by the formation of an ion pair between the imidazolium cation of **1** and the **TFSI** anion of **2** and/or the formation of a hydrogen bond between the amide N-H and the anion. In addition, **M1/2(60)** shows the C-H stretching band of the imidazolium ring at 3153 cm^{-1}, which is in the almost same position as that observed for **2**, whereas zwitterion **1** showed three C-H stretching peaks between 3000 and 3200 cm^{-1}. These results also support the pairing of the imidazolium cation of **1** with the **TFSI** anion of **2**. Moreover, the C-SO_2-N absorption peak[15] at 1127 cm^{-1} of **2** is shifted to 1136 cm^{-1} upon the addition of **1**. This high-wavenumber shift may be caused by the weakening of the interaction associated with the ion-pairing between the imidazolium ring of **1** and the **TFSI** anion of **2**

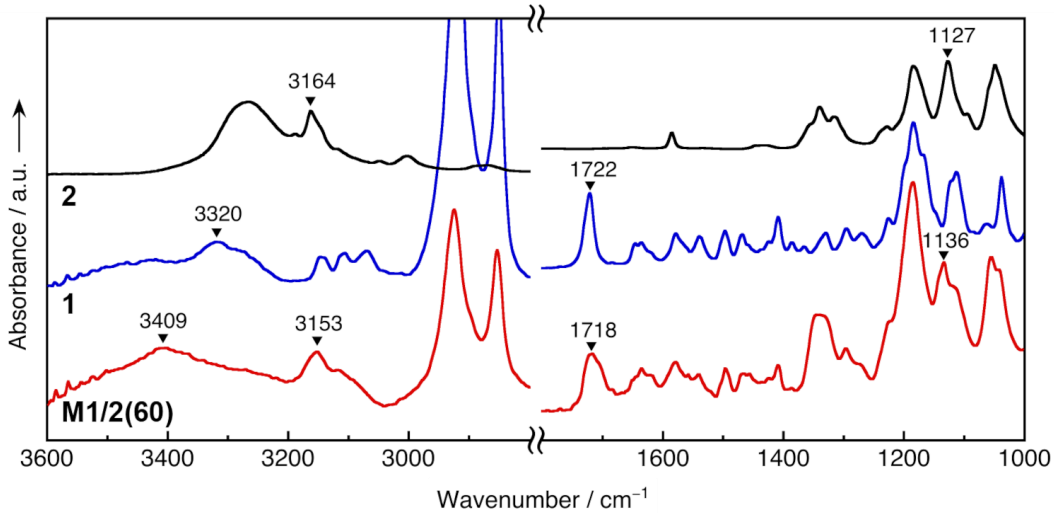

Figure 2-4. FT-IR spectra of **2** (black line), **1** (blue line), and **M1/2 (60)** (red line) at room temperature.

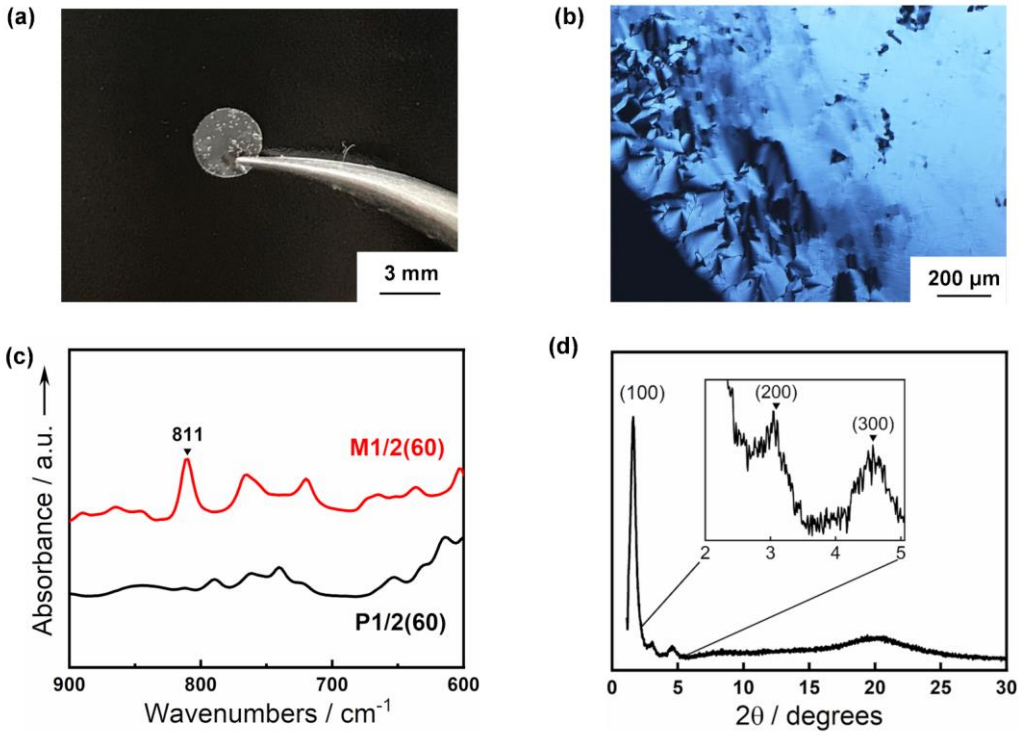

Figure 2-5. (a) Photograph of a free-standing polymer film of **P1/2(60)** at room temperature. The thickness is 458 μm. (b) POM image of **P1/2(50)**. (c) FT-IR spectra of **M1/2(60)** and **P1/2(60)**. (d) XRD pattern of **P1/2(50)** at room temperature.

compared to that of the protonated imidazole of **2** and the anion. On the other hand, the C=O stretching bands of **1** and **M1/2(60)** were observed at 1722 and 1718 cm^{-1}, respectively. This result indicates that the C=O group of **1** is not involved in the interactions between **2**.

In-situ photopolymerization of the **LC** mixtures was carried out to obtain ion-conductive polymer films preserving the columnar nanostructures. The monomeric **LC** mixtures **M1/2(40)**, **M1/2(50)**, and **M1/2(60)** containing 1.0 wt% 2,2-dimethyl-2-phenylacetophenone as a photoinitiator were sandwiched between two **ITO** glasses and the thickness was controlled by a polyimide spacer. The UV light irradiation (365 nm, 30 mW cm^{-2}) with a Xenon lamp for 10 min was performed for the polydomain sample in the Col phase at room temperature. This irradiation led to the formation of a translucent free-standing polymer film (Figure 2-5a). No significant change in the columnar alignment is observed after polymerization under POM observation (Figure 2-5b). The UV polymerization was confirmed by FT-IR measurements. The C=C absorption band of acrylate moiety was observed at 811 cm^{-1} for the monomeric **M1/2(60).** In contrast, the polymer film of **P1/2(60)** obtained after UV irradiation shows no

C=C absorption peak (Figure 2-5c).

The XRD pattern of the **P1/2(50)** at room temperature shows three peaks at 55.9 (2θ = 1.58°), 29.6 (2.98°), and 19.1 Å (4.62°) (Figure 2-5d). These peaks are assumed to be the (100), (200), and (300) reflections of a columnar arrangement, respectively although the *d*-spacing ratio does not exactly match 1: 1/2: 1/3. Assuming that the polymer films formed a hexagonal columnar structure, the intercolumnar distance (*a*) was calculated to be 66 Å by the following equation: $a = 2 \langle d_{100} \rangle / \sqrt{3}$, $\langle d_{100} \rangle = (d_{100} + 2\, d_{200} + 3 d_{300})/3$. The number (*n*) of molecules per unit cell in a hexagonal lattice was estimated to be approximately 14 according to the equation: $n = (\sqrt{3} N_A a^2 h \rho)/2M$, where N_A is Avogadro's number (6.02×10^{23} mol^{-1}), *h* is the average height of the stratum of a column (4.45 Å from a halo peak at 19.9°), *M* is the average molecular weight of **M1/2(50)** (M = 710.84 g mol^{-1}), and the density (ρ) was assumed to be 1.0 g cm^{-3}.

An increase in the amount of protic ionic liquid **2** in the mixture tends to decrease the intercolumnar distance rather than column expansion. The *a* values of **P1/2(40)**, **P1/2(50)**, and **P1/2(60)** are estimated to be 68, 66, and 64 Å, respectively. These results also suggest that the protic ionic liquid dissociates and forms an ion pair with the zwitterionic moiety organized into the center of columns. The increase in the electrostatic and hydrogen-bonded interactions results in column shrinkage.

In order to clarify the influence of polymer nanostructures on ionic conductivity, amorphous polymer films were prepared by photopolymerization of **M1/2(40)**, **M1/2(50)**, and **M1/2(60)** in an isotropic liquid state (**P1/2(x)-Iso**). Figure 2-6 shows the temperature dependence of ionic conductivities for **P1/2(x)** with the columnar nanostructures and amorphous **P1/2(x)-Iso**. The ionic conductivity for all samples increases with the increase in temperature due to the thermal activation of the molecular motility. The increase of the protic ionic liquid content in the mixtures leads to the enhancement of ionic conductivities because of the increase in the number of ionic carriers. It is significant that nanostructured polymers **P1/2(x)** exhibits 100-1000 times higher conductivities than the corresponding amorphous polymers **P1/2(x)-Iso**. For example, the conductivity value of **P1/2(60)** is 4.2×10^{-4} S cm^{-1} at 20 °C, which is 1000 times higher than **P1/2(60)-Iso** at the same temperature (4.5×10^{-7} S cm^{-1}). These results suggest that the formation of ionic nanochannels is essential to enhance ion transport in the solid polymer matrices. The maximum conductivity reaches 3.0×10^{-3} S cm^{-1} at 80 °C for **P1/2(60)**. Protic ionic liquid **2** was reported to show the proton conductivity of 2.7×10^{-2} S cm^{-1} at 130 °C.[14]

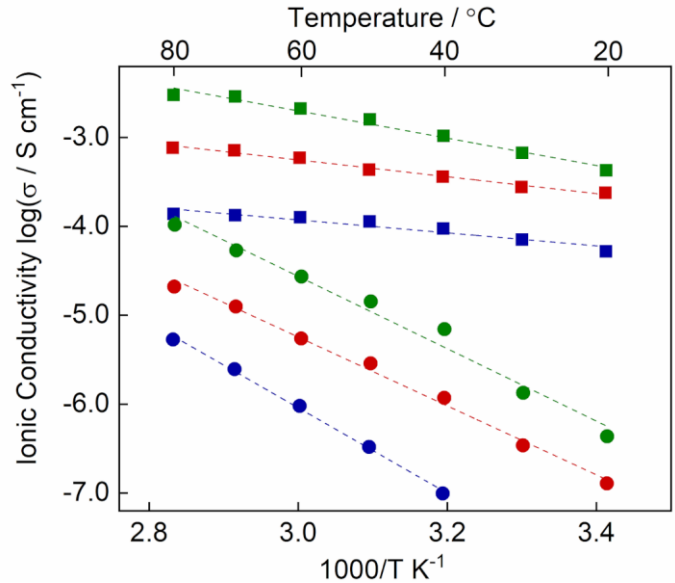

Figure 2-6. Ionic conductivities of polymers **1/2(40)** (blue), **1/2(50)** (red), and **1/2(60)** (green) with Col_h **LC** molecular arrangement (square) and isotropic molecular arrangement (round). The dashed lines are fits by the Arrhenius equation to the data.

It is worthwhile to note that high ion-conductive and flexible solid polymer electrolytes could be obtained by self-assembly of the solid protic salt, the insulating zwitterionic monomer, and a small amount of water.

The temperature-dependent ionic conductivity (σ) can be fitted by the Arrhenius Equation, $\sigma = \sigma_0 \exp(-E_a/RT)$, where R is a gas constant and T is the temperature in Kelvin. The activation energies (E_a) of **P1/2(60)** and **P1/2(60)-Iso** were estimated from the slope ($-E_a/R$) of lines to be 13 kJ mol^{-1} and 28 kJ mol^{-1}, respectively. The lower activation energy for **P1/2(60)** is attributed to the formation of continuous hydrogen-bonded networks consisting of the protonated imidazole, the sulfonate anion of **2**, and water. More interestingly, the E_a value of **P1/2(x)** tends to decrease with the decrease in the protic ionic liquid content. The E_a values of **P1/2(50)** and **P1/2(40)** are 7.9 and 6.1 kJ mol^{-1}, respectively. These results indicate that the introduction of proton accepting vacant sites is a great key to constitute the effective proton-conductive pathways in the **LC** polymers.

Recently, Ichikawa and coworkers developed proton-conductive bicontinuous cubic **LC** polymer films based on the self-assembly of polymerizable zwitterionic molecules and **HTFSI** in the presence of water.[9] The three-dimensionally continuous channel structures allowed significantly higher proton conduction of 9.9×10^{-2} S cm^{-1} at 70 °C and lower activation energy

of 2.2 kJ mol^{-1} attributable to proton conduction via the Grotthuss mechanism. The materials presented herein show two-orders of magnitude lower conductivities. The difference in ionic conductivity between columnar and bicontinuous cubic zwitterionic **LC** polymers seems to be mainly due to the differences in channel connectivity, proton conduction mechanism, and size of mobile ions. Bicontinuous cubic **LC** assemblies have the advantage of channel connectivity without alignment control. However, uniaxially oriented columnar **LC** channels are expected to show faster ion transport ability due to their linearity. In the present study, the vertical alignment of the columnar structures across the polymer films was not achieve. These oriented materials have great potentials for the development of ion-conductive polymer actuators that can achieve both high speed oscillation and high-power generation. For such application, fast transport of large ions is required. In this context, by employing hydrated and protonated imidazole as cation species, the mechanically robust nanostructured polymer films exhibiting good ionic conductivities in the order of 10^{-4}–10^{-3} S cm^{-1} at ambient temperature were successfully fabricated.

2.3.2 LC Properties and ionic conductivity of thermotropic LC compounds

Selecting the appropriate ionic liquids as nonvolatile electrolytes is the key to inducing nanostructured **LC** phases and achieving high ionic conductivity. It was found that the monomeric mixture of zwitterionic compound **1** and commercially available protic ionic liquid **3** (**M1/3(40)**, **M1/3(50)**, and **M1/3(60)**) exhibited thermotropic **Col LC** phases at room temperature. The phase transition behavior of **M1/3(x)** was determined by DSC measurements and POM observations. All of samples exhibited fan-shaped textures typically for the **Col** phase at room temperature (Figure 2-7). In the DSC traces (Figure 2-8), the crystal (**Cr**)–**LC** phase transitions were observed during the cooling and heating processes, whereas the **Col LC** to isotropic (**Iso**) phase transition was not detected. The Col-Iso transition temperatures were determined by POM observation. The **Cr**–**Col** and **Col**-**Iso** transition temperatures decreased when increasing the amount of ionic liquid **3** during heating process. For example, the **Col**-**Iso** transitions of **M1/3(60)**, **M1/3(50)**, and **M1/3(40)** gradually occur from 130, 147, and 155 °C, respectively and formed the biphasic phases of isotropic liquids and partially polymerized solids. The thermal stabilization of **Col** phase was decreased by increase in the content of protic

ionic liquid, which was ascribed to be caused by disorder of columnar structure by the formation of intermolecular hydrogen bonding between the hydrogen sulfonate of **3** and sulfonate anion of **1**.

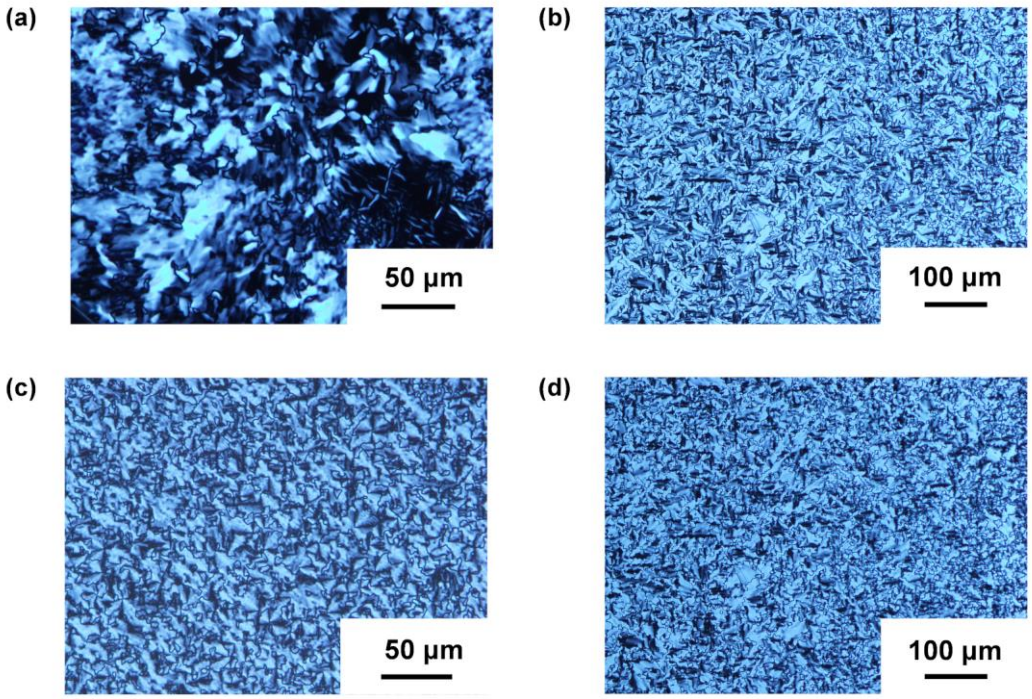

Figure 2-7. POM images of (a) **M1/3(40)**; (b) **M1/3(50)**; (c) **M1/3(60)**; (d) **P1/3(50)** at room temperature.

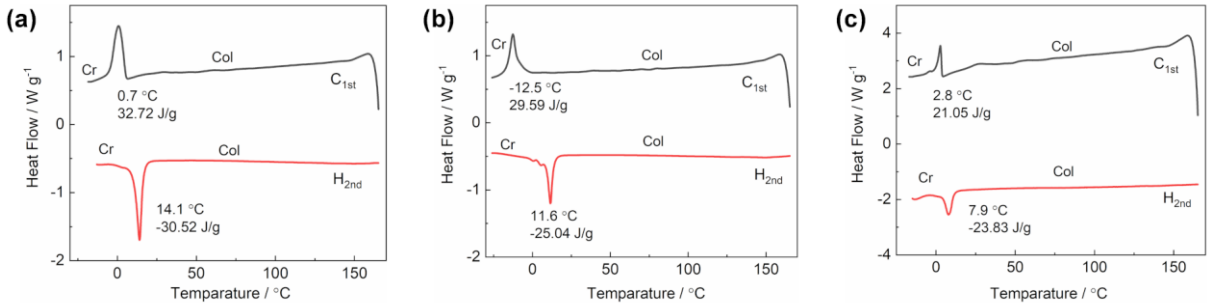

Figure 2-8. DSC traces of (a) **M1/3(40)**; (b) **M1/3(50)**; (c) **M1/3(60)** during first cooling and second heating processes.

The columnar nanostructured polymer films **P1/3(x)** were successfully prepared by *in situ* photopolymerization of **M1/3(x)** under the same condition as for the preparation of **P1/2(x)**. No obvious change in the Col **LC** texture was observed after polymerization (Figure 2-7d). The

XRD patterns of **P1/3(x)** show a sharp peak at 2θ = 1.7°–2.0° attributable to the (100) diffraction of a Col phase and a broad halo at 2θ = 20° (Figure 2-9). Assuming that the polymer films formed a hexagonal columnar structure, the intercolumnar distance (a) was calculated by the following equation: $a = 2\ d_{100}/\sqrt{3}$. The average height of the stratum of a column was determined from the halo peak at 2θ = 20.3°. The value of d-spacings, Miller Indices, lattice parameters (a) of hexagonal columnar phase, and number of molecules (n) per unit cell in the hexagonal lattice were summarized in the Table 2-1.

The intercolumnar distance of **P1/3(x)** tends to increase with the amount of **3**, which is the opposite with **P1/2(x)**. In case of **P1/3(x)**, confining **3** to the center of the ionic columns without charge compensating for the ion-pairing with the zwitterionic moiety of **1** may lead to the expansion of columns. The a values of anhydrous **P1/3(40)**, **P1/3(50)**, and **P1/3(60)** are estimated to be 52, 53, and 59 Å which are smaller than that of corresponding **P1/2(x)** forming aqueous channels. The intercolumnar distance was increased after polymerization, for example the a value of **M1/3(50)** was calculated to be 51 Å which was smaller than that of **P1/3(50)**. It was due to the connection of acrylate groups at the extremity of alkyl chains surrounding the outside of each columnar domain during inter-columnar crosslinking.

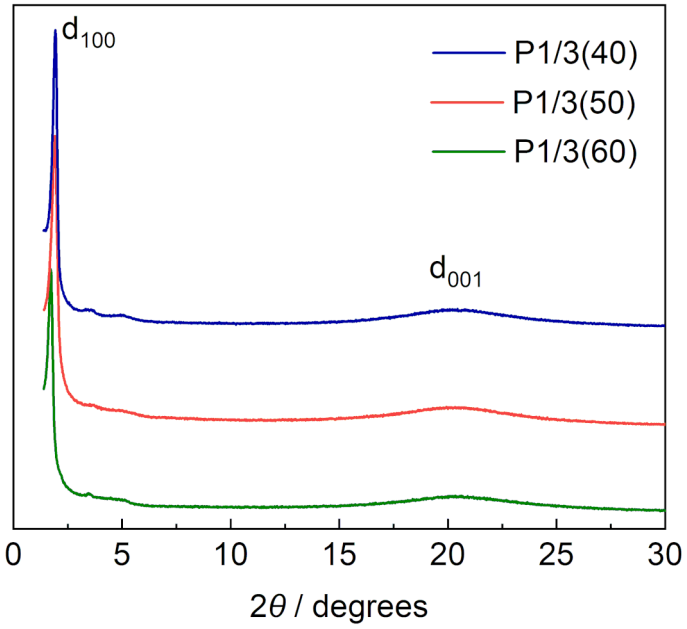

Figure 2-9. XRD patterns of **P1/3(x)** at ambient condition.

Table 2-1. Observed *d*-spacings, Miller Indices, lattice parameters (*a*) of hexagonal columnar phase, and number of molecules (*n*) per unit cell in the hexagonal lattice estimated from the XRD measurements of **P1/2(x)** and **P1/3(x)** at ambient condition.

	x	*d* (Å)	Miller Index	*a* (Å)	*n*
P1/2(x)	40	60.9 4.4	100 001	70.3	14
	50	55.9 4.4	100 001	64.5	14
	60	55.2 4.3	100 001	63.7	14
P1/3(x)	40	45.4 4.4	100 001	52.4	8
	50	46.2 4.3	100 001	53.3	10
	60	51.2 4.4	100 001	59.1	14

The ionic conductivities of **M1/3(x)** and **P1/3(x)** at room temperature are shown in Figure 2-10. As same as **P1/2(x)**, the higher the ion contents, the higher the ionic conductivity. The conductivity decreased after polymerization. For example, **M1/3(50)** shows room-temperature ionic conductivity of 2.1×10^{-6} S cm^{-1}, which is 10 times higher than **P1/3(50)** (2.1×10^{-7} S cm^{-1}). The polymerization increases the viscosity of the insulating matrix surrounding the ion channels, which reduces the ion diffusion. The conductivity of **P1/3(x)** was about 10^2–10^4 times lower than those of **P1/2(x)** at room temperature. The conductivity value of **P1/2(40)** is 5.2×10^{-5} S cm^{-1} at 20 °C, while that of **P1/3(40)** at the same temperature is only 2.3×10^{-9} S cm^{-1}. The high conductivity for **P1/2(x)** may be attributed to the proton hopping via the hydrogen-bonding networks of the incorporated water molecules, zwitterion, and doped protic salt. In contrast, the low conductivity for **P1/3(x)** should be caused by the bulk diffusion of cation and anion in the absent of water.

To date, a variety of materials design methods have been employed improving proton-conductive polymer electrolytes for fuel cell and actuator applications. For the realization of fast proton conduction, one of the most general approaches is to create hydrogen-bonding networks of water molecules in the polymer matrices. In contrast, for ionic electroactive actuator applications, the formation of electric double layer at electrode–electrolyte interfaces

and the difference in the volume and transference number of cations and anions are significant impacts on the bending actuation performance. It is assumed that the anhydrous polymer electrolyte **P1/3(x)** should exhibit better actuator performance than **P1/2(x)**.

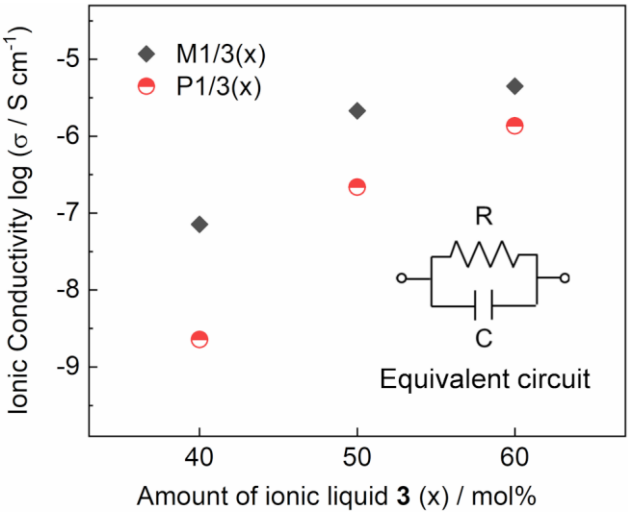

Figure 2-10. Ionic conductivities of **M1/3(x)** and **P1/3(x)** at room temperature. (The inset is equivalent circuit of measured system.)

2.4 Conclusions

A new columnar **LC** self-assembly of polymerizable zwitterionic compound consisting of an imidazolium sulfobetaine moiety and imidazolium-based ionic liquids was designed. The lyotropic and thermotropic columnar **LC** phase were induced by co-assembly with different ionic liquids. The mechanically stable and free-standing polymer films preserving the columnar nanostructures were obtained by *in-situ* photopolymerization of the columnar **LC** mixtures. The ionic conductivity for lyotropic **LC** resultant polymer films with polydomain columnar orientation was exhibited in the order of 10^{-4}–10^{-3} S cm^{-1} at ambient temperature. The nanostructured polymers were examined to show 100–1000 times higher conductivity compared to the corresponding amorphous polymer films. The thermotropic **LC** resultant polymer films with polydomain columnar architecture shows anhydrous ionic conductivity in the order of 10^{-6}–10^{-9} S cm^{-1} at ambient temperature. Control of the number of vacancy sites consisting of the sulfonate anion is of importance for efficient proton transport. Two-component noncovalent approach for the development of ionic **LC** materials has advantages not only for

tuning the ion transport properties but also for optimizing nanostructures and temperature range of **LC** phases. Nanostructured ion-conductive polymer films have great potential for applications such as fuel cells, filtration membranes, and polymer actuators in both humid and dry condition.

2.5 References

1. Hamaguchi, K.; Kuo, D.; Liu, M.; Sakamoto, T.; Yoshio, M.; Katayama, H.; Kato, T., Nanostructured Virus Filtration Membranes Based on Two-Component Columnar Liquid Crystals. *ACS Macro Lett.* **2018,** *8* (1), 24–30.

2. Henmi, M.; Nakatsuji, K.; Ichikawa, T.; Tomioka, H.; Sakamoto, T.; Yoshio, M.; Kato, T., Self-Organized Liquid-Crystalline Nanostructured Membranes for Water Treatment: selective permeation of ions. *Adv. Mater.* **2012,** *24* (17), 2238–2241.

3. Wang, C.; Cao, S.; Li, P.; Tan, S.; Wu, Y., Anisotropic Films Photopolymerized from Aligned Cross-Linkable Gemini Ammonium Liquid Crystals for Ion Conduction. *J. Appl. Polym. Sci.* **2019,** *136* (15), 47349.

4. Bara, J. E.; Kaminski, A. K.; Noble, R. D.; Gin, D. L., Influence of Nanostructure on Light Gas Separations in Cross-Linked Lyotropic Liquid Crystal Membranes. *J. Membr. Sci.* **2007,** *288* (1-2), 13–19.

5. Yamashita, A.; Yoshio, M.; Soberats, B.; Ohno, H.; Kato, T., Use of a Protic Salt for the Formation of Liquid-Crystalline Proton-Conductive Complexes with Mesomorphic Diols. *J. Mater. Chem. A* **2015,** *3* (45), 22656–22662.

6. Soberats, B.; Yoshio, M.; Ichikawa, T.; Taguchi, S.; Ohno, H.; Kato, T., 3D Anhydrous Proton-Transporting Nanochannels formed by Self-Assembly of Liquid Crystals Composed of a Sulfobetaine and a Sulfonic Acid. *J. Am. Chem. Soc.* **2013,** *135* (41), 15286–15289.

7. Yoshizawa, M.; Ohno, H., Anhydrous Proton Transport System based on Zwitterionic Liquid and HTFSI. *Chem. Commun.* **2004,** (16), 1828–1829.

8. Ueda, S.; Kagimoto, J.; Ichikawa, T.; Kato, T.; Ohno, H., Anisotropic Proton-Conductive Materials Formed by the Self-Organization of Phosphonium-Type Zwitterions. *Adv. Mater.* **2011,** *23* (27), 3071–3074.

9. Kobayashi, T.; Li, Y.-x.; Ono, A.; Zeng, X.-b.; Ichikawa, T., Gyroid Structured Aqua-Sheets with Sub-Nanometer Thickness Enabling 3D Fast Proton Relay Conduction. *Chem. Sci.* **2019,** *10* (25), 6245–6253.

10. Ichikawa, T.; Okafuji, A.; Kato, T.; Ohno, H., Induction of an Infinite Periodic Minimal Surface by Endowing An Amphiphilic Zwitterion with Halogen-Bond Ability. *ChemistryOpen* **2016,** *5* (5), 439–444.

11. Ichikawa, T.; Kato, T.; Ohno, H., 3D Continuous Water Nanosheet as a Gyroid Minimal Surface Formed by Bicontinuous Cubic Liquid-Crystalline Zwitterions. *J. Am. Chem. Soc.* **2012,** *134* (28), 11354–11357.

12. Yasuda, T.; Watanabe, M., Protic Ionic Liquids: Fuel Cell Applications. *MRS Bull.* **2013,** *38* (7), 560–566.

13. Smith, R. C.; Fischer, W. M.; Gin, D. L., Ordered Poly(p-phenylenevinylene) Matrix Nanocomposites via Lyotropic Liquid-Crystalline Monomers. *J. Am. Chem. Soc.* **1997,** *119* (17), 4092–4093.

14. Susan, M. A. B. H.; Noda, A.; Mitsushima, S.; Watanabe, M., Brønsted Acid–Base Ionic Liquids and Their Use as New Materials for Anhydrous Proton Conductors. *Chem. Commun.* **2003,** (8), 938.

15. Wu, A.; Lu, F.; Sun, P.; Qiao, X.; Gao, X.; Zheng, L., Low-Molecular-Weight Supramolecular Ionogel Based on Host-Guest Interaction. *Langmuir* **2017,** *33* (49), 13982–13989.

Chapter 3 Electroactive Actuators Based on Columnar Ionic Liquid-Crystalline Polymer Membrane Electrolytes Forming 1D Ionic Channels

3.1 Introduction

Soft actuators have been widely developed into the applications including artificial muscles,[1-3] soft robotics,[4-5] haptics.[6-7] In recent years, **iEAP** actuators driven by ion movement were drawn extensive attraction in the field of nanomaterials because they can be operated under low voltage (typically 1–3V) and work in both dry and humid environment[8]. A number of materials for fabricating **iEAP** actuators have emerged. Among these, ionic polymers,[9] bucky gels,[10-11], and cellulose nanofibers[12-14] as electronic components were well-studied. Conventionally, amorphous ion gels and hydrated ionic polymers have been employed as polymer electrolytes. But, as the ions are transported by segmental motion of the polymer backbone or by diffusion in the entangled polymer chains, the ionic conductivities are in the range of 10^{-4}–10^{-7} S cm^{-1} at ambient temperature. Therefore, a new efficient electrolyte design that can transport a large amount of ions in a shorter distance is important to achieve fast and low-voltage-driven actuation. Moreover, **iEAP** actuators that can withstand humid working environment such as biomedical, marine robotics need to be developed. The intention in this chapter is to introduce 1D ionic transporting nanochannels into polymer electrolytes to achieve large bending displacement under low operating voltage.

Liquid crystals (**LC**) as versatile materials have exhibited remarkable performance for transportation of ions in application of batteries, fuel cells, and photoluminescent materials.[15-17] The nanostructured **LC** phases constructed well-organized inner channels providing effective transporting pathways for mobile ions. In pioneer's researches, self-assembly of mesogens can induce columnar (1D), lamellar (2D), and cubic (3D) architectures can extremely enhanced ion conduction.[18-23] The author is interested to see whether the actuator performance can be improved by employing nanostructured liquid crystals as the electrolyte in the **iEAP** actuator. In chapter 2, a new family of lyotropic and thermotropic columnar **LC** electrolyte polymer films was successfully prepared. These nanostructured polymers forming 1D nanochannels can be

used to fabricate **iEAP** actuators. Moreover, the actuators based on the lyotropic and thermotropic columnar **LC** electrolyte that can work at both dry and humid environments were also expected to adapt a wider range of applications.

To explore the advantages of nanostructured **LC** ion-conducting materials in application of actuators, a new design of soft actuators based on **LC** polymer electrolytes which constructed 1D columnar ionic nanochannels was developed in this chapter. The **LC** polymer electrolytes sandwiching by two conductive polymer electrodes exhibited large bending strain and block force. And various factors affecting the actuation were also investigated in this section.

3.2 Experimental section

Preparation of P1/2(x) and P1/3(x) electrolyte films

The monomeric mixture **M1/2(x)** and **M1/3(x)** were sandwiched between glass substrate and polyimide-taped glass substrate. The space was controlled by polyimide spacer (60 μm). For lyotropic mixture **M1/2(x)**, the cell was directly placed under UV light at room temperature. For thermotropic mixture **M1/3(x)**, the sample was heated to isotropic state and then cooled down to room temperature. All the samples were irradiated by UV light (365 nm, 30 mW cm^{-2}) for 1 min. After photopolymerization, the samples were peeled off from glass plates after heating to 70 °C. The free-standing polymer films with a thickness of 64 ± 3 μm were obtained.

Preparation of PEDOT:PSS electrode films

Ethylene glycol (6 wt% to **PEDOT:PSS**) was added to the **PEDOT:PSS** aqueous solution (Clevios PH1000, 1.3 wt%). The mixed solution (2 mL) was cast in a defined area (6.5 × 7 cm) partitioned by polyimide tapes onto a glass substrate. The sample was dried at 60 °C for 20 min to get a gelatinous film and then transferred to Teflon plate and dried at 120 °C for 2 h in a vacuum oven. The **PEDOT:PSS** film was peeled off using tweezers from the substrate and immersed into the 98 wt% H_2SO_4 aqueous solution for 30 min. The acid treated film was washed by water and then dried on a Teflon plate at 100 °C in vacuo. The electrical conductivity of the films (600 ± 50 S cm^{-1}) was evaluated by a four-point method with a Loresta-GX (MCP-T700, Nittoseiko Analytech Co., Ltd.).

Chapter 3

Preparation of P1/2(x)- and P1/3(x)-based actuators

The polymer films **P1/2(x)** and **P1/3(x)** were sandwiched between two **PEDOT: PSS** films by pressing at room temperature (AS ONE Co., Small hot press machine H300-10D). The dimension of actuators in this chapter was 13 mm in length, 4 mm in width and 74 ± 3 μm in thickness.

Actuator performance test

The actuator strip with a copper foil on one end was clamped between two stainless steel electrodes connected to a potentiostat (Hokudo Denko, HAL3001A). Alternating square-wave voltages or DC voltages generated by a function generator (NF, WF1973) were controlled by the potentiostat and applied to the actuator strip. The working actuator length was 10 mm. The bending displacement was measured by using a laser meter (Keyence, LK-HD500). The laser was irradiated perpendicular to the surface of actuator at 2 mm away from the tip of strip. The blocking force was measured by the load sensor and force detection monitor (KYOWA LTS-50GA/KYOWA WGA-680A). The signals of voltage, current, displacement, and force were recorded in a MEMORY HiLOGGER (HIOKI LR8431) with a time interval of 50 ms. The measurements in dry condition were performed in ambient atmosphere with a relative humidity 25 ± 5%. The measurements in humid condition were performed in a humidity-controlled glove box and the samples were stored in humid atmosphere for 1h before measurements to arrive equilibrium state.

The peak-to-peak bending strain (ε) bending strain was calculated following the equation: [10]

$$\varepsilon = 2\delta d \times 100/(\delta^2 + L^2)$$

where δ is peak-to-peak displacement (mm), d is the thickness of actuator (mm), and L is the working length (mm) of actuator strip.

3.3 Results and discussion

The working mechanism of **LC** polymer-based ionic electroactive polymer actuators is the difference in volume of cations and anions accumulated in the interfaces between electrolyte and cathode and anode. The size and movement of ions in the electrolyte play a key role in

actuation response. Here, the actuation performance of **LC** electrolyte-based actuator was evaluated in both dry and humid condition. Various factors affecting the actuation were discussed in this section such as relative humidity (RH), ion contents in the polymer, ion species and the thickness of electrolytes.

3.3.1 Relative humidity

The actuation performance was influenced by relative humidity in the working environment. When applied an AC voltage, the transferred current shows a spike signal immediately in 70% and 80% RH condition while only weak peak in 60% RH (Figure 3-1). The spike signal was caused by the rapid charging/discharging process in the interface between electrolyte and electrodes. The water molecules involved in actuator can facilitate the dissociation of cations and anions of **IL**, which resulting in fast charging/discharging and larger transferred current in the higher RH environment. For example, the response current in 80% RH is 8 mA in about 10 times higher than that in 60 % RH (0.7 mA). The larger current indicates more accumulated ions in the surface of electrolytes in higher humid condition. However, the displacement in 80%

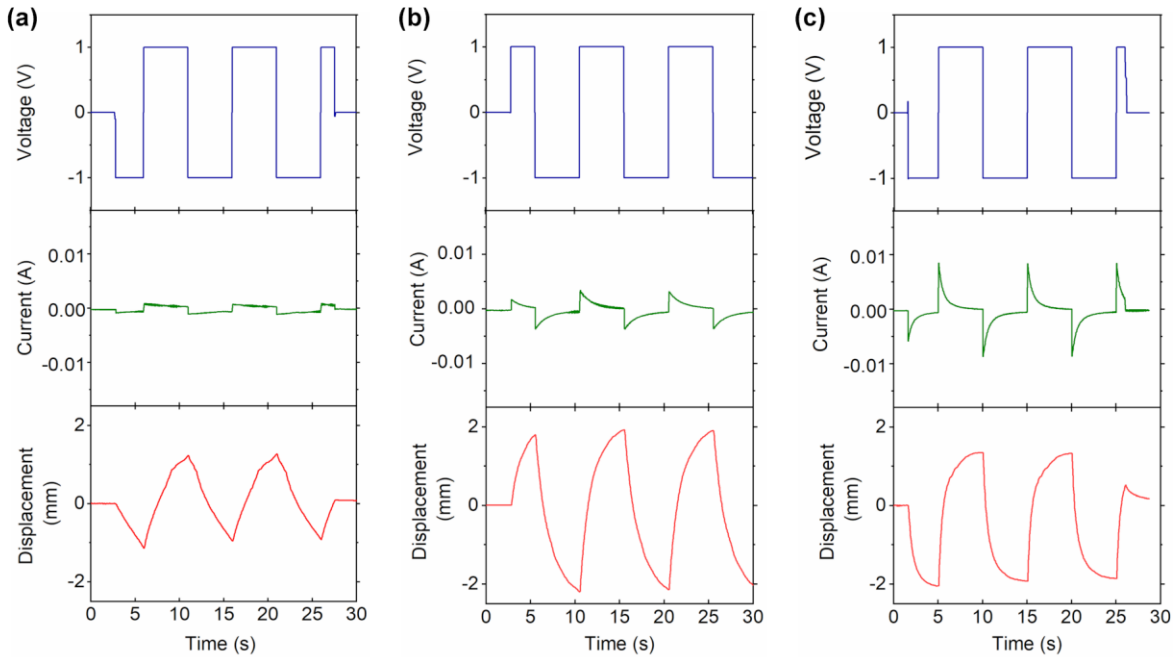

Figure 3-1. Voltage, transient current, and displacement vs. time plots of **P1/2(50)** actuators under an applying voltage of ±1 V with a frequency of 0.1 Hz in the various humid environment: (a) 60% RH; (b) 70% RH; (c) 80% RH.

RH environment was smaller than that in 70% RH environment. The reason was supposed to be the soften of electrolyte by adsorbing water that cannot induce the enough deformation of electrodes. The maximum bending strain of **P1/2(50)** was achieved to be 0.84% under an AC voltage of ±2 V with a frequency of 0.1 Hz at 70% RH environment.

The response time of **P1/2(50)** actuators in different RH condition was tested under an AC voltage of ±0.5 V with a frequency of 0.01 Hz (Figure 3-2). The shortest response time for reaching the equilibrium position is 10 s achieved in 80% RH condition. It needs 29 s to reach equilibrium bending for actuators working in 60% RH condition. It means the actuation cannot reach saturated state when the frequency of electric field is higher 0.02 Hz in 60% RH environment. For 50% RH condition, the actuation did not get to equilibrium in whole electric cycle. The longer response time is due to the slower movement of ions in the electrolyte. It can be attributed to the gradual dissociation of **IL**s and larger hindrance in transporting in the low humidity environment. The actuators exhibit good stability and can maintain same deformation value after working over 600 cycles without any loss under an AC voltage of ±1 V at 1 Hz at 80% RH (Figure 3-3).

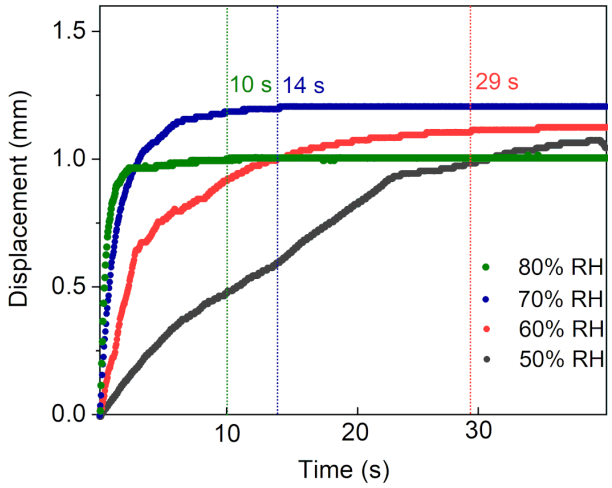

Figure 3-2. Response time of **P1/2(50)** actuators under an AC voltage of ±0.5 V with a frequency of 0.01 Hz at various RH condition.

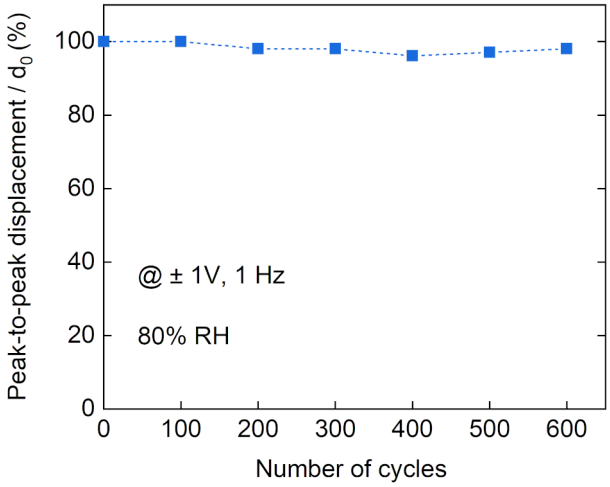

Figure 3-3. Cycling stability of the **P1/2(60)** actuators under an AC voltage of ±1 V at 1 Hz at 80% RH. The peak-to-peak displacement for each cycle is normalized by the initial displacement value (d_0).

3.3.2 Ion content

The ion content moving in the electrolyte is critical for achieving rapid and large bending. The accumulated charge can be improved by applying higher voltage to accelerate the dissociation of cations and anions of **IL**. The relationship between peak-to-peak displacement, applied voltage, and frequency of **P1/2(40)** actuators was investigated under ±0.5, ±1, and ±2 V with frequencies of 0.01, 0.1, and 1.0 Hz in the 70% RH environment (Figure 3-4a). The **P1/2(40)** actuators working under an AC of ±2 V with a frequency of 0.01 Hz can move over 3.9 mm and generated a high bending strain of 0.76%. On the other hand, the peak-to-peak displacement of **P1/2(40)** actuators decreased to 0.3 mm with a bending strain of 0.08% under same voltage with a frequency of 1 Hz. The reduced displacement by increased frequency of applied voltage can be ascribed to that the time of a voltage cycle is not enough for ions to dissociate and move across the electrolyte film to reach the surface. The photographs of actuator working under various applied voltage with 0.01 Hz in the 60% RH environment are shown in Figure 3-4b.

The bending strain dependence of ion content in the **LC** assemblies was studied for **P1/2(40)**, **P1/2(50)**, and **P1/2(60)** under various applied voltage and frequency (Figure 3-5a). At high frequency of 1 Hz, the bending strain was linearly improved by increasing the amount of ionic liquid **2**. The **P1/2(60)** actuator exhibited a strain range of 0.06-0.22%, while the **P1/2(40)** actuator shows no bending at 1 Hz, basically. At 0.1 Hz, the bending strain was strongly

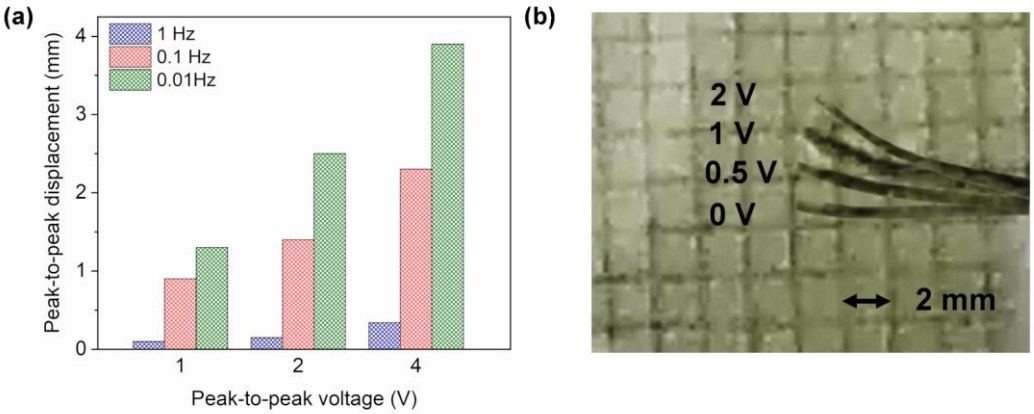

Figure 3-4. (a) Peak-to-peak displacement of **P1/2(40)** under applying voltages of ±0.5, ±1, and ±2 V with frequencies of 0.01, 0.1, and 1.0 Hz in the 70% RH environment; (b) Photographs of **P1/2(60)** under various applied voltage with 0.01 Hz in the 60% RH environment.

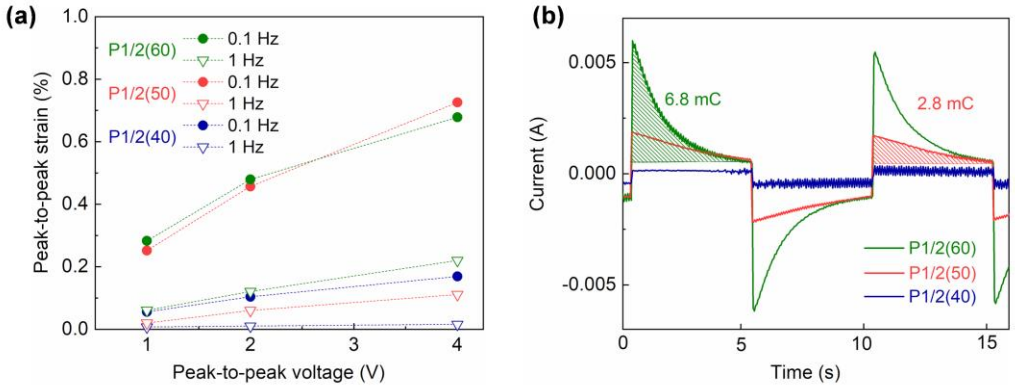

Figure 3-5. (a) Comparison of peak-to-peak strain for **P1/2(x)** actuators with different mole ratio of **2** in 60% RH environment; (b) Accumulated charge of **P1/2(x)** actuators with various mole ratio of **2** under an AC of ±2 V with a frequency of 0.1 Hz in 60% RH environment.

increased when the mole ratio of 2 in the **LC** assemblies was increased from 40 to 50. For example, the value of strain for P1/2(50) was 0.72% under an AC of ±2 V which was 4 times higher than that of **P1/2(40)** (0.16%). However, further increasing the content of **2**, there is no obvious difference in bending strain between **P1/2(50)** and **P1/2(60)** at 0.1 Hz in whole testing voltage range. The reason is that the ionic conductivity of **P1/2(50)** was about 10 times higher than that of **P1/2(40)** (2.3×10^{-4} S cm^{-1} vs. 5.13×10^{-5} S cm^{-1}) at room temperature (Figure 2-6) while as same order with that of **P1/2(60)** (4.2×10^{-4} S cm^{-1}). By integrating the response current, the accumulated charge in the interface between electrolyte and electrodes can be

calculated (Figure 3-5b). The transferred current curve of **P1/2(40)** was flat, and the value is low, indicating the initial charging/discharging response was weak and the lack of accumulated charges which can also be attributed to low ionic conductivities. The charge of **P1/2(60)** was 6.8 mC which was about two times larger than that of **P1/2(50)**. The fact that more charging sample did not generate larger bending strain was assumably owing to the limitation of deformation by inherent rigidity of polymers.

Since **P1/2(X)** actuators showed weak force (will be discussed in section 3.3.3), the block force affected by **IL** content was examined by **P1/3(x)** actuators. As shown in Figure 3-6, the **P1/3(60)** actuator exhibited maximum blocking force of 1.2 mN around 2 min after applying a DC voltage of 2 V. The **P1/3(50)** actuators generated a force of 0.6 mN and took 5 min to reach equilibrium state. The larger blocking force generated by **P1/3(x)** with higher **IL** amount is caused by the larger bending displacement according to the following equation:[24]

$$P = \frac{3\delta EI}{L^3}$$

where P is applied force, δ is bending displacement, E, I, and L are elasticity, momentum, and length of actuator, respectively.

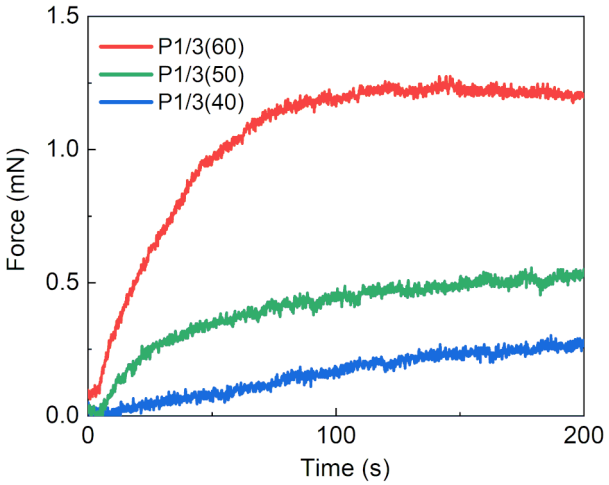

Figure 3-6. Generated force of **P1/3(x)** under a DC of 2 V at ambient condition.

3.3.3 Ion species

The bending of actuator caused by the difference in deformation at two electrode–electrolyte interfaces strongly depend on the size of cation and anion. In this study, we investigated two

types of cations: protonated imidazole (**Imi**$^+$) and 1-butyl-3-methylimidazolium (**BMIM**$^+$), and two types of anions: bis(trifluoromethylsulfonyl)imide (**TFSI**$^-$), and hydrogen sulfate (**HSO$_4^-$**). The ion volume is listed in Table 3-1.

Table 3-1. Ion volume of cations and anions in this study.

*Ion type	Ion volume (Å^3)
[**Imi**]$^+$	95[a]
[**BMIM**]$^+$	224[b]
[**TFSI**]$^-$	147[c]
[**HSO$_4$**]$^-$	28[d]

[a]The volume of protonated imidazole was calculated from Van der Waals volumes of imidazole and H.[25] The Van der Waals volumes of imidazole was reported to be 90 Å^3.[26] The value of imidazole volume in per mole was calculated to be 54.18 cm^3/mol. The volumes of -H was 3.44 cm^3/mol.[27] The volumes of imidazolium cation (imidazole attached with H) were 57.62 cm^3/mol. The Van der Waals volumes of imidazolium cation was calculated to be 95 Å. [b]Ref.[28]; [c]Ref.[29]; [d]Ref.[30].

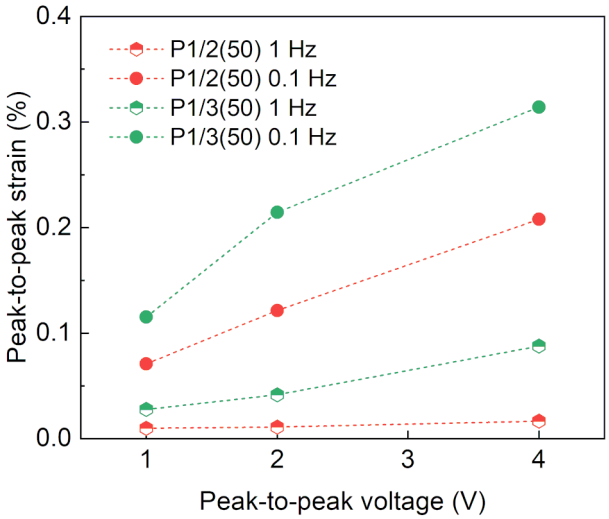

Figure 3-7. Strain comparison of **P1/2(50)** and **P1/3(50)** actuators under various applied voltage in 50% RH environment.

Here, the performance of columnar **LC**-based actuators employing two types of ionic liquids: **[Imi]$^+$[TFSI]$^-$** (**P1/2(x)**) and **[BMIM]$^+$[HSO$_4$]$^-$** (**P1/3(x)**) in same mole fraction was compared. The bending strain of **P1/2(50)** and **P1/3(50)** actuators under various applied voltage and frequency was shown in Figure 3-7. The value of **P1/3(50)** was higher than that of **P1/2(50)** at

any condition. There are 2–5 times difference of strain at 1 Hz and around 1.5 times difference at 0.1 Hz. For example, **P1/3(50)** generated a strain of 0.31% under ±2 V at 0.1 Hz while the value of **P1/2(50)** was 0.20%. The volume differences of cations and anions for **P1/2(50)** and **P1/3(50)** are 52 $Å^3$ and 196 $Å^3$. The bigger difference was leading to the larger generated strain. The strain is not proportional to the volume difference is due to the ion distribution in the electrolyte.[31] For different types of **IL**s, the accumulation of cations and anions on the interface of cathode and anode are in different gradient in depth direction. It will result in the total volume deformation is not exactly matched with the difference in volume of cations and anions.

From the transferred current of **P1/2(50)** and **P1/3(50)** actuator (Figure 3-8a), the initial response of **P1/3(50)** actuator was much more than that of **P1/2(50)** actuator, it determines the response speed when an electric filed was changed. When electric field was changed from E_+ to $E_–$, the **P1/3(50)** actuator bending to the initial position with 1 s (motion speed: 0.78 mm s^{-1}), while **P1/2(50)** actuator bending with a speed of 0.21 mm s^{-1} (Figure 3-8b). The $\mathbf{HSO_4^-}$ with small molecular size can easily move inside transporting channels with low hindrance that making the **P1/3(50)** actuator can bend in faster speed. And the dissociation of ion paring between cations and anions of **2** with zwitterionic moiety in **P1/2(50)** also delayed the ion movement when changing electric field.

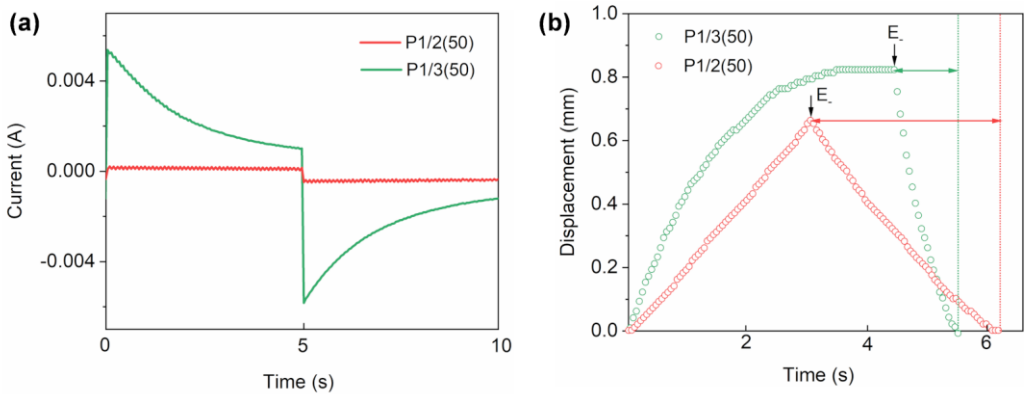

Figure 3-8. Comparison of **P1/2(50)** and **P1/3(50)** actuators under an AC voltage of ±2 V with a frequency of 0.1 Hz in 50% RH environment: (a) Current; (b) Displacement.

The **P1/3(50)** actuator exhibited high generated force than **P1/2(50)** actuator at ambient environment (Figure 3-9). And **P1/3(50)** actuator triggered by a DC voltage of 1V generated a force of 0.5 mN, while the **P1/2(50)** actuator only generated 0.2 mN even under a DC voltage of 2V. Furthermore, the **P1/3(50)** actuator can reach equilibrium position by taking 5 min while

the **P1/2(50)** actuator cannot reach equilibrium position until 10 min. Larger blocking force for **P1/3(50)** can be attributed to the larger deformation according to the equation shown in section **3.3.2**. Furthermore, the containing of water in **P1/2(50)** can lead to lower stiffness, which was also reduced the force output.

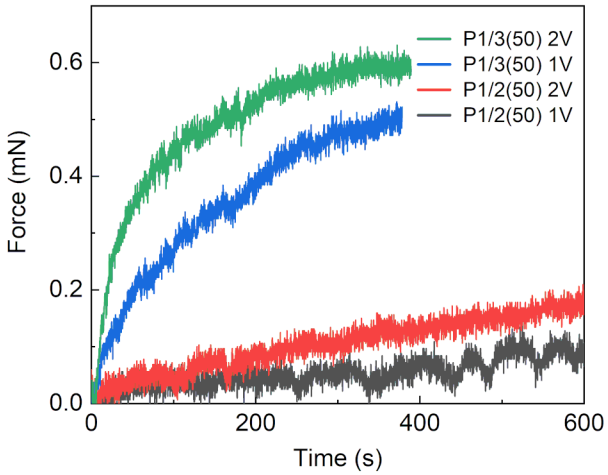

Figure 3-9. Force generation of **P1/2(50)** and **P1/3(50)** actuators under a DC voltage in ambient environment.

3.3.4 Thickness

To investigate the thickness influenced actuation performance, **P1/3(50)** actuators with thickness of 53 μm, 74 μm, and 133 μm were tested. The strain value of **P1/3(50)-133** actuator was 0.22% under an AC voltage of ±2 V, which was half of the value of **P1/3(50)-53** (0.51%) (Figure 3-10a). The thicker actuator exhibited smaller bending strain because of the limitation caused by the stacked and entangled polymer chains. In contrary, the thicker actuator **P1/3(50)-133** can generate larger blocking force (1mN under a DC of 2 V) than **P1/3(50)-74** (0.6 mN) and **P1/3(50)-53** (0.35 mN) due to its rigid structure. The relationship between stiffness and thickness is shown in the following equation:[32]

$$EI = \frac{wt^3}{12}$$

where *EI* is stiffness, *w* and *t* are the width and thickness of actuator strip.

It should be noted that **P1/3(50)-53** actuators have a back relaxation when voltage was applying after 1 min due to the generated stress disrupted thin fragile electrolyte films and lead **P1/3(50)-53** actuators to loss the mechanical properties.

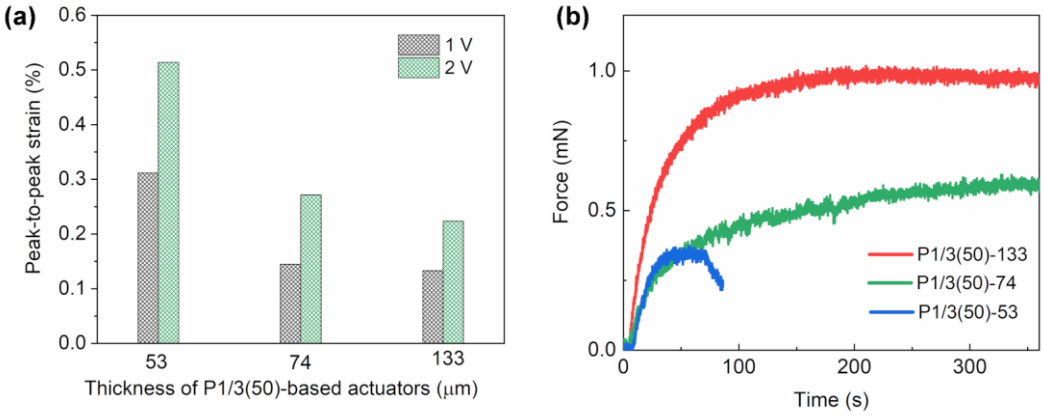

Figure 3-10. P1/3(50) actuators with various thickness (53 μm, 74 μm, and 133 μm): (a) Peak-to-peak strain under peak-to-peak voltages of ±0.5, ±1 V with a frequency of 0.01 Hz; (b) generated force under a DC of 2 V at ambient environment.

3.4 Conclusions

A new design of ionic electroactive polymer actuators with 1D nanostructured ionic transporting channels was achieved in this chapter. The actuators were allowed to work in both dry and humid condition by employing ionic polymers containing columnar **LC** architecture. A high bending strain of 0.65% for [**BMIM**]$^+$[**HSO4**]$^-$-based (**P1/3(50)**) actuator was generated under an AC of ±2V with a frequency of 0.01 Hz in dry state. The bending performance was enhanced by increasing the humidity and reached to maximum value at 70% RH. A high strain of 0.84% for **[Imi]**$^+$**[TFSI]**$^-$-based actuator (**P1/2(50)**) was exhibited under an AC of ±2 V with a frequency of 0.1 Hz in 70% RH environment. The actuation performance was certificated to be affected by ion content in the electrolyte. The actuator with 60 mol% of **IL** shows higher bending strain comparing to the sample with 40 mol% of **IL**. And the actuator with higher ion content can generate higher block force within shorter equilibrium time. The generated force of dry actuators with 60 mol% of **IL** can reach to 1.2 mN within 2 min under a DC of 2 V in ambient atmosphere. Ion species can be contributed to affect the actuation performance, too. The larger difference in volume size of cations and anions can generate larger deformation. Furthermore, the thickness effect was also discussed in this section. Thicker electrolyte

exhibited larger blocking force but smaller bending displacement. Controlling of ions and thickness can be a powerful approach to optimize actuator performance. Due to its compliance of both dry and humid environment, the actuators composed of ionic **LC** polymer electrolyte and conductive polymer electrodes have a wide application field such as small robotics, artificial skins, biomedicals and so on. The introduction of **LC** nanostructures can provide a new strategy for designing soft ionic polymer actuators to achieve fast, large deformation.

3.5 References

1. Chen, Y.; Zhao, H.; Mao, J.; Chirarattananon, P.; Helbling, E. F.; Hyun, N.-s. P.; Clarke, D. R.; Wood, R. J., Controlled Flight of a Microrobot Powered by Soft Artificial Muscles. *Nature* **2019,** *575* (7782), 324–329.

2. Kanik, M.; Orguc, S.; Varnavides, G.; Kim, J.; Benavides, T.; Gonzalez, D.; Akintilo, T.; Tasan, C. C.; Chandrakasan, A. P.; Fink, Y.; Anikeeva, P., Strain-Programmable Fiber-Based Artificial Muscle. *Science* **2019,** *365* (6449), 145.

3. Chen, D.; Pei, Q., Electronic Muscles and Skins: a Review of Soft Sensors and Actuators. *Chem. Rev.* **2017,** *117* (17), 11239–11268.

4. Ilami, M.; Bagheri, H.; Ahmed, R.; Skowronek, E. O.; Marvi, H., Materials, Actuators, and Sensors for Soft Bioinspired Robots. *Adv. Mater.* **2021,** *33* (19), 2003139.

5. Hines, L.; Petersen, K.; Lum, G. Z.; Sitti, M., Soft Actuators for Small-Scale Robotics. *Adv. Mater.* **2017,** *29* (13).

6. Bai, H.; Li, S.; Shepherd, R. F., Elastomeric Haptic Devices for Virtual and Augmented Reality. *Adv. Funct. Mater.* **2021,** *2009364* (n/a), 2009364.

7. Zhai, Y.; Wang, Z.; Kwon, K.-S.; Cai, S.; Lipomi, D. J.; Ng, T. N., Printing Multi-Material Organic Haptic Actuators. *Adv. Mater.* **2021,** *33* (19), 2002541.

8. Kruusamäe, K.; Punning, A.; Aabloo, A.; Asaka, K., Self-Sensing Ionic Polymer Actuators: A Review. *Actuators* **2015,** *4* (1), 17–38.

9. Kim, O.; Kim, H.; Choi, U. H.; Park, M. J., One-Volt-Driven Superfast Polymer Actuators Based on Single-Ion Conductors. *Nat. Commun.* **2016,** *7*, 13576.

10. Mukai, K.; Asaka, K.; Sugino, T.; Kiyohara, K.; Takeuchi, I.; Terasawa, N.; Futaba, D. N.; Hata, K.; Fukushima, T.; Aida, T., Highly Conductive Sheets from Millimeter-Long Single-Walled Carbon Nanotubes and Ionic Liquids: Application to Fast-Moving, Low-Voltage Electromechanical Actuators Operable in Air. *Adv. Mater.* **2009,** *21* (16), 1582–1585.

11. Terasawa, N., High-Performance Transparent Actuator Made from Poly(dimethylsiloxane)/Ionic Liquid Gel. *Sens. Actuators, B* **2018,** *257*, 815–819.

12. Wang, F.; Jeon, J.-H.; Park, S.; Kee, C.-D.; Kim, S.-J.; Oh, I.-K., A Soft Biomolecule Actuator Based on a Highly Functionalized Bacterial Cellulose Nano-Fiber Network with Carboxylic Acid Groups. *Soft Matter* **2016,** *12* (1), 246–254.

13. Correia, D. M.; Lizundia, E.; Fernandes, L. C.; Costa, C. M.; Lanceros-Méndez, S., Influence of Cellulose Nanocrystal Surface Functionalization on the Bending Response of Cellulose Nanocrystal/ionic Liquid Soft Actuators. *PCCP* **2021,** *23* (11), 6710–6716.

14. Terasawa, N., Self-Standing High-Performance Transparent Actuator Based on Poly(dimethylsiloxane)/TEMPO-Oxidized Cellulose Nanofibers/Ionic Liquid Gel. *Langmuir* **2020,** *36* (22), 6154–6159.

15. Kato, T.; Yoshio, M.; Ichikawa, T.; Soberats, B.; Ohno, H.; Funahashi, M., Transport of Ions and Electrons in Nanostructured Liquid Crystals. *Nat. Rev. Mater.* **2017,** *2* (4).

16. Goossens, K.; Lava, K.; Bielawski, C. W.; Binnemans, K., Ionic Liquid Crystals: Versatile Materials. *Chem. Rev.* **2016,** *116* (8), 4643–4807.

17. Seki, A.; Yoshio, M., Multi-Color Photoluminescence Based on Mechanically and Thermally Induced Liquid-Crystalline Phase Transitions of a Hydrogen-Bonded Benzodithiophene Derivative. *Chemphyschem* **2020,** *21* (4), 328–334.

18. Wang, C.; Cao, S.; Li, P.; Tan, S.; Wu, Y., Anisotropic Films Photopolymerized from Aligned Cross-Linkable Gemini Ammonium Liquid Crystals for Ion Conduction. *J. Appl. Polym. Sci.* **2019,** *136* (15), 47349.

19. Yamashita, A.; Yoshio, M.; Shimizu, S.; Ichikawa, T.; Ohno, H.; Kato, T., Columnar Nanostructured Polymer Films Containing Ionic Liquids in Supramolecular One-Dimensional-Nanochannels. *J. Polym. Sci., Part A: Polym. Chem.* **2015,** *53* (2), 366–371.

20. Ichikawa, T.; Sasaki, Y.; Kobayashi, T.; Oshiro, H.; Ono, A.; Ohno, H., Design of Ionic Liquid Crystals Forming Normal-Type Bicontinuous Cubic Phases with a 3D Continuous Ion Conductive Pathway. *Crystals* **2019,** *9* (6), 309.

21. Soberats, B.; Yoshio, M.; Ichikawa, T.; Zeng, X.; Ohno, H.; Ungar, G.; Kato, T., Ionic Switch Induced by a Rectangular–Hexagonal Phase Transition in Benzenammonium Columnar Liquid Crystals. *J. Am. Chem. Soc.* **2015,** *137* (41), 13212–13215.

22. Luo, J.; You, J.; Tan, S.; Wang, C.; Wu, Y., Lamellar Lyotropic Liquid Crystal Superior to Micellar Solution for Proton Conduction in an Aqueous Solution of 1-Tetradecyl-3-methylimidazolium Hydrogen Sulfate. *ACS Appl Mater Interfaces* **2020,** *12* (40), 45611–45617.

23. Yang, J.; Tan, S.; Xie, W.; Luo, J.; Wang, C.; Wu, Y., Promotion of Anhydrous Proton Conduction

by Polyvinyl Alcohol in Liquid Crystalline Composite Membranes Containing 1-Tetradecyl-3-methylimidazolium Hydrogen Sulfate. *Ionics* **2020,** *26* (4), 1819–1827.

24. Kim, J.; Kang, Y.; Yun, S., Blocked Force Measurement of Electro-Active Paper Actuator by Micro-Balance. *Sens. Actuators, A* **2007,** *133* (2), 401–406.

25. Li, P.; Paul, D. R.; Chung, T.-S., High Performance Membranes Based on Ionic Liquid Polymers for CO_2 Separation from the Flue Gas. *Green Chem.* **2012,** *14* (4), 1052–1063.

26. Costantino, U.; Massucci, M. A.; La Ginestra, A.; Tarola, A. M.; Zampa, L., Intercalation of Heterocyclic Compounds in α-Zirconium Phosphate: Imidazole, Benzimidazole, Histamine and Histidine. *J. Inclusion Phenom.* **1986,** *4* (2), 147–162.

27. Bondi, A., van der Waals Volumes and Radii. *J. Phys. Chem.* **1964,** *68* (3), 441–451.

28. Liu, S.; Liu, W.; Liu, Y.; Lin, J.-H.; Zhou, X.; Janik, M. J.; Colby, R. H.; Zhang, Q., Influence of Imidazolium-Based Ionic Liquids on the Performance of Ionic Polymer Conductor Network Composite Actuators. *Polym. Int.* **2010,** *59* (3), 321–328.

29. Ue, M.; Murakami, A.; Nakamura, S., A Convenient Method to Estimate Ion Size for Electrolyte Materials Design. *J. Electrochem. Soc.* **2002,** *149* (10), A1385.

30. Marcus, Y.; Donald Brooke Jenkins, H.; Glasser, L., Ion Volumes: a Comparison. *J. Chem. Soc., Dalton Trans.* **2002,** (20), 3795–3798.

31. Liu, Y.; Lu, C.; Twigg, S.; Ghaffari, M.; Lin, J.; Winograd, N.; Zhang, Q. M., Direct Observation of Ion Distributions near Electrodes in Ionic Polymer Actuators Containing Ionic Liquids. *Sci. Rep.* **2013,** *3* (1), 973.

32. Oh, C.; Kim, S.; Kim, H.; Park, G.; Kim, J.; Ryu, J.; Li, P.; Lee, S.; No, K.; Hong, S., Effects of Membrane Thickness on the Performance of Ionic Polymer–Metal Composite Actuators. *RSC Adv.* **2019,** *9* (26), 14621–14626.

Chapter 4 Electroactive Actuators Based on Columnar Ionic Liquid Crystal/Polymer Composite Membrane Electrolytes Forming 3D Continuous Ionic Channels

4.1 Introduction

Soft polymer actuators have attracted intensive attention for their applications in soft robotics, bionics, and haptics.[1-7] A variety of polymers, such as dielectric elastomers, liquid crystal elastomers, and electron- and ion-conductive polymers have been studied as actuator materials. Among them, ionic liquid-containing polymers have gained increasing attention in the development of ionic electromechanical actuators due to their non-volatility and large bending deformation under low operation voltage.[8-13] The simple configuration of the ionic actuator consists of the ionic polymeric layer sandwiched between two flexible electrodes to obtain a deformable electrostatic capacitor. The efficient and rapid actuation depends on the coupling of effective ionic tranport with elastic properties. Control of intermolecular interactions and formation of phase-separated nanostructures are significantly important in the design of polymer electrolytes to achieve fast ion transport and mechanical intensification.

Several bottom-up approaches have been explored to generate interconnected ion transport channels and reinforce polymer materials, such as self-assembly of block copolymers[14-17] and charged condensation polymers,[18-24] geometric engineering in polymer blends,[25] addition of inorganic additives to polymers,[26] and chemically modified electrolyte/electrode interfaces.[27] In particular, incorporation of ionic liquids into block copolymers has the benefit of tuning the morphology of polymers as well as increasing the conductivity. The formation of continuous ionic domains in block polymers resulted in an increase of the electromechanical performance. However, this approach suffered from the formidable synthetic and alignment procedures. Increasing the conducitivity at room-temperature remains a challenge to improve the actuation performance. The new design strategy for ionic polymer electrolytes here is to construct three-dimensionally interconnected ionic nanochannels in such materials through the self-assembly of ionic liquid crystals and conventional vinyl polymers.

The use of liquid crystal self-assembly is a powerful approach for the preparation of

nanostructured soft materials exhibiting low-dimensional transport of ions.[28-34] Previously, enhanced ion transport for nanostructured ionic liquid crystals and ordered ionic liquids into hydrogen-bonded liquid crystal networks was reported, wherein ions can form 1–3D nanochannels shielded by insulating mesogenic moieties.[35-36] These materials have great potential as electrolytes in energy devices such as lithium-ion batteries, fuel cells, and dye-sensitized solar cells.[37-40] However, current anisotropic liquid-crystalline electrolytes provide limited efficiency due to the inhibition of ion migration at the multi-domain grain boundaries, although many efforts have been conducted to achieve macroscopically oriented monodomains such as surface treatments and magnetic fields.[41] More recently, some groups have focused on bicontinuous cubic liquid-crystalline electrolytes due to their intrinsic 3D channel connectivity.[36, 42-43] However, it is difficult to design room-temperature bicontinuous cubic materials.

Considering previous researches, the author envisioned that the use of a continuous ionic matrix forming the outside of supramolecular columnar architectures[44] would be another approach to develop an efficient electrolyte. To date, a diverse range of liquid-crystalline polymer actuators that use anisotropic structures and respond to external stimuli such as heat, light, electric field, and humidity have been developed.[45-48] However, to the best of our knowledge, ionic electroactive polymer actuators based on 3D columnar ionic liquid-crystalline electrolytes have not yet been explored. The goal of this work is the design of a new type of nanostructured liquid-crystalline polymer electrolytes with good room-temperature ionic conductivity in three dimensions, as an alternative to known anisotropic ionic liquid-crystalline materials. In addition, the intension here is also to show that such a material could be implemented as an electrolyte in an electromechanical polymer actuator to demonstrate a new application direction for ionic liquid-crystalline materials.

Normally, fan-shaped zwitterionic molecules tend to form columnar structure with 1D channels as shown in chapter 2. In this chapter, a new rod-shaped zwitterionic liquid-crystalline compound (**ZI**) was designed. It was expected that by interaction of zwitterionic part with ionic liquids(**IL**) can change molecular shape from rod-like to conical which can induce inverted columnar structure with 3D channels. The 3D columnar ionic liquid crystal/polymer composite membrane electrolyte was obtained via the supramolecular self-assembly of **ZI**, **IL**, and poly(vinyl alcohol) (**PVA**) (**Figure 4-1**). The net 3D-continuous ionic polymer membrane

shows enhanced ionic conductivity by the incorporation of water molecules under controlled relative humidity (RH) and form a stable contact with conducting polymer electrodes of poly(3,4-ethylenedioxythiophene) doped with poly(styrene sulfonate) (**PEDOT:PSS**), which leads to the low-voltage-driven, fast-response actuation.

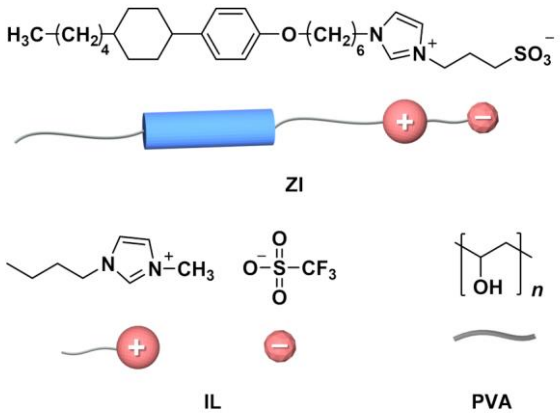

Figure 4-1. Chemical structures and illustrations of the zwitterionic liquid-crystalline compound (**ZI**), ionic liquid (**IL**), and poly(vinyl alcohol) (**PVA**).

4.2 Experimental section

Synthesis and characterization

All reagents and solvents were purchased from Aldrich, TCI or Wako, and used as received without further purification. NMR spectra were recorded using a JEOL JNM-ECS400 at 400 MHz and 100 MHz for ^{1}H NMR and ^{13}C NMR in $CDCl_3$, respectively. Chemical shifts of ^{1}H and ^{13}C NMR signals were quoted in ppm to internal standard Me_4Si (δ = 0.00) and $CDCl_3$ (δ = 77.00). Elemental analysis for CHNS was carried out by using an ELEMENTAR vario EL tube.

Chapter 4

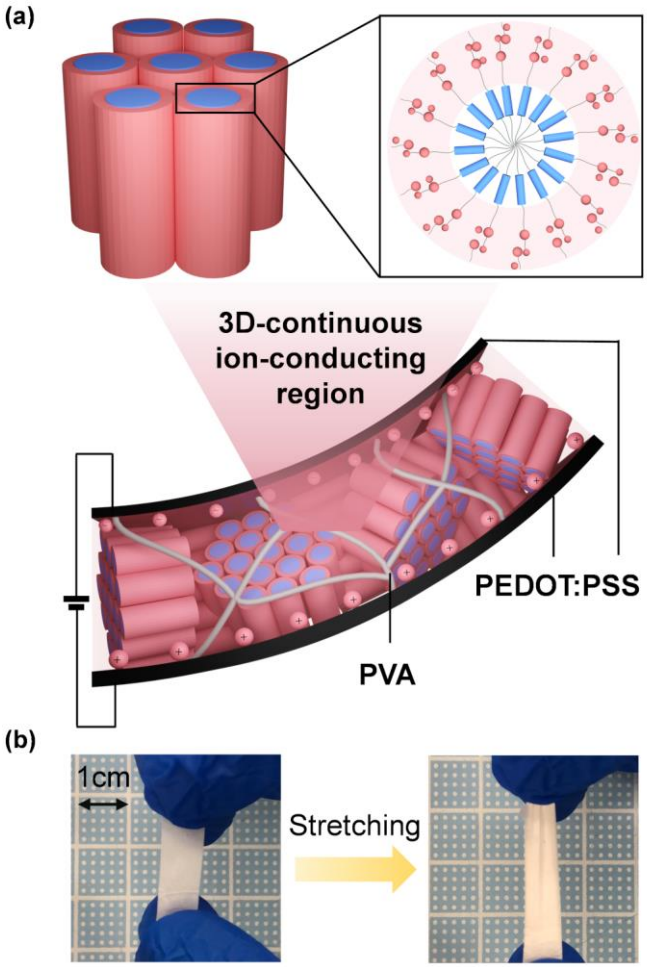

Figure 4-2. (a) Schematic illustration of the deformed ionic electroactive polymer actuator composed of the hexagonal columnar liquid-crystalline polymer composite electrolyte membrane of **ZI/IL/PVA** sandwiched between two **PEDOT:PSS** electrode layers under an applied DC electric field at 70% RH. (b) Photographs of the free-standing **ZI/IL/PVA** membranes before and after mechanical stretching.

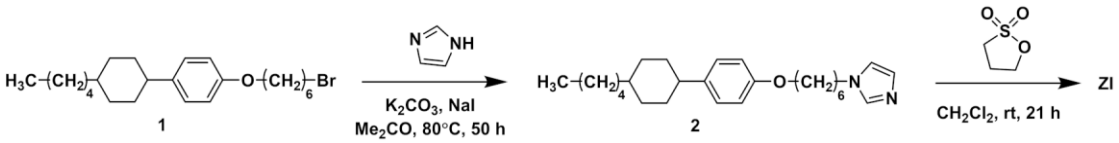

Scheme 4-1. Synthesis of compound **ZI**.

6-4-(*trans*-4-Pentylcyclohexyl)phenyloxy-1-bromohexane **1** was synthesized according to the reported procedure.[49]

Chapter 4

1-[6-{4-(*trans*-4-Pentylcyclohexyl)phenyloxy}]hexyl-1*H*-imidazole (2)

Compound **1** (8.94 g, 21.8 mmol), imidazole (7.43 g, 109.1 mmol), potassium carbonate (15.20 g, 109.9 mmol), and sodium iodide (3.30 g, 22.0 mmol) were added in a three-necked round-bottom flask with a reflux condenser. After removal of air and refilled with an Ar gas in flask, acetone (140 mL) was added. The suspension was stirred and refluxed at 80 °C for 50 h. After the reaction mixture was cooled, the inorganic solids were dissolved in water and the organic mixture was extracted with EtOAc and washed by a sat. NH_4Cl aq. solution. The organic phase was dried over anhydrous $MgSO_4$ and filtered. After removal of the solvent under vacuum, the residue was purified by a silica-gel flash column chromatography (MeOH: $CHCl_3$ = 0:10 to 1:9) to give a white solid **2** (5.47 g, 13.8 mmol, 63 %).

^{1}H NMR (400 MHz, $CDCl_3$): δ = 7.46 (s, 1H; CH), 7.11 (d, J = 8.7 Hz, 2H; ArH), 7.05 (t, J = 1.2 Hz, 1H; CH), 6.90 (t, J = 1.4 Hz, 1H; CH), 6.80 (d, J = 8.2 Hz, 2H; ArH), 3.92 (q, J = 7.0 Hz, 4H; CH_2), 2.44 (tt, J = 12.1, 3.1 Hz, 1H; CH), 1.99-1.72 (m, 8H; CH_2), 1.53-1.18 (m, 15H; CH, CH_2), 1.07-0.98 (m, 2H; CH_2), 0.89 (t, J = 7.1 Hz, 3H; CH_3); ^{13}C NMR (100 MHz, $CDCl_3$): δ = 157.17, 140.23, 137.20, 129.59, 127.75, 118.87, 114.30, 77.48, 76.85, 67.64, 47.04, 43.85, 37.53, 37.43, 34.71, 33.78, 32.35, 31.18, 29.25, 26.80, 26.44, 25.77, 22.85, 14.27; Elemental analysis calcd. for $C_{26}H_{40}N_2O$: C, 78.74, H, 10.17, N, 7.06; found: C, 79.20, H, 9.86, N, 6.97.

3-[1-[6-{4-(*trans*-4-Pentylcyclohexyl)phenyloxy}hexylimidazolium]propane-1-sulfonate (ZI)

To a 15 mL anhydrous dichloromethane solution of compound **2** (5.37 g, 13.5 mmol), 1,3-propanesultone was added dropwise. After stirring at room temperature for 21 h, the resulting mixture was purified by a silica-gel flash column chromatography (MeOH: $CHCl_3$ = 1:9 to 2:8) and subsequent recrystallization from EtOAc to afford compound **ZI** as a white powder (4.37 g, 8.4 mmol, 61%).

^{1}H NMR (400 MHz, $CDCl_3$): δ = 9.66 (s, 1H; CH), 7.36 (t, J = 1.6 Hz, 1H; CH), 7.15 (t, J = 1.6 Hz, 1H; CH), 7.09 (d, J = 8.7 Hz, 2H; ArH), 6.78 (d, J = 8.7 Hz, 2H; ArH), 4.53 (t, J = 6.9 Hz, 2H; CH_2), 4.26 (t, J = 7.6 Hz, 2H; CH_2), 3.90 (t, J = 6.2 Hz, 2H; CH_2), 2.84 (t, J = 6.9 Hz, 2H; CH_2), 2.38 (q, J = 7.2 Hz, 2H; CH_2), 1.91-1.71 (m, 8H; CH_2), 1.54-1.17 (m, 15H; CH, CH_2), 1.05-0.97 (m, 2H), 0.88 (t, J = 6.9 Hz, 3H; CH_3); ^{13}C NMR (100 MHz, $CDCl_3$): δ = 157.14, 140.20, 137.71, 127.75, 122.86, 121.59, 114.30, 77.48, 76.85, 67.60, 50.00, 48.67, 47.56, 43.81,

37.51, 37.40, 34.70, 33.74, 32.34, 30.25, 29.14, 26.78, 26.06, 25.03, 22.84, 14.25; Elemental analysis calcd. for $C_{29}H_{46}N_2O_4S$: C, 67.14, H, 8.94, N, 5.40, S, 6.18; found: C, 67.10, H, 8.89, N, 5.25, S, 6.37.

Preparation of the equimolar mixture of ZI and IL (ZI/IL)

The solid sample of **ZI** and 1-butyl-3-methylimidazolium trifluoromethanesulfonate (**IL**) were mixed in a 1:1 molar ratio and dissolved in methanol. The solvent was slowly evaporated at 60 °C and the resultant mixture was dried in a vacuum oven at 75 °C for 1 day.

Preparation of ZI/IL/PVA composite membranes

The solid **ZI** and **IL** were dissolved in deionized water in the 1:1 molar ratio with a concentration of 20 wt%. The resulting solution was stirred at 50 °C for 30 min. The 10 wt% aqueous solution of **PVA** (TCI, degree of polymerization: approximately 2000, degree of saponification: ca. 80 mol%) was added into **ZI/IL** solution to be the ratio of **ZI/IL**: **PVA** = 77.0 : 23.0 in wt% and stirred at 50 °C for 2 h. The resulting solution was allowed to stand until the bubbles disappeared, and then it was casted onto a polyimide tape-coated glass substrate and dried at 50 °C in an oven for 2 h and then dried in vacuum at 80 °C for 1 day.

Preparation of ZI/IL/PVA-based actuators

The **ZI/IL/PVA** composite membranes and **PEDOT: PSS** films were stored in a humidity-controlled chamber (Espec Co., Bench-top type temperature & humidity chamber SH-242) for 2 h to reach a moisture-equilibrium state before use. Then the humidified membrane was sandwiched between two humidified **PEDOT: PSS** films by pressing at room temperature (AS ONE Co., Small hot press machine H300-10D). The dimension of actuators in this work was 25 mm in length, 5 mm in width and 50 μm in thickness.

Actuator performance test

The actuator strip with a copper foil on one end was clamped between two stainless steel electrodes connected to a potentiostat (Hokudo Denko, HAL3001A). Alternating square-wave voltages generated by a function generator (NF, WF1973) were controlled by the potentiostat

and applied to the actuator strip. The working actuator length was 20 mm. The bending displacement was measured by using a laser meter (Keyence, LK-HD500). The laser was irradiated perpendicular to the surface of actuator at 7 mm away from the tip of strip. The signals of voltage, current, and displacement were recorded in a MEMORY HiLOGGER (HIOKI LR8431) with a time interval of 50 ms. The measurements were performed in a humidity-controlled glove box. Because the displacement at ±2 V under 0.1 Hz is over the working distance of a laser displacement sensor, the peak-to-peak displacement in Fig. 6a is estimated from the photograph of bending actuators.

Characterization of liquid crystallinity

Optical textures of liquid-crystalline phases were observed by using a polarized optical microscope (POM) (Olympus, BX51N-31P-O3) equipped with a digital camera DP22 and a temperature control system (LINKAM T95-HS, LTS420E). X-ray diffraction (XRD) measurements were carried out by Rigaku Miniflex 600 (Ni-filtered Cu Kα) diffractometer equipped with an Anton Par BTS 500 hot stage chamber sealed by a polyimide tape. The relative humidity inside the XRD chamber was controlled by precise steam condense system (Micro equipment Inc.) equipped with humidity/temperature transmitter (Elektronik, EE23 T6). Differential scanning calorimetry (DSC) measurements were conducted with a NETZCH DSC 3500 Sirius system at a scanning rate of 10 °C/min. Attenuated total reflectance Fourier-transform infrared (ATR-FTIR) spectra were taken with a BRUKER FT-IR ALPHA II spectrometer with a single reflection diamond ATR module.

Electrochemical measurements

Impedance measurement was performed using a Metrohm Autolab PGSTAT128N analyzer (frequency range: 100 Hz–10 MHz, applied voltage: 10 mV). The impedance data were fitted by the equivalent circuit consisting of a constant phase element and a parallel RC element. A glassy cell with comb-shaped gold electrodes deposited with the gap of 300 μm and a cover glass was used for the anisotropic measurements of in-plane conductivities for the aligned columnar phase of **ZI/IL** samples. The ionic conductivities were calculated to be the product of $1/R$ (Ω^{-1}) times the cell constant (cm^{-1}) for comb-shaped gold electrodes with a polyimide tape spacer, which was calibrated with a KCl aqueous solution (Hanna Instruments, HI7033L

84 μS cm^{-1}). The value of the bulk resistance *R* was obtained from the intercept of the semicircle on the real axis of impedance in Nyquist plots. The planar alignment of the columnar phase was achieved by applying a mechanical shearing force to the sample filled between the gold gaps. As for the conductivity measurement of **ZI/IL/PVA** membranes, a four-probe sample holder (TOYO Co., SH2-Z) was used, and the membrane was sandwiched between the gold electrodes (bottom electrode: 2.5 mm ø, top electrode: 25 mm ø). The ionic conductivity was calculated by the equation: $\sigma = d/(R \cdot S)$, where σ is the conductivity (S cm^{-1}), *d* is the sample thickness (cm), and *S* is the sample area (cm^2).

The cyclic voltammograms of actuators were measured by using a Swagelok-type two-electrode cell (2E-Cell-SUS, Eager Corporation) and a CH instruments electrochemical analyzer (Model: 611E). The specific capacitance was calculated by using the following equation:[50]

$$C = \int \frac{IdV}{2\nu SV}$$

where *C* (F cm^{-2}) is the specific capacitance, *I* (A) is response current of CV, *V* (V) is voltage windows, *v* (V s^{-1}) is scan rate, *S* (cm^2) is the area of electrode of active materials.

SEM observation of the actuators

The scanning electron microscope observation of the actuators was performed using a Hitachi S-4800 FE-SEM operating at 10 kV.

Tensile test of the ZI/IL/PVA membrane

The stress-strain behavior of the electrolyte films was measured by a mechanical testing machine (Shimadzu EZ-SX). The electrolyte film was stretched with a speed of 5 mm per minute. The Young's modulus was estimated using the slope of the linear part of the stress-strain curve.

Energy conversion efficiency calculation

The average input electric power ($P_{electrical}$) for AC square-wave electric field was calculated by integrating charging current:

$$P_{electrical} = \frac{1}{T}\int_0^T v(t)i(t)\,dt$$

where *T* is the time for one cycle, *v(t)* and *i(t)* are function of applied voltage and response current, in square-wave electric field *v(t)* is constant value.

The output mechanical power ($P_{mechanical}$) is calculated by the following equation:[51]

$$P_{mechanical} = 0.5Y\varepsilon^2 f \times Vol$$

where *Y* is Young's modulus, ε is the bending strain, *f* is the frequency of applied electric field, *Vol* is the volume of actuator,

The energy conversion efficiency (η) from electrical to mechanical of **LC** composite membranes is defined as the following equation:

$$\eta = \frac{P_{mechanical}}{P_{electrical}}$$

4.3 Results and discussion

4.3.1 LC Properties and ionic conductivities of ZI/IL

Zwitterionic compounds are known to function as prominent ion-conducting matrices.[52] With an aim to construct self-assembled zwitterionic channels, a rod-shaped mesogenic compound, **ZI**, containing an imidazolium sulfobetaine moiety was designed (Figure 4-1). The complexation of **ZI** and **IL** was expected to facilitate ion transport in ordered ion channels after dissociation of ionic liquids.[53-54] Furthermore, the author envisioned that the combination of polar polymers with ionic liquid crystals would result in new, free-standing, liquid crystal/polymer composite electrolytes with tunable mechanical and electrical properties.

Compound **ZI** shows a crystalline (Cr)—smectic A (S_A) phase transition at 114 °C during first heating process. No isotropization of the S_A phase was detected by the DSC measurement. The decomposition of **ZI** was observed by POM around 230 °C. On the DSC first cooling and second heating process, the glass transition was detected at 13 °C and 17 °C, respectively. The XRD pattern of **ZI** at 140 °C shows three peaks of 46.4 Å, 23.3 Å, and 15.6 Å, which can be assigned to the (100), (200) and (300) diffraction of the layered molecular assemblies, respectively. The extended molecular length of **ZI** was estimated to be 28 Å using the DTF

calculations of the Wavefunction Spartan 18. It is assumed that **ZI** forms the interdigitated bilayer structure in the S_A phase.

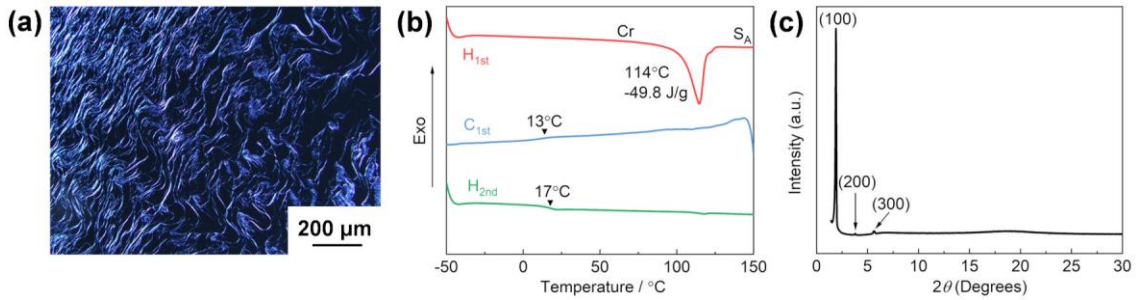

Figure 4-3. Liquid-crystalline properties of **ZI**: (a) POM image at 140 °C; (b) DSC traces on cooling and heating process; (c) XRD pattern at 140 °C.

The mixture of **ZI** and **IL** as a lyotropic solvent in a 1:1 molar ratio (**ZI/IL**) exhibited a type I hexagonal columnar (Col_{hex}) liquid-crystalline phase, whereas **ZI** alone showed a thermotropic smectic A phase (Figure 4-3). For dry **ZI/IL** (25% RH) and the humidified samples (60–70% RH), the fan-shaped and broken fan-shaped optical textures of columnar phases were observed at room temperature under crossed polarizers (Figure 4-4). The XRD patterns of **ZI/IL** at various RH values show two peaks in the small-angle region with a reciprocal *d*-spacing ratio of 1 : √3, corresponding to the (10) and (11) reflections of a Col_{hex} mesophase, respectively (Figure 4-4). The number of molecules per unit cell in a hexagonal lattice was estimated to be about 18 from the XRD results (Table 4-1). This phase transition from layered to columnar hexagonal can be attributed to the increased ionic volume in nanophase segregation between ionic and non-ionic parts, and a change in the molecular shape from a linear to a conical form. To gain further insight into the self-assembled columnar structure, anisotropic ion conductivity measurements at various RH values and miscibility test with water were conducted for **ZI/IL** in the Col_{hex} phase. The columns were oriented by mechanical shearing in two directions, parallel and perpendicular to the comb-shaped gold electrodes in the anisotropic measurement cell (Figure 4-5). Unlike ionic columnar liquid crystals forming 1D channels in the center,[35] no anisotropy in conductivity was observed for the aligned **ZI/IL** (Figure 4-6). Furthermore, the contact region of **ZI/IL** with water showed no induction of smectic phases and a destabilization of the columnar phase under polarized optical microscope (Figure 4-7). These results strongly suggest that the ionophilic domains are located on the outside of the nanophase-segregated hydrophobic columns of the hexagonal mesophase

and are in sufficient contact with each other to form a surrounding 3D-interconnected ion-transport material (Figure 4-2a). In addition, the non-aligned and aligned **ZI/IL** equilibrated in a controlled humidify chamber for 2 hours show enhanced conductivities by the incorporation of water molecules (Figure 4-6). Similar water-induced conductivity increment was reported for room-temperature ionic liquids.[55-56] This is probably due to the decrease in viscosity and the accelerated ion diffusion.

For a better understanding of the intermolecular interactions, FT-IR spectra of **ZI**, **IL**, **ZI/IL**, and **ZI/IL/PVA** were measured. Measurement samples of **ZI**, **IL**, and **ZI/IL** were prepared at ambient condition. The **ZI/IL/PVA** films were stored in a controlled humidity chamber for 2 h and their IR spectra were taken under ambient condition.

Figure 4-8 shows on the fingerprint region between 1000 cm^{-1} and 1300 cm^{-1}. In the IR spectrum of **ZI**, the peaks observed at 1236 and 1036 cm^{-1} can be assigned to the asymmetric and symmetric SO_3^{-1} stretching bands, respectively. The corresponding peaks of **IL** are observed at 1253 and 1028 cm^{-1}, respectively.[57] As for the **ZI/IL** spectrum, the asymmetric SO_3^{-1} stretching motions gives a broader peak at 1245 cm^{-1} with shoulder peaks in a higher wavenumber region. Assuming the respective peaks at 1236 and 1253 cm^{-1} observed for **ZI** and **IL** have been shifted and gave the peak at 1245 cm^{-1}, these changes can be considered due to the dissociation of zwitterionic dimer and the ion paring between the zwitterions and dissociated ions of **IL**. In addition, a similar small peak shift is observed in the symmetric SO_3^{-1} stretching region. The **ZI/IL** spectrum shows a peak maximum at 1030 cm^{-1} together with a shoulder at 1037 cm^{-1}. These peaks can be assigned to the symmetric SO_3^{-1} stretching bands of the sulfonate of **IL** and the zwitterionic sulfonate of **ZI**, respectively. The peak shifting towards lower wavenumber, compared with those of pure **IL** and **ZI**, can be attributed to the weak intermolecular interactions between the zwitterionic imidazolium cation of **ZI** and the sulfonate anion of **IL**, as well as the interaction of zwitterionic sulfonate moiety of **ZI** with the dissociated imidazolium cation of **IL**.

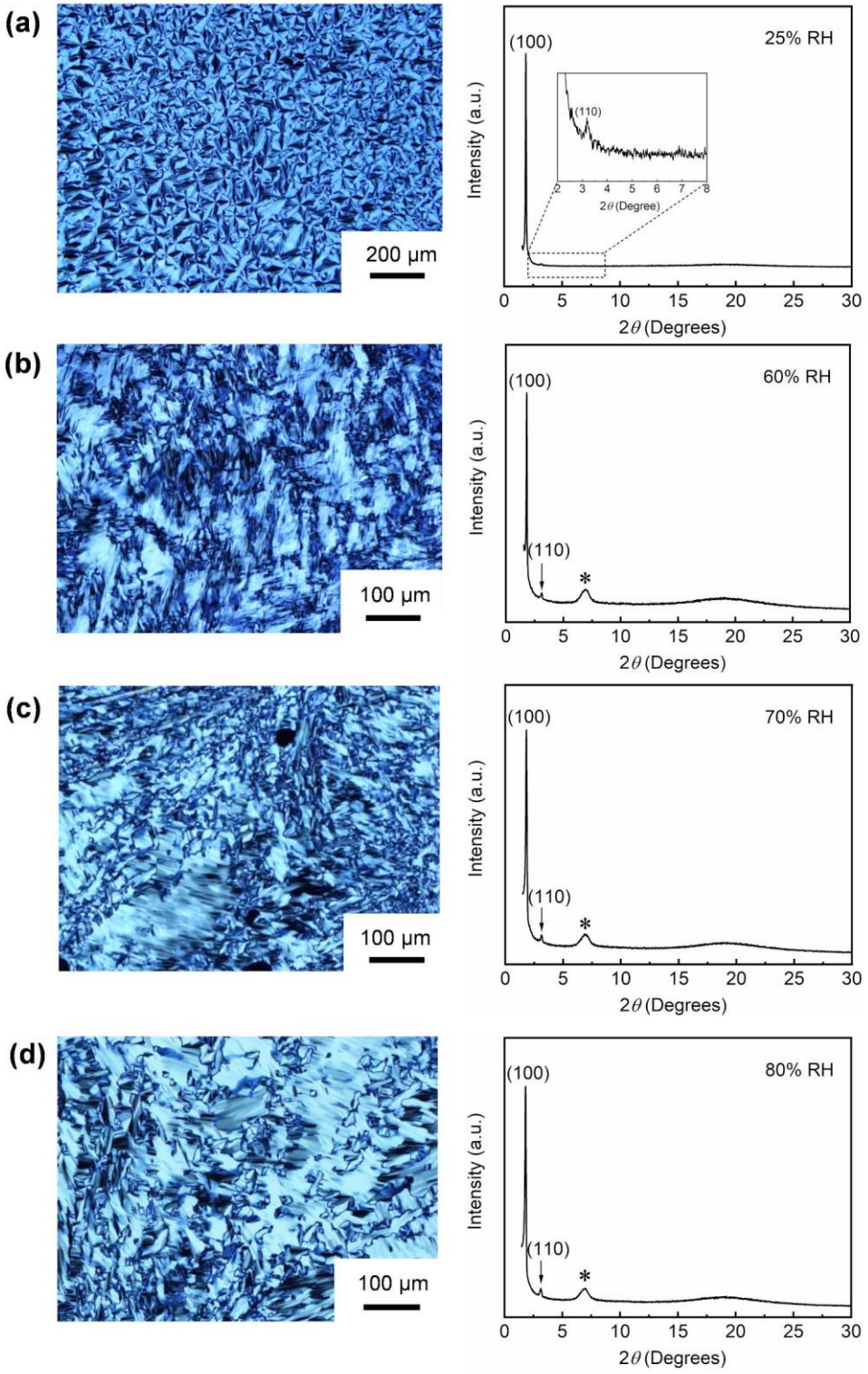

Figure 4-4. POM images and XRD patterns of **ZI/IL** at various relative humidity (RH) values: (a) 25% RH; (b) 60% RH; (c) 70% RH, and (d) 80% RH. The peak at 2θ = 7.1° (*) is attributed to the reflection of the polyimide film attached to the humidity chamber for XRD measurement.

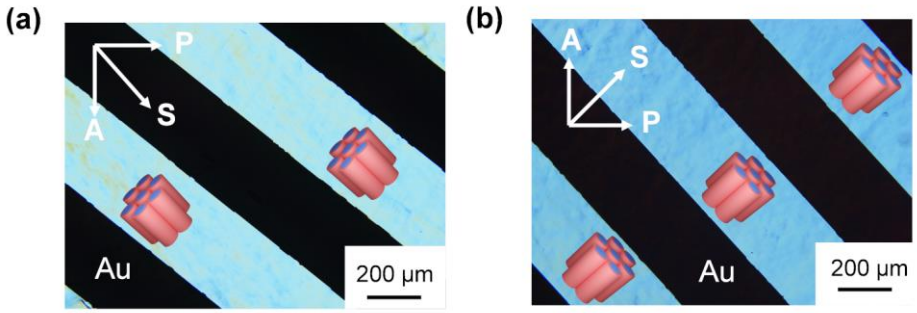

Figure 4-5. POM images of the mechanically sheared columnar phase of **ZI/IL** at ambient condition between comb-shaped gold electrodes: (a) parallel orientation of the columnar axis to the direction of electrodes (//); (b) perpendicular orientation of the columnar axis to the direction of electrodes (⊥).

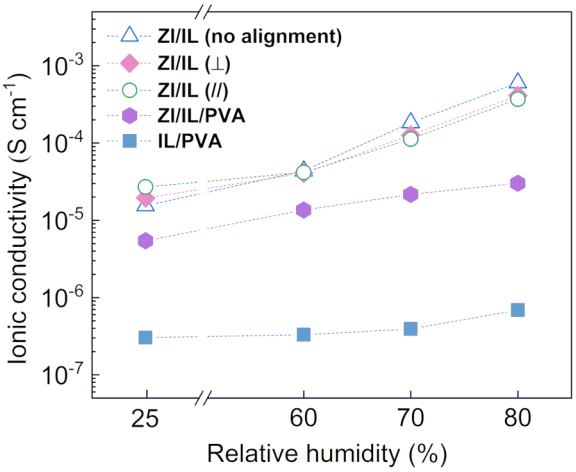

Figure 4-6. Ionic conductivities of **ZI/IL**, **IL/PVA**, and **ZI/IL/PVA** films as a function of relative humidity. **ZI/IL**(//) and **ZI/IL**(⊥) indicate the conductivities of mechanically sheared columnar phases with parallel and perpendicular orientation of the columnar axis to the direction of gold electrodes, respectively.

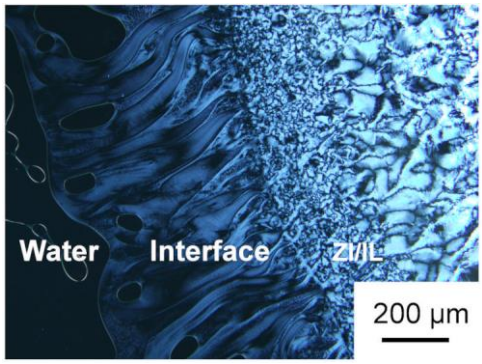

Figure 4-7. POM image of the contact region of **ZI/IL** in the columnar liquid-crystalline phase and water at ambient temperature.

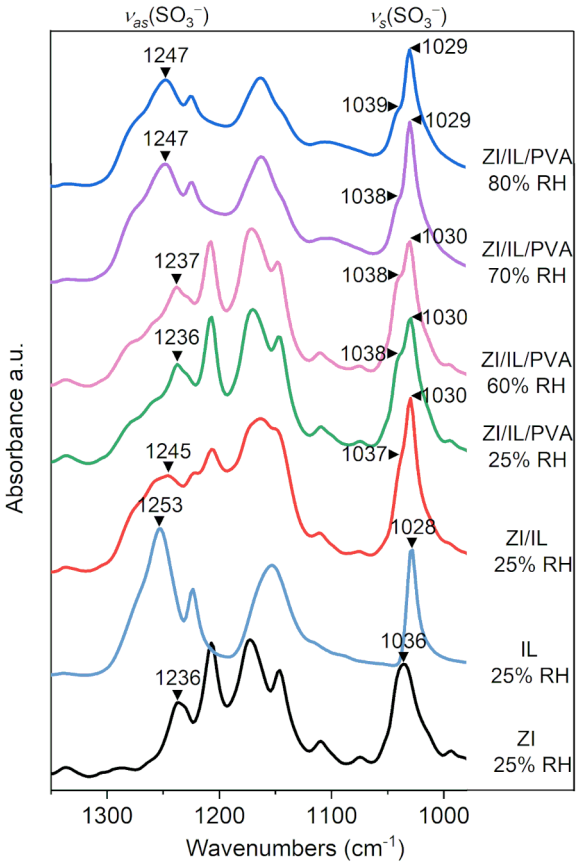

Figure 4-8. FT-IR spectra of **ZI, IL, ZI/IL** at ambient conditions, and humidified **ZI/IL/PVA**.

4.3.2 LC Properties and ionic conductivities of ZI/IL/PVA membranes

To obtain a free-standing polymer composite film, the mixing ratio of **PVA** into **ZI/IL** was optimized. As a result, the combination of **ZI/IL** (49.5 wt% of **ZI** and 27.5 wt% of **IL**) and 23 wt% of **PVA** yielded a stretchable composite film (**ZI/IL/PVA**) as shown in Figure 4-2b while maintaining the Col_{hex} structure at ambient condition. Polarized optical microscopic images of **ZI/IL/PVA** films show ambiguous fan-like textures compared with that of **ZI/IL** (Figure 4-9). The viscous **PVA** chains surrounding the hexagonal columns of **ZI/IL** may prevent the formation of large oriented domain of columns. The Young's modulus of **ZI/IL/PVA** under ambient conditions was estimated to be 1.12 MPa by tensile testing (Figure 4-10). Although the modulus of the liquid-crystalline electrolyte film is as small as one-hundredth of those of block copolymers, it is noteworthy that the stretchable material was obtained by mixing low-molecular weight ionic liquid crystal with a small amount of simple vinyl polymer. The intercolumnar distance of **ZI/IL/PVA** increased compared to that of **ZI/IL**, and the average

number of molecules in the stratum of column was reduced from 18 to 16 (Table 4-1), which may be caused by the incorporation of **PVA** into the ionic parts of columnar structures.

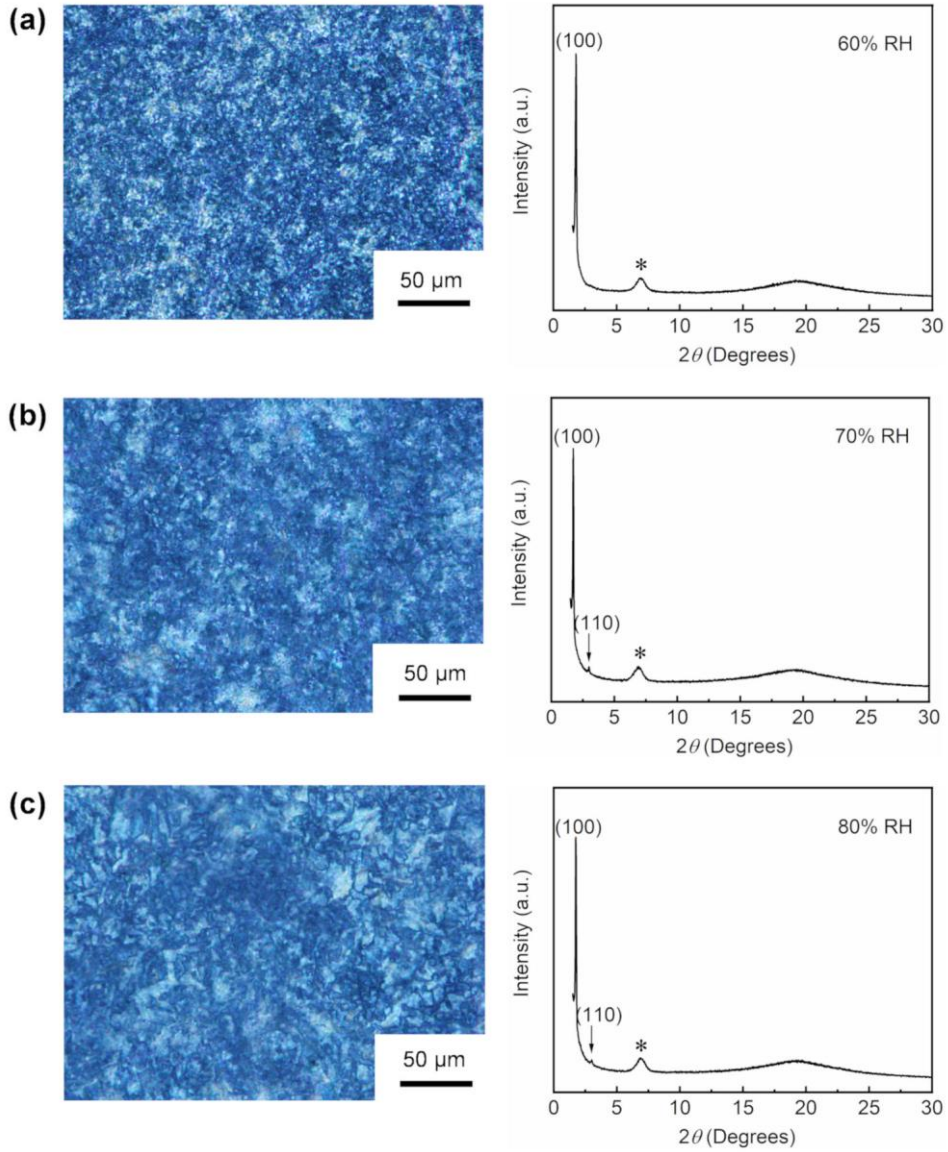

Figure 4-9. POM images and XRD patterns of the **ZI/IL/PVA** films at various relative humidity (RH) values: (a) 60% RH; (b) 70% RH, and (c) 80% RH. The peak at $2\theta = 7.1°$ (*) is attributed to the reflection of polyimide film attached to the humidity chamber for XRD measurement.

Table 4-1. Observed and calculated d-spacings, Miller Indices, lattice parameters (a) of the hexagonal columnar phases of different **ZI/IL**-based samples, and number of molecules (n) per unit cell in the hexagonal lattice estimated from the X-ray diffraction measurements for **ZI/IL** and **ZI/IL/PVA** at room temperature under the varied relative humidity.

Sample	Relative humidity (%)	*d*, obs (Å)	*d*, cal (Å)	Miller index	*a* (Å)	phase	*n*
ZI/IL	25	47.4	47.4	100	54.7	Col_{hex}	18
		27.9	27.4	110			
		4.6	-	001			
	60	49.0	49.0	100	56.6	Col_{hex}	19
		28.3	28.3	110			
		4.7	-	001			
	70	48.5	48.5	100	56.0	Col_{hex}	19
		28.2	28.0	110			
		4.6	-	001			
	80	48.9	48.9	100	56.4	Col_{hex}	19
		28.1	28.2	110			
		4.7	-	001			
ZI/IL/PVA	60	49.6	49.6	100	57.3	Col_{hex}	15
		4.6	-	001			
	70	50.9	50.9	100	58.7	Col_{hex}	16
		29.6	29.4	110			
		4.6	-	001			
	80	50.5	50.5	100	58.3	Col_{hex}	16
		29.4	29.2	110			
		4.6	-	001			

The lattice parameters (*a*) of hexagonal columnar phase and the number of molecules (*n*)

per unit cell in the hexagonal lattice are estimated as follows. The value of d_{100} is obtained from the XRD pattern. The h is average height of the stratum of a column, which is estimated from the X-ray halo around 20° due to disordered aliphatic chains and aromatic rings in the direction of the column axis. M is molecular weight (403.5 g mol^{-1} for **ZI/IL**, 524.0 g mol^{-1} for **ZI/IL/PVA**). The molecular weight is calculated by the following equation: $M_{\mathbf{ZI/IL}} = M_{\mathbf{ZI}} \times n_{\mathbf{ZI}}\% + M_{\mathbf{IL}} \times n_{\mathbf{IL}}\%$; $M_{\mathbf{ZI/IL/PVA}} = M_{\mathbf{ZI/IL}} \times n_{\mathbf{ZI/IL}}\% + M_{\mathbf{PVA}} \times n_{\mathbf{PVA}}\%$. $M_{\mathbf{PVA}} = (M_{\mathbf{poly(vinyl\ alcohol)}} \times 80\% + M_{\mathbf{poly(vinyl\ acetate)}} \times 20\%) \times 2000$, $M_{\mathbf{poly(vinyl\ alcohol)}} = 44$, $M_{\mathbf{poly(vinyl\ acetate)}} = 86$. N_A is Avogadro's number (6.02×10^{23} mol^{-1}). The density ρ is assumed to be 1.0 g cm^{-3}.

$$a = \frac{2}{\sqrt{3}} \times d_{100}$$

$$n = \frac{\sqrt{3} \times a^2 \times h \times N_A \times \rho}{2 \times M}$$

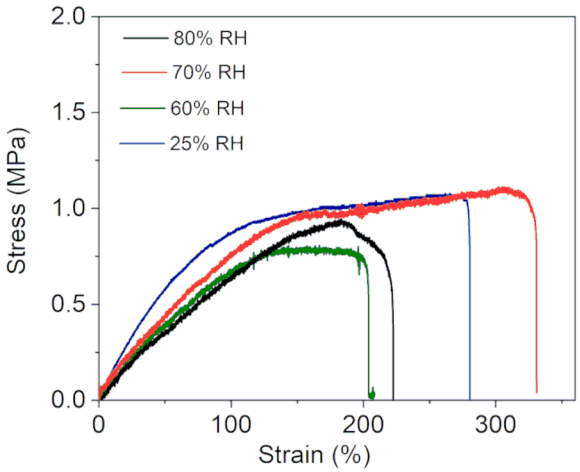

Figure 4-10. Stress vs. strain plots of the **ZI/IL/PVA** film at different relative humidity (RH) values.

The application of **ZI/IL/PVA** membrane to ionic electroactive polymer actuators poses a technical challenge because compound **ZI** gradually crystallizes at room temperature. It was found that the crystallization of **ZI** was prevented by placing the membranes under 60–80% RH and the Col_{hex} phase was stably formed at room temperature. While dry actuators able to work in air would expand the range of applications, wet actuators operated in water and a humid atmosphere also have numerous biomedical uses. For the dry **ZI/IL/PVA**, the partial crystallization of **ZI** was prevented by heating around 45 °C and the actuation behavior was observed. However, installing the instruments such as a laser displacement sensor in the oven is difficult in the present stage. In addition, to obtain room-temperature stable liquid-crystalline

materials, a new design of zwitterionic mesogenic molecule such as introducing blanched alkyl chains is necessary. Therefore, to examine the actuation performance, the humidified **ZI/IL/PVA** electrolyte membranes were employed at room temperature. The water content of the membranes reached equilibrium in 2 hours in a humidify chamber (Figure 4-11). The amount of water adsorption (W_{H2O}) for the samples of **ZI/IL** and **ZI/IL/PVA** were estimated by the difference in weight between the humidified state (W_{wet}) and their original dry state (W_{dry}) using the following equation:

$$W_{H_2O}\% = \frac{W_{wet} - W_{dry}}{W_{dry}} \times 100\%$$

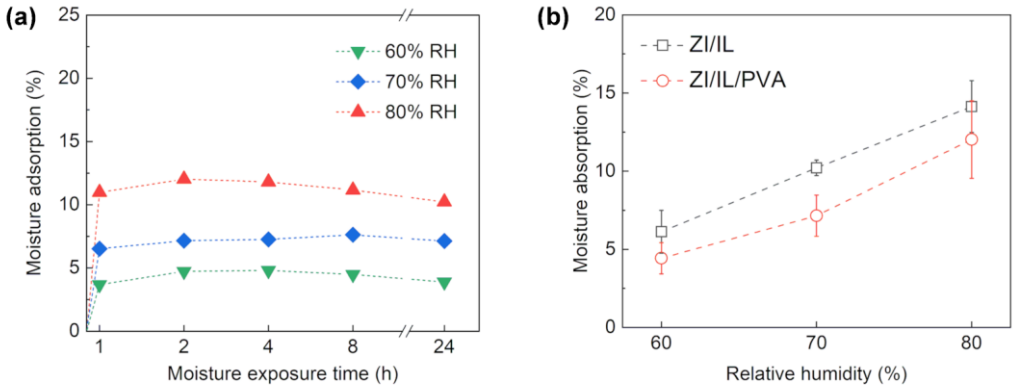

Figure 4-11. (a) Time-dependent water adsorption in weight % for samples of **ZI/IL/PVA** films under different relative humidity (RH) values; (b) Adsorbed water in weight % for samples of **ZI/IL** and **ZI/IL/PVA** films stored for 2 hours in a humidified chamber at different relative humidity.

The incorporation of water molecules into the film can cause a plasticizing effect on the interpenetrating polymer network and accelerate ion diffusion, resulting in the improved conductivities (Figure 4-6) and a lower glass transition temperature (Figure 4-12). The **ZI/IL/PVA** film at 80% RH showed the conductivity of 3.0×10^{-5} S cm^{-1} at 25 °C, which is 5.5 times higher than that at 25% RH (5.4×10^{-6} S cm^{-1}). Furthermore, the conductivity of nanostructured **ZI/IL/PVA** membrane is one order of magnitude higher than that of an amorphous membrane composed of **IL** (27.5 wt%) and **PVA** (72.5 wt%) (**IL/PVA**). The thermal properties of **ZI/IL/PVA** films stored under different humidity were examined by differential scanning calorimetry (DSC) measurement. The **ZI/IL/PVA** film obtained from RH

25% shows a glass transition at –42 °C, which can be attributed to the segmental motion of **PVA**. As the increase of relative humidity from 25% RH to 80% RH, the glass transition temperature (*Tg*) is shifted to lower temperature, probably due to the liquid-crystalline gel-like formation induced by the absorption of water into the **PVA** matrix. The plasticizing effect of relative humidity for bare Poval® PVA-224 (Kuraray, degree of hydrolysis: 87–89 mol%) was reported.[58] In addition, the DSC curves of the humidified **ZI/IL/PVA** (RH = 60–80%) exhibit a small peak between –6 and –22 °C, which can be assigned to the freezing point of mobile water chemically bound in the liquid-crystalline polymer networks.[59] The glass transition of the **IL/PVA** film was observed at 15 °C. The introduction of **ZI** into the **IL/PVA** film significantly reduced the glass transition temperature. The plasticizing effect of zwitterions was reported for the blends of single-ion conductive polymers tethering lithium salt moieties and poly(ethylene oxide).[60]

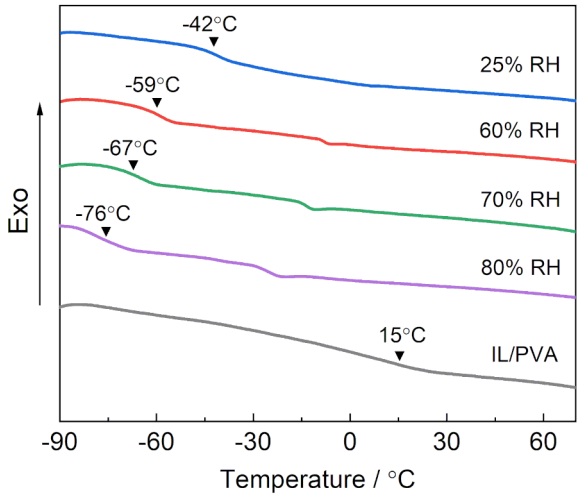

Figure 4-12. DSC curves on heating of the **ZI/IL/PVA** films stored at various relative humidity (RH) values, and the **IL/PVA** film prepared at ambient condition.

4.3.3 ZI/IL/PVA-based actuators

The **PEDOT:PSS** electrode membranes were attached to both sides of the humidified **ZI/IL/PVA** film by pressing at room temperature. The **ZI/IL/PVA** film shows good adhesion to the **PEDOT:PSS** films. The cross-section of the stacked membrane was observed by FE-SEM (Figure 4-13). The **ZI/IL/PVA** electrolyte film and the **PEDOT:PSS** films appeared to be seamlessly integrated, which was expected to facilitate ion diffusion between the electrodes

and electrolytes.

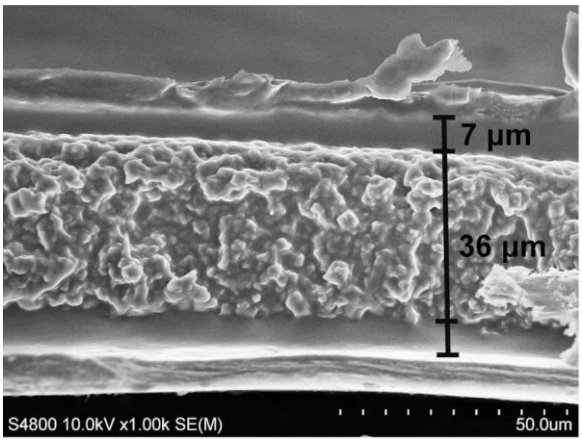

Figure 4-13. SEM image of the cross-sectional view of the actuator composed of the **ZI/IL/PVA** membrane electrolyte sandwiched between the **PEDOT:PSS** electrodes.

Here, an application of the ionic columnar liquid crystal/polymer composite electrolytes to ionic electroactive polymer actuators was shown. Figure 4-14 shows the transferred current and bending displacement of actuator strip at room temperature and the photographs under applying an alternating square voltage of ± 1 V at 0.1 Hz in a 70% RH atmosphere. The upper face of the actuator (Figure 4-14b) was connected to working electrodes and the other was attached to a counter electrode short-circuited with the reference electrode of the potentiostat. The bending displacement was measured by a laser displacement meter at 7 mm from the tip of strip. The actuator showed a bending motion against the anode side when voltage was applied. This is probably because the accumulation of cations on the cathode and anions on the anode cause a volume difference between the two sides of the electrolyte. The transient current shows a spike signal due to the rapid charging/discharging of the electric double layer formed at the electrolyte/electrode interface (Figure 4-14, middle). It determines the initial speed of bending. The measured displacement of actuator strip exhibited 2 mm within 220 ms. The displacement in a shorter time scale is shown in Figure 4-15. In addition, the spike current is followed by the slower current attributable to the Faradic redox reactions between the **PEDOT:PSS** and **IL**. The maximum peak-to-peak displacement reached 15 mm at the tip of strip (Figure 4-14b).

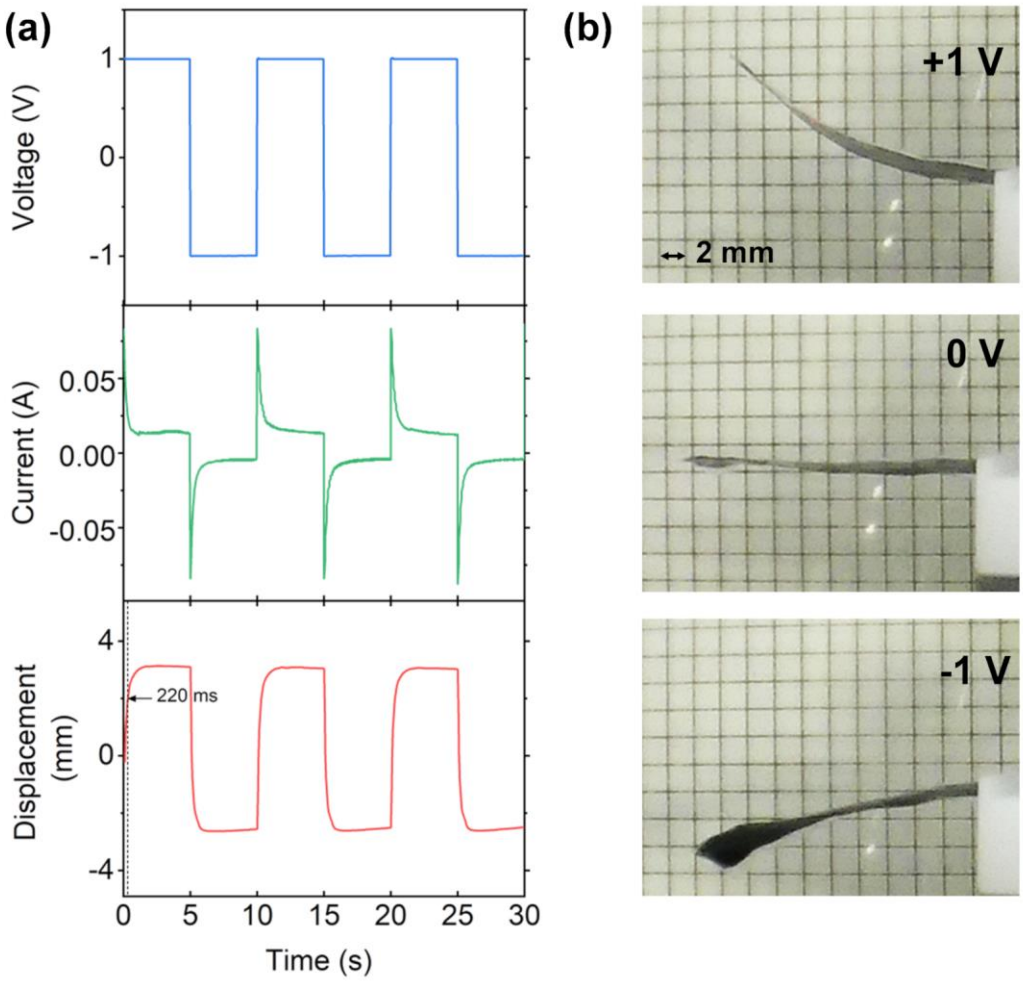

Figure 4-14. Actuation response of the **ZI/IL/PVA** electrolyte sandwiched between **PEDOT:PSS** electrodes under an AC electric field: (a) Voltage, transient current, and displacement vs. time plots; (b) Photographs of the bending actuation. The bending displacement was measured by a laser displacement meter at 7 mm from the tip of actuator strip.

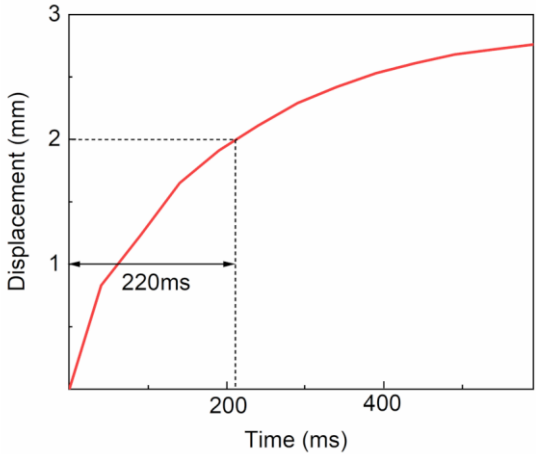

Figure 4-15. Displacement change of the **ZI/IL/PVA** actuator humidified under 70% RH in a shorter time scale under an AC voltage of ±1 V at 0.1 Hz.

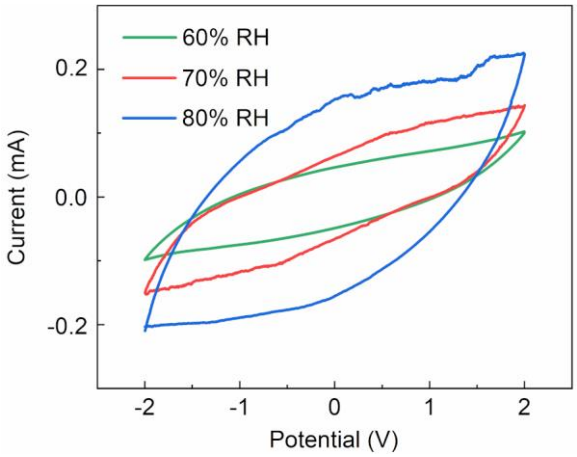

Figure 4-16. Cyclic voltammetry curves of **ZI/IL/PVA** actuators under a potential window between +2 and –2 V at a scan rate of 50 mV s^{-1} under various RH values.

To explore the actuation mechanism of **ZI/IL/PVA**-based actuators, electrochemical characterizations were examined by cyclic voltammetry (CV) test with a two electrodes configuration. The CV curves of **ZI/IL/PVA** actuators under 60–80% RH in a potential window from –2 to +2 V in a scan rate of 50 mV s^{-1} (Figure 4-16) exhibit box-type characteristics and no obvious redox peaks of **PEDOT:PSS** were seen. These results suggest that the strain induced in the electrolyte/electrode interfaces by the formation of an electrostatic double-layer is the dominant actuation mechanism. The value of specific capacitance was calculated to be 2.4–7.5 mF cm^{-2} from the integrated area of CV curves at 60%–80% RH, which is lower than those for ion polymer gel electrolytes (33.4–44.5 mF cm^{-2}).[61] The lower capacitance is assumed to be

due to the lower ionic liquid content and smaller surface area of **PEDOT:PSS** films compared to porous carbon electrodes.

The voltage and frequency dependence of the actuator at 70% RH was further investigated using alternating square-wave voltages of ±0.5, ±1, and ±2 V and frequencies of 0.05, 0.1, and 1.0 Hz. The actuator can move over at voltage range of ±0.5 V and show cycling stability over 3600 cycles (Figure 4-17). The peak-to-peak displacement of the actuator at the tip increases as the voltage increases (Figure 4-18), probably due to the increase of charges accumulated at the electrolyte/electrode interface. In addition, the displacement shows a tendency to decrease with increasing frequency because of the decrease in the stored charge at the electrode layer at higher frequencies (Figure 4-19).

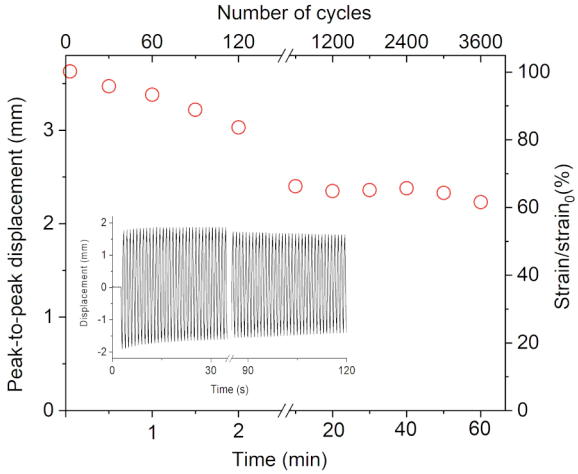

Figure 4-17. Cycling stability of the **ZI/IL/PVA** actuators under an AC voltage of ±1 V at 1 Hz at 70% RH. The bending strain for each cycle is normalized by the initial strain value (strain0).

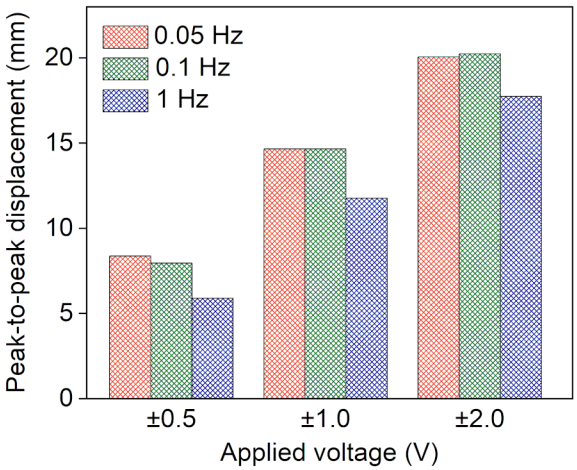

Figure 4-18. Tip displacement of **ZI/IL/PVA** actuator under applying voltages of ±0.5, ±1, and ±2 V with frequencies of 0.05, 0.1, and 1.0 Hz in the 70% RH environment. The tip displacement was

estimated from the photograph of bending actuators.

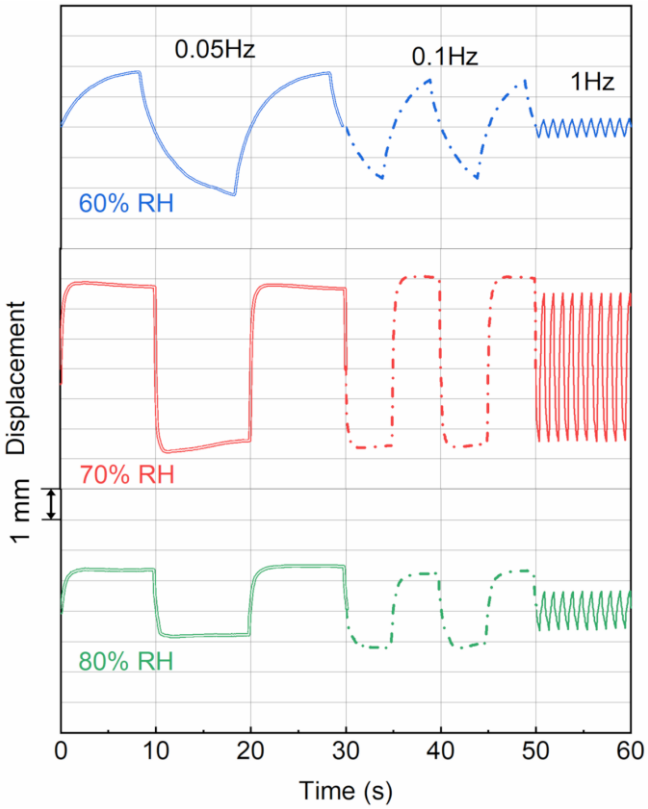

Figure 4-19. Displacement of the **ZI/IL/PVA** actuator at various frequency and relative humidity (RH) values. The applied voltage is ±1 V. The displacement at 7 mm away from the tip of actuator strip was recorded.

RH was found to be an important factor that affects the bending behavior. The **ZI/IL/PVA** electrolyte film was able to absorb more water molecules under a high-humidity atmosphere, which resulted in the formation of more mobile ion channels and increased ionic conductivity through hydrogen-bonded networks between water molecules, the hydroxyl groups of **PVA**, and the sulfonate anions of **ZI** and **IL**. It was expected that the higher the RH value, the larger the displacement. To show the time-dependent displacement change at AC 2 V and 1 Hz under varied RH conditions, the displacement at 7 mm from the tip of strip was monitored by a laser displacement meter (Figure 4-20). The displacement values shown in Figure 4-20 are about one order of magnitude smaller than the tip displacement seen in Figure 4-18 estimated from the photographs of bending actuators, because the bending displacement is over the working distance of a laser displacement sensor under AC 2V at low frequency. The bending

displacement at 70% RH (red line) is more than two times larger than that attained at 60% RH (green line), as shown in Figure 4-20. However, the displacement at 80% RH (blue dot line) becomes smaller than that obtained at 70% RH. In contrast, the electrical conductivity of **PEDOT: PSS** films showed no significant change by varying the humidity from 25% to 80% RH. From these results, the reduced displacement at 80% RH is hypothesized to be due to the obstruction of ion migration because of the partial electrolysis of absorbed water.

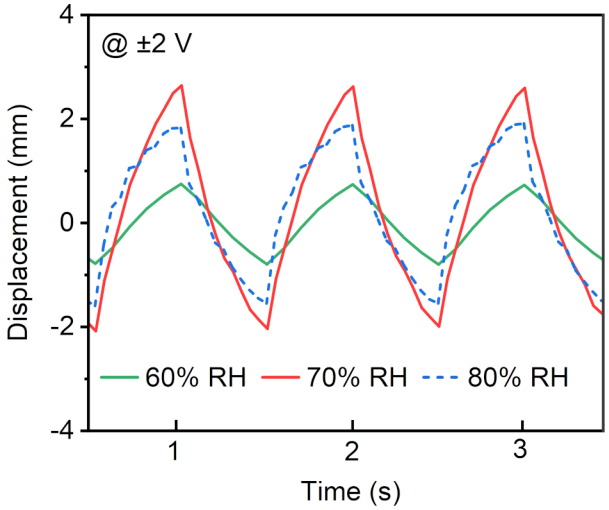

Figure 4-20. Displacement of **ZI/IL/PVA** actuator vs. time under AC voltage of ±2 V, 1 Hz at 60, 70, and 80% RH, monitored at 7 mm from the tip of strip.

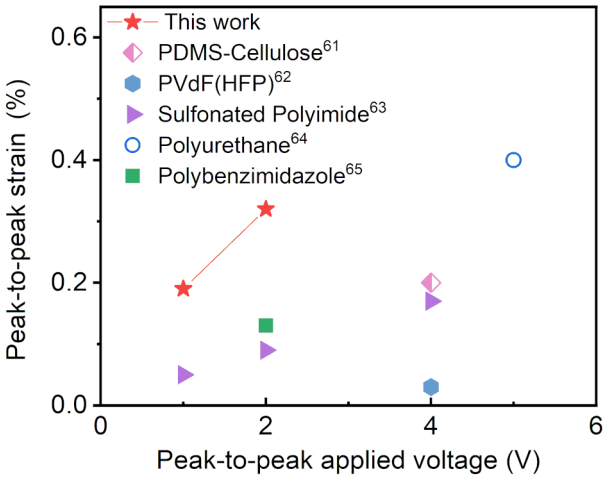

Figure 4-21. Peak-to-peak strain vs. peak-to-peak voltage plots of **ZI/IL/PVA** actuators at 70% RH and other ionic electroactive polymer actuators with **PEDOT:PSS** electrodes operating at 0.1 Hz.

The peak-to-peak bending strain (ε) in 70% RH was estimated from the peak-to-peak displacement (δ), thickness (d), and length (L) of actuator strip using the following equation: $\varepsilon = 2\delta d \times 100/(\delta^2 + L^2)$. The displacement of actuator at 13 mm from the clamped end was used for the calculation (L = 13 mm). The strain of **ZI/IL/PVA** actuators under 70% RH became larger with increasing an applied voltage. The actuator under applying 1 V with a frequency of 0.1 Hz attains the maximum peak-to-peak strain of 0.32%, while the strain value at 0.5 V, 0.1 Hz is 0.19%. The peak-to-peak strain of **ZI/IL/PVA** actuators at 0.1 Hz was compared with other ionic electroactive polymer actuators using the same conducting polymer electrodes (Figure 4-21), such as poly(dimethylsiloxane)—cellulose nanofiber/ionic liquid (57 wt%),[61] poly(vinylidene fluoride)-co-hexafluoropropylene/ionic liquid (67 wt%),[62] sulfonated polyimide block copolymer/ionic liquid (80 wt%),[63] polyurethane/ionic liquid (50 wt%),[64] and sulfonated polybenzimidazole/ionic liquid (70 wt%).[65] The peak-to-peak strains obtained from these electrolytes ranged from ca. 0.05 to 0.4 %, although different types of ionic liquids were used. The nanostructured electrolyte system developed in this study was able to generate larger strains even with a smaller amount of ionic liquid, which can contribute to reduce the risk of ionic liquid leakage and the production cost. Besides, the energy conversion efficiency (η) of **ZI/IL/PVA** actuator can reach to 1.07% at an AC voltage of ±1 V with a frequency of 0.1 Hz under 60% RH condition, which was comparable with reported ion gel actuator containing 50 wt% of **IL**s.[64] By increasing the frequency to 1 Hz, the value of η was decreased to 0.31%. Furthermore, it is worth noting that the 3D continuous ionic nanochannels were effective in achieving a faster actuation response (0.79 s for a 3.2 mm swing from one side to the opposite side at 0.5 V), compared to the microphase-segregated channels of PS-*b*-PSS block copolymer, which took 5 s for 8.2 mm bending displacement.[66] More importantly, it was found that the nanostructured **ZI/IL/PVA** actuators exhibited a faster and larger bending actuation than a control actuator with an amorphous **IL/PVA** membrane electrolyte at 70% RH. When the electric field was changed from +0.5 V to –0.5 V, the bending speeds of the **ZI/IL/PVA** and the **IL/PVA** actuators are 4.0 and 1.9 mm/s, respectively (Figure 4-22). These positive impacts on the actuation behavior for the nanostructured **ZI/IL/PVA** electrolyte may be due to the synergetic effects of more efficient ion migration in the proposed interconnected 3D ion matrix and plasticization of the polymer matrix by the intermolecular interactions of the zwitterionic molecules and **PVA**.

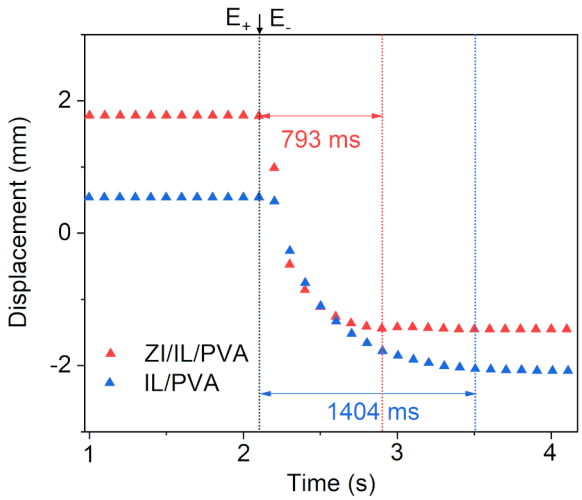

Figure 4-22. Response time of the **ZI/IL/PVA** and **IL/PVA** actuators under an AC voltage of ±0.5 V with a frequency of 0.05 Hz at 70% RH.

4.4 Conclusions

A self-standing, flexible columnar ionic liquid crystal/polymer composite membrane electrolyte forming 3D continuous ion channels by the supramolecular self-assembly of a zwitterionic rod-shaped mesogenic compound, an ionic liquid, and poly(vinyl alcohol) was successfully constructed. The stable hexagonal columnar liquid-crystalline phase was founded in the humidified nanostructured polymer film at room temperature and ionic conductivities was shown to be enhanced. A fast and large bending actuation was achieved at 1 V by sandwiching of **ZI/IL/PVA** electrolyte membrane between two conducting **PEDOT:PSS** films. A promising new route was demonstrated to construct tailor-made soft actuators and sensors for advanced applications in soft robotics and haptics.

4.5 References

1. Asaka, K.; Okuzaki, H., *Soft Actuators: Materials, Modeling, Applications, and Future Perspectives*. 2nd ed.; Springer: Singapore, 2019.

2. Zhai, Y.; Wang, Z.; Kwon, K.-S.; Cai, S.; Lipomi, D. J.; Ng, T. N., Printing Multi-Material Organic Haptic Actuators. *Adv. Mater.* **2021,** *33* (19), 2002541.

3. Hines, L.; Petersen, K.; Lum, G. Z.; Sitti, M., Soft Actuators for Small-Scale Robotics. *Adv. Mater.*

2017, *29* (13).

4. Martins, P.; Correia, D.; Correia, V.; Lanceros-Mendez, S., Polymer-Based Actuators: Back to the Future. *PCCP* **2020,** *22* (27), 15163–15182.

5. Dong, Y. Q.; Yeung, K. W.; Tang, C. Y.; Law, W. C.; Tsui, G. C. P.; Xie, X. L., Development of Ionic Liquid-Based Electroactive Polymer Composites Using Nanotechnology. *Nanotechnol. Rev.* **2021,** *10* (1), 99–116.

6. Chang, L. F.; Liu, Y. F.; Yang, Q.; Yu, L. F.; Liu, J. Q.; Zhu, Z. C.; Lu, P.; Wu, Y. C.; Hu, Y., Ionic Electroactive Polymers Used in Bionic Robots: A Review. *J. Bionic Eng.* **2018,** *15* (5), 765–782.

7. Chen, D.; Pei, Q., Electronic Muscles and Skins: A Review of Soft Sensors and Actuators. *Chem. Rev.* **2017,** *117* (17), 11239–11268.

8. Ueki, T.; Watanabe, M., Macromolecules in Ionic Liquids: Progress, Challenges, and Opportunities. *Macromolecules* **2008,** *41* (11), 3739–3749.

9. Fukushima, T.; Asaka, K.; Kosaka, A.; Aida, T., Fully Plastic Actuator Through Layer-by-Layer Casting with Ionic-Liquid-Based Bucky Gel. *Angew. Chem. Int. Ed.* **2005,** *44* (16), 2410–2413.

10. Osada, I.; de Vries, H.; Scrosati, B.; Passerini, S., Ionic-Liquid-Based Polymer Electrolytes for Battery Applications. *Angew. Chem. Int. Ed.* **2016,** *55* (2), 500–513.

11. Carrico, J. D.; Tyler, T.; Leang, K. K., A Comprehensive Review of Select Smart Polymeric and Gel Actuators for Soft Mechatronics and Robotics Applications: Fundamentals, Freeform Fabrication, and Motion Control. *Int. J. Smart Nano Mater.* **2017,** *8* (4), 144–213.

12. Elwan, H. A.; Thimmappa, R.; Mamlouk, M.; Scott, K., Applications of Poly Ionic Liquids in Proton Exchange Membrane Fuel Cells: A review. *J. Power Sources* **2021,** *510*, 29.

13. Jeong, J.; Marques, G. C.; Feng, X.; Boll, D.; Singaraju, S. A.; Aghassi-Hagmann, J.; Hahn, H.; Breitung, B., Ink-Jet Printable, Self-Assembled, and Chemically Crosslinked Ion-Gel as Electrolyte for Thin Film, Printable Transistors. *Adv. Mater. Interfaces* **2019,** *6* (21), 1901074.

14. White, B. T.; Long, T. E., Advances in Polymeric Materials for Electromechanical Devices. *Macromol. Rapid Commun.* **2019,** *40* (1), 1800521.

15. Swann, J. M.; Topham, P. D., Design and Application of Nanoscale Actuators Using Block-Copolymers. *Polymers* **2010,** *2* (4), 454–469.

16. Kim, O.; Kim, S. J.; Park, M. J., Low-Voltage-Driven Soft Actuators. *Chem Commun (Camb)* **2018,** *54* (39), 4895–4904.

17. Kim, O.; Kim, S. Y.; Park, B.; Hwang, W.; Park, M. J., Factors Affecting Electromechanical Properties of Ionic Polymer Actuators Based on Ionic Liquid-Containing Sulfonated Block Copolymers. *Macromolecules* **2014,** *47* (13), 4357–4368.

18. Song, J.; Jeon, J. H.; Oh, I. K.; Park, K. C., Electro-active Polymer Actuator Based on Sulfonated

Polyimide with Highly Conductive Silver Electrodes via Self-Metallization. *Macromol. Rapid Commun.* **2011,** *32* (19), 1583–1587.

19. Rajagopalan, M.; Jeon, J.-H.; Oh, I.-K., Electric-Stimuli-Responsive Bending Actuator Based on Sulfonated Polyetherimide. *Sens. Actuators, B* **2010,** *151* (1), 198–204.

20. Rajagopalan, M.; Oh, I.-K., Fullerenol-Based Electroactive Artificial Muscles Utilizing Biocompatible Polyetherimide. *ACS nano* **2011,** *5* (3), 2248–2256.

21. Imaizumi, S.; Ohtsuki, Y.; Yasuda, T.; Kokubo, H.; Watanabe, M., Printable Polymer Actuators from Ionic Liquid, Soluble Polyimide, and Ubiquitous Carbon Materials. *ACS Appl. Mater. Interfaces* **2013,** *5* (13), 6307–6315.

22. Kwon, T.; Cho, H.; Lee, J.-W.; Henkensmeier, D.; Kang, Y.; Koo, C. M., Sulfonated Copper Phthalocyanine/sulfonated Polysulfone Composite Membrane for Ionic Polymer Actuators with High Power Density and Fast Response Time. *ACS Appl. Mater. Interfaces* **2017,** *9* (34), 29063–29070.

23. Duncan, A. J.; Layman, J. M.; Cashion, M. P.; Leo, D. J.; Long, T. E., Oligomeric A2+ B3 Synthesis of Highly Branched Polysulfone Ionomers: Novel Candidates for Ionic Polymer Transducers. *Polym. Int.* **2010,** *59* (1), 25–35.

24. Tas, S.; Zoetebier, B.; Sukas, O. S.; Bayraktar, M.; Hempenius, M.; Vancso, G. J.; Nijmeijer, K., Ion-Selective Ionic Polymer Metal Composite (IPMC) Actuator Based on Crown Ether Containing Sulfonated Poly (Arylene Ether Ketone). *Macromol. Mater. Eng.* **2017,** *302* (4), 1600381.

25. Guo, D.; Han, Y.; Huang, J.; Meng, E.; Ma, L.; Zhang, H.; Ding, Y., Hydrophilic Poly(vinylidene Fluoride) Film with Enhanced Inner Channels for Both Water- and Ionic Liquid-Driven Ion-Exchange Polymer Metal Composite Actuators. *ACS Appl. Mater. Interfaces* **2019,** *11* (2), 2386–2397.

26. Yan, Y.; Santaniello, T.; Bettini, L. G.; Minnai, C.; Bellacicca, A.; Porotti, R.; Denti, I.; Faraone, G.; Merlini, M.; Lenardi, C.; Milani, P., Electroactive Ionic Soft Actuators with Monolithically Integrated Gold Nanocomposite Electrodes. *Adv. Mater.* **2017,** *29* (23).

27. Simaite, A.; Tondu, B.; Souères, P.; Bergaud, C., Hybrid PVDF/PVDF-graft-PEGMA Membranes for Improved Interface Strength and Lifetime of PEDOT:PSS/PVDF/Ionic Liquid Actuators. *ACS Appl. Mater. Interfaces* **2015,** *7* (36), 19966–19977.

28. Kato, T.; Yoshio, M.; Ichikawa, T.; Soberats, B.; Ohno, H.; Funahashi, M., Transport of Ions and Electrons in Nanostructured Liquid Crystals. *Nat. Rev. Mater.* **2017,** *2* (4).

29. Cho, B.-K., Nanostructured Organic Electrolytes. *RSC Adv.* **2014,** *4* (1), 395–405.

30. Goossens, K.; Lava, K.; Bielawski, C. W.; Binnemans, K., Ionic Liquid Crystals: Versatile Materials. *Chem. Rev.* **2016,** *116* (8), 4643–4807.

31. Beginn, U.; Zipp, G.; Mourran, A.; Walther, P.; Möller, M., Membranes Containing Oriented Supramolecular Transport Channels. *Adv. Mater.* **2000,** *12* (7), 513–516.

32. Ramón-Gimenez, L.; Storz, R.; Haberl, J.; Finkelmann, H.; Hoffmann, A., Anisotropic Ionic Mobility of Lithium Salts in Lamellar Liquid Crystalline Polymer Networks. *Macromol. Rapid Commun.* **2012,** *33* (5), 386–391.

33. Yildirim, A.; Szymoniak, P.; Sentker, K.; Butschies, M.; Bühlmeyer, A.; Huber, P.; Laschat, S.; Schönhals, A., Dynamics and Ionic Conductivity of Ionic Liquid Crystals Forming a Hexagonal Columnar Mesophase. *PCCP* **2018,** *20* (8), 5626–5635.

34. Concellón, A.; Liang, T.; Schenning, A. P.; Serrano, J. L.; Romero, P.; Marcos, M., Proton-Conductive Materials Formed by Coumarin Photocrosslinked Ionic Liquid Crystal Dendrimers. *J. Mater. Chem. C* **2018,** *6* (5), 1000–1007.

35. Yoshio, M.; Mukai, T.; Ohno, H.; Kato, T., One-Dimensional Ion Transport in Self-Organized Columnar Ionic Liquids. *J. Am. Chem. Soc.* **2004,** *126* (4), 994–995.

36. Ichikawa, T.; Yoshio, M.; Hamasaki, A.; Mukai, T.; Ohno, H.; Kato, T., Self-Organization of Room-Temperature Ionic Liquids Exhibiting Liquid-Crystalline Bicontinuous Cubic Phases: Formation of Nano-Ion Channel Networks. *J. Am. Chem. Soc.* **2007,** *129* (35), 10662–10663.

37. Sakuda, J.; Hosono, E.; Yoshio, M.; Ichikawa, T.; Matsumoto, T.; Ohno, H.; Zhou, H. S.; Kato, T., Liquid-Crystalline Electrolytes for Lithium-Ion Batteries: Ordered Assemblies of a Mesogen-Containing Carbonate and a Lithium Salt. *Adv. Funct. Mater.* **2015,** *25* (8), 1206–1212.

38. Yang, J.; Tan, S.; Xie, W.; Luo, J.; Wang, C.; Wu, Y., Promotion of Anhydrous Proton Conduction by Polyvinyl Alcohol in Liquid Crystalline Composite Membranes Containing 1-Tetradecyl-3-methylimidazolium Hydrogen Sulfate. *Ionics* **2020,** *26* (4), 1819–1827.

39. Högberg, D.; Soberats, B.; Yatagai, R.; Uchida, S.; Yoshio, M.; Kloo, L.; Segawa, H.; Kato, T., Liquid-Crystalline Dye-Sensitized Solar Cells: Design of Two-Dimensional Molecular Assemblies for Efficient Ion Transport and Thermal Stability. *Chem. Mater.* **2016,** *28* (18), 6493–6500.

40. Bresser, D.; Leclere, M.; Bernard, L.; Rannou, P.; Mendil-Jakani, H.; Kim, G. T.; Zinkevich, T.; Indris, S.; Gebel, G.; Lyonnard, S.; Picard, L., Organic Liquid Crystals as Single-Ion Li(+) Conductors. *ChemSusChem* **2021,** *14* (2), 655–661.

41. Feng, X.; Tousley, M. E.; Cowan, M. G.; Wiesenauer, B. R.; Nejati, S.; Choo, Y.; Noble, R. D.; Elimelech, M.; Gin, D. L.; Osuji, C. O., Scalable Fabrication of Polymer Membranes with Vertically Aligned 1 nm Pores by Magnetic Field Directed Self-Assembly. *Acs Nano* **2014,** *8* (12), 11977–11986.

42. Kerr, R. L.; Miller, S. A.; Shoemaker, R. K.; Elliott, B. J.; Gin, D. L., New Type of Li Ion Conductor with 3D Interconnected Nanopores via Polymerization of a Liquid Organic Electrolyte-Filled Lyotropic Liquid-Crystal Assembly. *J. Am. Chem. Soc.* **2009,** *131* (44), 15972–15973.

43. Kobayashi, T.; Li, Y.-x.; Ono, A.; Zeng, X.-b.; Ichikawa, T., Gyroid Structured Aqua-Sheets With Sub-Nanometer Thickness Enabling 3D Fast Pproton Relay Conduction. *Chem. Sci.* **2019,** *10* (25),

6245–6253.

44. Nguyen, M. L.; Kim, H.-J.; Cho, B.-K., Ionic Effects on the Self-Assembly, Molecular Dynamics and Conduction Properties of A 1,2,3-Triazole-Based Amphiphile. *J. Mater. Chem. C* **2018,** *6* (36), 9802–9810.

45. White, T. J.; Broer, D. J., Programmable and Adaptive Mmechanics with Liquid Crystal Polymer Networks and Elastomers. *Nat. Mater.* **2015,** *14* (11), 1087–1098.

46. Zhu, C.; Lu, Y.; Jiang, L.; Yu, Y., Liquid Crystal Soft Actuators and Robots toward Mixed Reality. *Adv. Funct. Mater.* **2021**, 2009835.

47. Ohm, C.; Brehmer, M.; Zentel, R., Liquid Crystalline Elastomers as Actuators and Sensors. *Adv. Mater.* **2010,** *22* (31), 3366–3387.

48. da Cunha, M. P.; Debije, M. G.; Schenning, A., Bioinspired Light-Driven Soft Robots Based on Liquid Crystal Polymers. *Chem. Soc. Rev.* **2020,** *49* (18), 6568–6578.

49. Kihara, H.; Yoshida, M., Reversible Bulk-Phase Change of Anthroyl Compounds for Photopatterning Based on Photodimerization in the Molten State and Thermal Back Reaction. *ACS Appl. Mater. Interfaces* **2013,** *5* (7), 2650–2657.

50. Shi, Y.-X.; Wu, Y.; Wang, S.-Q.; Zhao, Y.-Y.; Li, T.; Yang, X.-Q.; Zhang, T., Soft Electrochemical Actuators with a Two-Dimensional Conductive Metal–Organic Framework Nanowire Array. *J. Am. Chem. Soc.* **2021,** *143* (10), 4017–4023.

51. Cottinet, P. J.; Souders, C.; Labrador, D.; Porter, S.; Liang, Z.; Wang, B.; Zhang, C., Nonlinear Strain–Electric Field Relationship of Carbon Nanotube Buckypaper/Nafion Actuators. *Sens. Actuators, A* **2011**, *170* (1–2), 164–171.

52. Ohno, H.; Yoshizawa-Fujita, M.; Kohno, Y., Design and Properties of Functional zwitterions Derived From Ionic Liquids. *PCCP* **2018,** *20* (16), 10978–10991.

53. Soberats, B.; Yoshio, M.; Ichikawa, T.; Taguchi, S.; Ohno, H.; Kato, T., 3D Anhydrous Proton-Transporting Nanochannels Formed by Self-Assembly of Liquid Crystals Composed of a Sulfobetaine and A Sulfonic Acid. *J. Am. Chem. Soc.* **2013,** *135* (41), 15286–15289.

54. Lind, F.; Rebollar, L.; Bengani-Lutz, P.; Asatekin, A.; Panzer, M. J., Zwitterion-Containing Ionogel Electrolytes. *Chem. Mater.* **2016,** *28* (23), 8480–8483.

55. Schröder, U.; Wadhawan, J. D.; Compton, R. G.; Marken, F.; Suarez, P. A. Z.; Consorti, C. S.; de Souza, R. F.; Dupont, J., Water-Induced Accelerated Ion Diffusion: Voltammetric Studies in 1-Methyl-3-[2,6-(S)-dimethylocten-2-yl]imidazolium Tetrafluoroborate, 1-Butyl-3-methylimidazolium Tetrafluoroborate and Hexafluorophosphate Ionic Liquids. *New J. Chem.* **2000,** *24* (12), 1009–1015.

56. Widegren, J. A.; Saurer, E. M.; Marsh, K. N.; Magee, J. W., Electrolytic Conductivity of Four Imidazolium-Based Room-Temperature Ionic Liquids and the Effect of a Water Impurity. , *J. Chem.*

Thermodyn. **2005,** *37* (6), 569–575.

57. Schwenzer, B.; Kerisit, S. N.; Vijayakumar, M., Anion Pairs in Room Temperature Ionic Liquids Predicted by Molecular Dynamics Simulation, Verified by Spectroscopic Characterization. *RSC Adv.* **2014,** *4*(11), 5457.

58. Hu, H.; Zhang, X.; He, Y.; Guo, Z.-s.; Zhang, J.; Song, Y., Combined Effect of Relative Humidity and Temperature on Dynamic Viscoelastic Properties and Glass Transition of Poly(vinyl alcohol). *J. Appl. Polym. Sci.* **2013,** *130* (5), 3161–3167.

59. Zhang, W.; Wu, B.; Sun, S.; Wu, P., Skin-Like Mechanoresponsive Self-Healing Ionic Elastomer from Supramolecular Zwitterionic Network. *Nat. Commun.* **2021,** *12* (1), 4082.

60. Lu, F.; Li, G.; Yu, Y.; Gao, X.; Zheng, L.; Chen, Z., Zwitterionic Impetus on Single Lithium-Ion Conduction in Solid Polymer Electrolyte for All-Solid-State Lithium-Ion Batteries. *Chem. Eng. J.* **2020,** *384*, 123237.

61. Terasawa, N., Self-Standing High-Performance Transparent Actuator Based on Poly(dimethylsiloxane)/TEMPO-Oxidized Cellulose Nanofibers/Ionic Liquid Gel. *Langmuir* **2020,** *36* (22), 6154–6159.

62. Terasawa, N.; Asaka, K., High-Performance PEDOT:PSS/Single-Walled Carbon Nanotube/Ionic Liquid Actuators Combining Electrostatic Double-Layer and Faradaic Capacitors. *Langmuir* **2016,** *32* (28), 7210–7218.

63. Cheedarala, R. K.; Jeon, J.-H.; Kee, C.-D.; Oh, I.-K., Bio-Inspired All-Organic Soft Actuator Based on a π-π Stacked 3D Ionic Network Membrane and Ultra-Fast Solution Processing. *Adv. Funct. Mater.* **2014,** *24* (38), 6005–6015.

64. Wang, D.; Lu, C.; Zhao, J.; Han, S.; Wu, M.; Chen, W., High Energy Conversion Efficiency Conducting Polymer Actuators bBased on PEDOT:PSS/MWCNTs Composite Electrode. *RSC Advances* **2017,** *7* (50), 31264–31271.

65. Kotal, M.; Kim, J.; Kim, K. J.; Oh, I.-K., Sulfur and Nitrogen Co-Doped Graphene Electrodes for High-Performance Ionic Artificial Muscles. *Adv. Mater.* **2016,** *28* (8), 1610–1615.

66. Nguyen, V. H.; Kim, J.; Tabassian, R.; Kotal, M.; Jun, K.; Oh, J. H.; Son, J. M.; Manzoor, M. T.; Kim, K. J.; Oh, I. K., Electroactive Artificial Muscles Based on Functionally Antagonistic Core-Shell Polymer Electrolyte Derived from PS-b-PSS Block Copolymer. *Adv. Sci.* **2019,** *6* (5).

Chapter 5 Conclusions and prospectives

5.1 General conclusions

In this study, a new type of **iEAP** actuators based on columnar **LC** electrolytes was developed. The ordered molecular structure in **LC** electrolytes provided 1D and 3D continuous nanochannels for ion transporting. The **LC**-based actuators exhibited fast and large bending performance and generated large blocking force under low voltage. The factors that affected on actuation performance were investigated. The low-voltage driven **LC**-based actuators can be operated in both dry and humid environment, which have a wide application for soft actuators, biomedicals, and virtual reality.

This thesis was divided into three parts and the detailed conclusion was following:

1. Ion-conductive polymer electrolytes with 1D columnar nanostructure obtained from lyotropic and thermotropic **LC**-assembly of fan-shaped zwitterionic molecules and ionic liquids.

A new design of fan-shaped zwitterionic molecules with an imidazolium sulfobetaine moiety was prepared. Two types of columnar **LC** assemblies (lyotropic and thermotropic) were induced by associating with different protic ionic liquids. The hydrous and anhydrous ion conductive polymer membranes with 1D nanostructure were obtained by *in situ* photopolymerization of lyotropic and thermotropic **LC** monomers at columnar phase. The conductivity of anhydrous **LC** polymer membrane was shown to be 10^{-6}–10^{-9} S cm^{-1} at room temperature. The conductivity of hydrous **LC** polymer membrane was reached the order of 10^{-4}–10^{-3} S cm^{-1} at room temperature. Furthermore, it was shown that the nanostructured **LC** polymers own 100–1000 times higher conductivity compared to the corresponding amorphous polymer films. The 1D columnar transporting nanochannels was demonstrated that can facilitate ion migration in the polymer. In this section, the free-standing polymer membranes with 1D columnar **LC** nanostructure were obtained which can provide a new strategy for actuator application.

2. Evaluation and discussion of actuation performance for 1D nanostructured **LC** electrolyte-based actuators under various condition.

The nanostructured ion conductive polymers obtained from lyotropic and thermotropic columnar **LC** assemblies were applied in **iEAP** actuators by sandwiching between two conductive polymer electrodes. Both of hydrous and anhydrous actuators exhibited actuation

response under a low driven voltage (≤ ±2 V). A high bending strain of 0.65% for anhydrous actuator was achieved at an AC of ±2V with a frequency of 0.01 Hz and a force of 1.2 mN was generated under a DC of 2 V within 2 min at ambient environment. The bending deformation was enhanced by increasing of relative humidity in operating environment. The maximum value of bending strain was reached to 0.84% at an AC of ±2 V with a frequency of 0.1 Hz in 70% RH atmosphere. The increase of ion content in the **LC** polymers can also enhanced bending displacement. The value of bending strain for polymers containing 50 mol% of ionic liquids was 4 times higher than that of polymers containing 40 mol% of ionic liquids under an AC of ±2 V. In addition, the blocking force was increased with ion content as well as the equilibrium time was reduced. Moreover, the ion species was proved to be an important factor for performance of **iEAP** actuators. The difference in volume size of cations and anions can lead to varying degrees of deformation. The thickness of electrolytes was shown to influence the performance in both strain and blocking force. The higher bending strain was obtained for thinner actuators, but the weaker force was generated at same time. In this section, the actuators based on 1D columnar polymer electrolytes was fabricated and low-voltage driven response was achieved at both dry and humid environment. The new developed **iEAP** actuators which can be operated in both dry and humid environment possess a wide application field such as biomedicals, haptics, and soft robotics.

3. Soft actuators based on columnar **LC**/polymer composite electrolyte with 3D continuous ionic nanochannels composed of rod-shaped zwitterionic molecules and ionic liquid.

A rod-like zwitterionic molecule with imidazolium cationic and sulfonate anionic moieties was designed. A columnar **LC** phase with 3D continuous interconnected channels was induced by combination of zwitterionic molecule with ionic liquid containing same cations and anions. The ionic conductivities of **LC** compound were about 10^{-5}–10^{-3} S cm^{-1} at room temperature. The polymer matrix (**PVA**) was induced into **LC** assembly to give a mechanical supporting for constructing free-standing electrolyte membrane in actuator. The **LC/PVA** composite membrane with 3D nanostructure showed one order higher conductivities comparing with the amorphous **PVA** film containing same amount of ionic liquids. By sandwiching **LC/PVA** composite membrane between two polymer electrodes, a large displacement of 15 mm and a fast motion rate of 2 mm within 220 ms was exhibited under a low voltage of ±1 V in 70% RH environment. The peak-to-peak bending strain of **LC/PVA**-based actuator was calculated to be

0.32% under 1V, which was higher than other reported amorphous ionic polymer-based actuators. In addition, the bending speed of **LC/PVA**-based actuator was two times higher than the **IL/PVA**-based actuator with same ion content under ±0.5 V. In this section, the new method of constructing 3D ionic channels in electrolyte were developed, and the large deformation with fast response was achieved under low applied voltage, which open up new ways for high-speed motion sensors and actuators.

5.2 Future prospective

Although the **LC**-based actuators in this study have shown fast and large actuation response under low voltage, there are still some improvements can be carried out to adapt practical application.

1. Low-power consumption actuators.

The low energy consuming devices are more attractive in the era of energy shortage. In that case, the actuators that can achieve larger displacement and blocking force under lower driven voltage should be designed. As we known, the ion migration acted as a critical role for actuation response of **iEAP** actuators. The migration of ions can determine the initial response time and ion distribution across the electrolyte, especially in high frequency operating condition. The optimized materials that can transport ions in high speed should be developed. The shorter migrating distance and less transporting obstacle were considered as a powerful method to achieve high speed ion-conduction. The macroscopically orientation of 1D columnar and 2D smectic **LC** assemblies can apply ionic channels that perpendicular to the surface of electrolyte films, which will eliminate the obstacle between each uncontinuous molecular domain and shorter transporting distance, resulting in high-speed ion conduction.[1-2] Furthermore, the selection of ionic liquids was another crucial factor to achieve larger deformation. The larger volume size of cation and the smaller volume size of anion can result in larger bending strain. Some anions with small volume size such as $\mathbf{OH^-}$ (9 $Å^3$) should be taken in consideration to replace of $\mathbf{TFSI^-}$ (147 $Å^3$), $\mathbf{CF_3SO_3^-}$ (80 $Å^3$) in this study. The high generated force will allow actuators to lift heavier stuffs which was benefit for application in smart transport mini robotic. The block force of **IMPC** actuators with thick electrolyte film (> 1000 μm) can reach 250 mN under a DC of 4 V and lift stuffs around 100 g due to the larger bending stiffness.[3] However,

thicker actuators normally show smaller deformation as discussed in chapter 3. Selection of an optimal thickness for **LC**-based **iEAP** actuators to balance the bending displacement and generated force need to be explored for low-energy consuming practical applications.

2. Long-durability actuators in ambient environment.

The durability of **iEAP** actuators was affected by several factors such as water evaporation, the detachment of electrodes and electrolytes, ion-leakage and so on. The dry actuator can be adapted to ambient environment regardless the loss of water in a long-term operation. There are many works reported for dry **iEAP** actuators. However, the introduction of 3D **LC** nanostructured into electrolyte to achieve anhydrous ion conduction is still challenging because the 3D cubic LC phase usually needs water to induce. One possible assumption is fixation the 3D cubic **LC** phase in the polymers and then replace the water with protonic ionic liquids to form continuous hydrogen bonding networks along nanochannels. Furthermore, the stability of electrodes will also determine the durability of actuators. The optimized electrode materials and the insertion of interface to combine electrodes with electrolytes can improved the actuation circles more than 10000.[4-5]

3. Multi-response **LC** actuators.

The **LC** materials can not only response to electric field, but also to various external stimulus such as light, humidity, thermal.[6-8] Such stimulus is easily found in nature which can be utilized to power environmental-friendly **LC** actuators. To imitate the response of artificial skins to natural environment to the greatest extent, multi-response **LC** actuators are one of the most popular candidates. Recent years, **LC** actuators that can by trigger by two stimuluses have been reported.[9-11] In addition, the switching of ionic conductivities by phase transition in **LC** materials has already achieved by temperature and UV light.[12-13] The author expected that taking advantage of such materials which can tune ion migration in electrolyte by electric, thermal, and light stimulus will create a series of multi-response **LC** actuators.

5.3 References

1. Yoshio, M.; Mukai, T.; Ohno, H.; Kato, T., One-Dimensional Ion Transport in Self-Organized Columnar Ionic Liquids. *J. Am. Chem. Soc.* **2004,** *126* (4), 994–995.

2. Kato, T., Uniaxially parallel alignment of a smectic A Liquid Crystalline Rod Coil Molecule and its

Lithium Salt Complexes using Rubbed Polyimides. *Macromolecules* **2007**.

3. Park, J. H.; Lee, S. W.; Song, D. S.; Jho, J. Y., Highly Enhanced Force Generation of Ionic Polymer–Metal Composite Actuators via Thickness Manipulation. *ACS Appl. Mater. Interfaces* **2015,** *7* (30), 16659–16667.

4. Simaite, A.; Tondu, B.; Souères, P.; Bergaud, C., Hybrid PVDF/PVDF-graft-PEGMA Membranes for Improved Interface Strength and Lifetime of PEDOT:PSS/PVDF/Ionic Liquid Actuators. *ACS Appl. Mater. Interfaces* **2015,** *7* (36), 19966–19977.

5. Lu, C.; Yang, Y.; Wang, J.; Fu, R.; Zhao, X.; Zhao, L.; Ming, Y.; Hu, Y.; Lin, H.; Tao, X.; Li, Y.; Chen, W., High-Performance Graphdiyne-Based Electrochemical Actuators. *Nat. Commun.* **2018,** *9* (1), 752.

6. Yu, H.; Ikeda, T., Photocontrollable Liquid-Crystalline Actuators. *Adv Mater* **2011,** *23* (19), 2149-2180.

7. Dai, M.; Picot, O. T.; Verjans, J. M. N.; de Haan, L. T.; Schenning, A. P. H. J.; Peijs, T.; Bastiaansen, C. W. M., Humidity-Responsive Bilayer Actuators Based on a Liquid-Crystalline Polymer Network. *ACS Appl. Mater. Interfaces* **2013,** *5* (11), 4945-4950.

8. Lu, H.-F.; Wang, M.; Chen, X.-M.; Lin, B.-P.; Yang, H., Interpenetrating Liquid-Crystal Polyurethane/Polyacrylate Elastomer with Ultrastrong Mechanical Property. *J. Am. Chem. Soc.* **2019,** *141* (36), 14364–14369.

9. Liu, Y.; Xu, B.; Sun, S.; Wei, J.; Wu, L.; Yu, Y., Humidity- and Photo-Induced Mechanical Actuation of Cross-Linked Liquid Crystal Polymers. *Adv. Mater.* **2017,** *29* (9), 1604792.

10. Liu, H.; Tian, H.; Shao, J.; Wang, Z.; Li, X.; Wang, C.; Chen, X., An Electrically Actuated Soft Artificial Muscle Based on a High-Performance Flexible Electrothermal Film and Liquid-Crystal Elastomer. *ACS Appl. Mater. Interfaces* **2020,** *12* (50), 56338–56349.

11. Xu, Z.; Ding, C.; Wei, D. W.; Bao, R. Y.; Ke, K.; Liu, Z. Y.; Yang, M. B.; Yang, W., Electro and Light-Active Actuators Based on Reversible Shape Memory Polymer Composites with Segregated Conductive Networks. *ACS Appl. Mater. Interfaces* **2019,** *11* (33), 30332–30340.

12. Soberats, B.; Yoshio, M.; Ichikawa, T.; Zeng, X.; Ohno, H.; Ungar, G.; Kato, T., Ionic Switch Induced by a Rectangular–Hexagonal Phase Transition in Benzenammonium Columnar Liquid Crystals. *J. Am. Chem. Soc.* **2015,** *137* (41), 13212–13215.

13. Soberats, B.; Uchida, E.; Yoshio, M.; Kagimoto, J.; Ohno, H.; Kato, T., Macroscopic Photocontrol of Ion-Transporting Pathways of a Nanostructured Imidazolium-Based Photoresponsive Liquid Crystal. *J. Am. Chem. Soc.* **2014,** *136* (27), 9552–9555.

Acknowledgement

Firstly, I would like to show my sincere respect and appreciate to my supervisor Prof. Masafumi Yoshio. His sufficient knowledge provided a powerful help for my research. I cannot finish my doctoral work without his assist. His valuable guidance, continuous patience, and positive attitude encouraged me a lot. His passionate and strict attitude to academic work is worthy to learn in my whole life.

I also want to appreciate to Prof. Kazuki Sada, Prof. Toshifumi Satoh, Prof. Kazunari Yamaura, and Prof. Takuya Masuda for their and guidance to my research. Their suggestions helped me do better in my work.

I would like to express my thanks to all the members in the Molecular Mechatronics Group in NIMS. Thanks for the kind help provided by Dr. Junko Aimi, Dr. Wenjing Meng, Dr. Yoshihiro Yamauchi, Mr. Shunichi Suwa, Mr. Che-Hao Wu, Ms. Izumi Matsunaga, Ms. Bo Zhou.

Last but not the least, I would like to express my deepest appreciate to my parents and other families. Their unconditional love, patient support, kind encouragement accompanies me all the time.